Institut de Physique
Université de Neuchâtel

Broadly tunable mid-infrared quantum cascade lasers for spectroscopic applications

THESE

présentée à la Faculté des Sciences de l'Université de Neuchâtel
pour l'obtention du grade de Docteur ès Sciences

par

Richard Maulini

Soutenue le 23 novembre 2006 en présence d'un jury composé de

Prof. Jérôme Faist, Directeur de thèse, Université de Neuchâtel
Prof. Hans-Peter Herzig, Université de Neuchâtel
Prof. Daniel Courtois, Université de Reims Champagne-Ardenne, France
Dr. Alessandro Tredicucci, NEST & Scuola Normale Superiore, Pisa, Italia

Neuchâtel, Novembre 2006

Université de Neuchâtel unine

FACULTE DES SCIENCES
Secrétariat-Décanat de la faculté
Rue Emile-Argand 11
CP 158
CH-2009 Neuchâtel

IMPRIMATUR POUR LA THESE

Broadly tunable mid-infrared quantum cascade lasers for spectroscopic applications

Richard MAULINI

UNIVERSITE DE NEUCHATEL

FACULTE DES SCIENCES

La Faculté des sciences de l'Université de Neuchâtel,
sur le rapport des membres du jury

MM. J. Faist (directeur de thèse),
H.P. Herzig,
A. Tredicucci (Pise I)
et D. Courtois (Reims F)

autorise l'impression de la présente thèse.

Neuchâtel, le 7 décembre 2006

Le doyen :
J.-P. Derendinger

UNIVERSITE DE NEUCHATEL
FACULTE DES SCIENCES
Secrétariat-décanat de la faculté
Rue Emile-Argand 11 - CP 158
CH-2009 Neuchâtel

Téléphone : +41 32 718 21 00 Fax : +41 32 718 21 03 E-mail : secretariat.sciences@unine.ch www.unine.ch/sciences

Ce travail est dédié à la mémoire de Gilles Maulini

Keywords

Semiconductor heterostructures, intersubband transitions, quantum cascade lasers, tunable lasers, mid-infrared spectroscopy.

Mots clés

Hétérostructures semiconductrices, transitions intersousbandes, lasers à cascade quantique, lasers accordables, spectroscopie moyen-infrarouge.

Abstract

Quantum cascade lasers are unipolar semiconductor lasers based on intersubband transitions in heterostructures. These lasers, which have demonstrated continuous wave operation at room temperature in the mid-infrared spectral range, are well suited for the realization of compact, ultra-sensitive, trace-gas sensors based on absorption spectroscopy. Up to now, only distributed feedback (DFB) single-mode devices have been used for such applications. DFB quantum cascade lasers have proven to be effective for gas sensing, but their relatively narrow tuning range, smaller or equal to about 1% of the wavelength, makes them not very versatile and limits their usefulness for spectroscopic investigations.

In this thesis we developed broadly tunable external cavity quantum cascade lasers. The main advantage of these sources compared with DFBs is their broader tuning range, which is limited only by the spectral bandwidth of the gain element.

We particularly studied broad gain bandwidth active regions based on bound-to-continuum designs. With that kind of active region, we have demonstrated a tuning range equal to 15% of the center wavelength at $\lambda \cong 10$ μm, which was three times broader than the best values reported in the literature at that time, as well as good performance in pulsed mode at room temperature.

Using a strain-compensated bound-to-continuum design emitting near 5.2 μm, we have demonstrated for the first time continuous-wave operation of an external cavity quantum cascade laser on a thermoelectric cooler. The tuning range was comparable to that of pulsed devices, but with a much better side-mode suppression ratio and a much narrower linewidth. This continuous-wave device has successfully been applied to the spectroscopy of nitric oxide in collaboration with Prof. Tittel's Laser Science Group at Rice University. High resolution

absorption spectra of that gas could be acquired over a large wavelength range.

We also studied heterogeneous cascade structures, that is quantum cascade structures in which the various stages emit at several different wavelengths, as a way to increase further the tuning range of external cavity quantum cascade lasers. A pulsed laser tunable from 8.2 to 10.4 μm, that is over 24% of the center wavelength has been realized using an active region composed of two substacks of bound-to-continuum designs.

We conclude on the feasibility of room temperature, continuous-wave, broadly-tunable external cavity quantum cascade lasers in the mid-infrared spectral range. These devices will be useful for the analysis of multi-component gases, for high resolution spectroscopic investigations in fundamental science, and for the detection of heavy molecules with broad absorption features which DFB quantum cascade lasers cannot scan entirely.

Résumé

Les lasers à cascade quantique sont des lasers semiconducteurs unipolaires basés sur des transitions intersousbandes dans des hétérostructures. Ces lasers, qui ont démontré une opération continue à température ambiante dans la région spectrale de l'infrarouge moyen, sont bien adaptés pour la réalisation de détecteurs de gaz compacts ultra-sensibles basés sur la mesure de l'absorption spectroscopique. Jusqu'à maintenant seuls des dispositifs monomodes à contre-réaction répartie (DFBs) ont été utilisés pour de telles applications. Les lasers à cascade quantique DFBs ont prouvés qu'ils sont efficaces pour la détection de gaz, mais leur gamme d'accord relativement étroite, plus petite ou égale à environ 1% de la longueur d'onde, ne les rend pas très souples et limite leur utilité pour les études spectroscopiques.

Dans cette thèse, nous avons développé des lasers à cascade quantiques à cavité externe largement accordables. Le principal avantage de ces sources sur les DFBs est leur gamme d'accord plus large qui n'est limitée que par la bande passante de l'élément amplificateur.

Nous avons particulièrement étudié des régions actives à large gain basées sur des designs bound-to-continuums. Avec ce type de régions actives, nous avons démontré une gamme d'accord égale à 15% de la longueur d'onde centrale à $\lambda \cong 10$ μm, ce qui était trois fois plus large que les meilleures valeurs reportées dans la littérature à ce moment-là, ainsi que des bonnes performances en mode pulsé à température ambiante.

En utilisant un design bound-to-continuum à contrainte compensée émettant vers 5.2 μm, nous avons démontré pour la première fois l'opération en continu d'un laser à cascade quantique à cavité externe à cavité externe sur un refroidisseur Peltier. La gamme d'accord était comparable à celle des dispositifs pulsés, mais avec un bien meilleur rapport de suppresion de modes latéraux et une largeur de ligne bien plus étroite.

Ce dispositif continu a été appliqué avec succès à la spectroscopie de l'oxyde nitrique en collaboration avec le groupe du professeur Tittel à l'université Rice de Houston. Des spectres d'absorption à haute résolution de ce gaz ont pu être mesurés sur une large gamme de longueurs d'onde.

Nous avons aussi étudié des cascades hétérogènes, c'est à dire des structures à cascade quantique dans lesquelles les différentes périodes émettent à plusieurs longueurs d'onde différentes, comme moyen d'augmenter encore plus la gamme d'accord des lasers à cascade quantique à cavité externe. Un laser pulsé accordable de 8.2 à 10.4 μm, c'est à dire sur 24% de la longeur d'onde centrale a été réalisé en utilisant une région active composée de deux sousensembles de designs bound-to-continuums.

Nous concluons à la faisabilité de lasers à cascade quantique à cavité externe largement accordables émettant en continu à température ambiante dans la région spectrale de l'infrarouge moyen. Ces dispositifs seront utiles pour l'analyse de gaz à plusieurs composants, pour les études spectroscopiques à haute résolution en recherche fondamentale, et pour la détection de molécules lourdes avec des lignes d'absorption larges que les lasers à cascade quantique DFBs n'arrivent pas à scanner entièrement.

Contents

Abstract **iii**

Résumé **iv**

1 Introduction **1**
1.1 General introduction . . . 1
1.2 Coherent light sources in the mid-infrared . . . 2
1.2.1 CO_2 laser and other gas lasers . . . 4
1.2.2 Lead salt diode lasers . . . 5
1.2.3 Antimonide-based semiconductor lasers . . . 6
1.2.4 Sources based on optical parametric generation . . . 10
1.3 Quantum cascade lasers . . . 12
1.3.1 Fundamentals . . . 12
1.3.2 State of the art . . . 20
1.3.3 Single-mode devices . . . 22

2 Theory **39**
2.1 Quantum cascade lasers . . . 39
2.1.1 Electronic states in heterostructures . . . 39
2.1.2 Intersubband relaxation times . . . 42
2.1.3 Spontaneous emission and gain between subbands . . . 43
2.1.4 Intersubband absorption linewidth . . . 44
2.1.5 Rate equations . . . 45
2.2 Grating-coupled external cavity lasers . . . 47
2.2.1 Modeling of the Littrow configuration . . . 48
2.3 Tuning properties . . . 52
2.3.1 Coarse tuning range . . . 52
2.3.2 Fine tuning behavior . . . 52
2.4 Anti-reflection coating . . . 54

3 Device fabrication and characterization **61**
3.1 Epitaxial growth . . . 61
3.2 Sample processing . . . 62
3.3 Electrical and optical characterization . . . 64

3.4 Anti-reflection coatings 65

4 Pulsed external cavity quantum cascade lasers emitting near 10 μm 71
4.1 Introduction 71
4.2 Active region design 72
4.2.1 The bound-to-continuum design 72
4.2.2 Calculation of the gain and spontaneous emission spectra 74
4.2.3 Measured spontaneous emission spectra 76
4.3 Fabry-Pérot chip performance 77
4.4 External cavity laser performance 78
4.5 Time-resolved spectra 81
4.5.1 Experimental setup 82
4.5.2 Results 82
4.5.3 Dynamical model 82

5 Continuous-wave external cavity quantum cascade laser emitting near 5.2 μm 87
5.1 Introduction 87
5.2 Active region design 88
5.3 Chip fabrication and performance 89
5.4 Setup for continuous-wave operation 91
5.5 Laser performance 91
5.5.1 Threshold current 91
5.5.2 Coarse tuning range and spectral purity 92
5.5.3 Output power 92
5.5.4 Fine tuning 93
5.6 Laser linewidth 94
5.6.1 Theoretical model 95
5.6.2 Experimental determination of an upper limit using heterodyne mixing 97
5.7 High-resolution spectroscopic applications 100

6 External cavity quantum cascade lasers based on heterogeneous cascade active regions 107
6.1 Introduction 107
6.2 Structure design 109
6.2.1 Active region 109
6.2.2 Waveguide 109
6.2.3 Spontaneous emission spectra 110
6.3 Rate equation model 112
6.4 Fabrication and characterization of the gain elements 115
6.5 Performance of external cavity lasers 118
6.6 Continuous-wave heterogeneous cascade devices 120

7 Conclusions 125

Acknowledgements **129**

Published work **131**

Contributions **133**

Chapter 1

Introduction

1.1 General introduction

The infrared (IR) radiation is the region of the electromagnetic spectrum with wavelengths longer than visible light (400 to 710 nm) but shorter than microwaves (1 mm to 30 cm). It is often divided in three subregions: the near infrared (NIR) going from 710 nm to 2.5 μm, the mid-infrared (MIR) from 2.5 to 25 μm, and the far infrared (FIR) from 25 μm to 1 mm.

The near-infrared radiation interacts with matter essentially the same way as visible light. This spectral range has a major technological importance because it is a standard for optical telecommunications and data storage. Nowadays, it is by far the most developped of the three IR subregions in terms of available laser sources and detectors. High performance NIR diode lasers are easily available and inexpansive because of mass-fabrication. According to Ref. [1], 396 million units have been sold during year 2004, compared to 337 millions of visible diode lasers and 131 millions of all other types of lasers.

The far-infrared or terahertz region is at the boundary between light and microwaves. Coherent THz local oscillators are important in astronomy since most of the interstellar dust clouds emit in this region. Other applications of THz radiation include imaging in the fields of biology, medecine, and homeland security and absorption spectroscopy. However,

the development of these applications is slow because of the lack of compact, powerful sources of coherent radiation in this region (sometimes refered to as the THz gap). This situation may change with the ongoing development of THz quantum cascade lasers if cryogenic free operation can be achieved.

In this thesis, I will focus on the development of tunable laser sources in the mid-infrared spectral range for spectroscopic applications. The MIR range, sometimes called the fingerprint region of the electromagnetic spectrum, is of enormous scientific and technological interest since many molecules have their fundamental rotational-vibrational absorption bands in this range. The MIR absorption spectrum is very specific to the structure of a particular molecule, allowing highly selective detection. In addition, since these absorption lines are very strong (several orders of magnitude stronger than the overtone and combination bands in the NIR), concentrations in the parts-per-billion (ppb) to parts-per-trillion (ppt) ranges can be detected using relatively compact laser-based sensors. Fast, sensitive, and selective chemical sensors are needed in numerous applications. In industrial process control they are used for detection of contamination in semiconductor fabrication lines and for plasma monitoring, in law enforcement for drug and explosive detection, in automotive industry for engine exhaust analysis, in environmental science for pollution monitoring, in medical diagnostics for exhaled breath analysis, and in homeland security for detection of chemical warfare agents.
Another interesting feature of the MIR are the atmospheric transmission windows between 3-5 μm and 8-12 μm which enable free-space optical communications, remote sensing, and thermal imaging. High power lasers in the 3-5 μm range will also enable the development of infrared counter-measures for homeland security.

1.2 Coherent light sources in the mid-infrared

The history of coherent light sources emitting in the mid-infrared started in the early sixties and is strongly related to the history of lasers in general. A few years after the first

realization, in 1954, of a coherent microwave source based on stimulated emission (MASER, acronym for microwave amplification by stimulated emission of radiation) by Townes and co-workers[2][3], a theoretical study realized by Schawlow and Townes in 1958 concluded on the feasibility of similar devices emitting in the infrared and visible regions[4]. The first such optical maser or laser, based on an optically pumped ruby cristal emitting in the visible, has been reported in 1960 by Maiman[5]. Already the second laser to be demonstrated, the uranium laser, the same year by Sorokin et al.[6] (which is also the first four-level laser, the ruby laser being based on a three level scheme), was emitting in the MIR at 2.5 μm. However, because of several factors such as the need for cryogenic cooling, Sorokin's laser has never found many practical applications. Two years later, in 1962, a much more important class of lasers has been demonstrated: diode lasers. Among the four groups who have demonstrated it almost simultaneously (in chonological order of publication, Hall et al.[7], Nathan et al.[8], Holonyak et al.[9], and Quist et al.[10]), three used GaAs homojunctions emitting in the NIR at 840 nm and one (Holonyak) a GaAsP homojunction emitting in the visible at 710 nm. The first MIR diode laser has been realized only one year later by Melngailis [11] using InAs material emitting at 3.1 μm. Another class of MIR diode lasers, which turned out to be important for spectroscopy, the lead salt lasers, has been invented in 1964. In Ref. [12], Butler et al. report laser action at 6.5 μm in PbTe and at 8.5 μm in PbSe diodes. Another milestone in the development of MIR lasers is the invention of the CO_2 laser by Patel[13][14] also in 1964.

Still in the mid-60s, one can still mention the first demonstration of difference frequency generation (DFG) of light[15] and the first realization of an optical parametric oscillator (OPO)[16] in nonlinear cristals, using the young laser technology. Both methods are still commonly used for generation of coherent MIR radiation because they can produce it over a wide range, only limited by the transparency of the nonlinear cristal, with the same spectral and beam properties as the pump laser(s).

In spite of all these early breakthroughs, the advent of a compact, high power, cryogenic-free, coherent mid-infrared source happened only in the nineties with the invention of the

quantum cascade laser by Faist et al.[17]. The main reason for that is the difficulty to make a diode laser emitting at room temperature in this spectral range because of the large non radiative recombination rate, dominated by Auger processes, in narrow gap semiconductors. These processes, in which the energy and momentum of the recombinating electron-hole pair are transfered to another carrier, generally an electron, lead to a relaxation rate varying with temperature as

$$\frac{1}{\tau_{\text{Auger}}} \propto \exp\left(-\frac{E_g/kT}{1+m_h/m_e}\right) \tag{1.1}$$

which makes it very difficult to obtain population inversion at non cryogenic temperature[18].

In this section I will review the most interesting coherent MIR sources for spectroscopy and gas sensing: the CO_2 laser and other gas lasers, the highest performance (lead salt and antimonide based) interband semiconductor lasers, and the sources based on optical parametric generation. The quantum cascade lasers will be discussed in details in Section 1.3. Interested readers can find a recent review of solid state mid-infrared lasers in the book edited by Sokorina and Vodopyanov[19] which includes a chapter on mid-infrared laser applications in spectroscopy by Tittel et al.[20].

1.2.1 CO_2 laser and other gas lasers

The CO_2 laser was one of the earliest lasers to be developed and is still one of the most useful. These lasers, which have their main emission wavelength bands around 9.6 and 10.6 μm, can deliver high power, up to several hundreds of watts in continuous-wave (CW) mode, with a conversion efficiency up to $\sim$20%. Because of their high power levels and reasonable cost, CO_2 lasers are frequently used in power-demanding industrial applications like cutting and welding of metals. They are also very useful in surgical procedures because water, which makes up most biological tissue, strongly absorbs this wavelength.

Coming to spectroscopic applications, CO_2 lasers are particularly interesting for photoacoustic spectroscopy because several watts can be obtained from relatively compact devices, enabling the realization of ultra-sensitive field deployable sensors (see for example Pushkarsky

et al.[21]). These lasers are line-tunable, that is they can be tuned only on the vibrational-rotational transitions of the CO_2 molecule. The positions of these lines and their relative strengths are shown in Fig. 1.1 for the $^{12}CO_2$ and $^{13}CO_2$ isotopes. The spectra cover a large wavelength range ($\approx$ 9.2 to 11.5 μm) but are constituted of discrete lines separated by 1-3 cm^{-1} gaps.

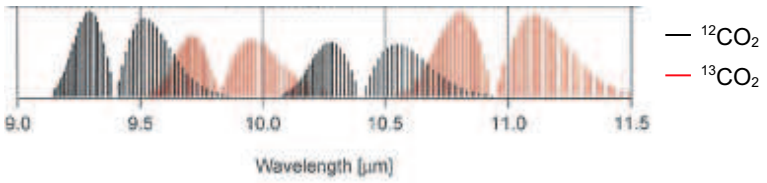

Figure 1.1: Positions and relative power levels of the $^{12}CO_2$ and $^{13}CO_2$ lasing transitions (reprinted from Ref. [22]).

Among the other gas lasers operating in the MIR, let's cite the CO laser which is line-tunable in the 5-8 μm region when operated on the fundamental rotational-vibrational transitions and in the 2.5-4 μm region when operated on the first overtone band.

1.2.2 Lead salt diode lasers

The IV-VI lead salt semiconductors are interesting materials for MIR optoelectronics because of their particular band structure. In these materials the direct bandgap is not located at the Γ point, in the center of the Brillouin zone, as for most III-V semiconductors, but there are four band minima located at the L points, on the (111)-axes. In addition, the conduction and valence band are quite similar, so that electrons and holes have comparable effective masses. This property results in a two orders of magnitude smaller Auger recombination rate for the Pb salts at equal bandgap energy, allowing to maintain population inversion and thus laser operation, at higher temperature[23].

Laser diodes based on this material system have been developed for operation at wavelengths from 3 to 30 μm. The active regions are usually double heterostructures and are grown by MBE. The confining material is PbSe, PbTe, or PbS and the bandgap of the active

material is adjusted by addition of Cd, Sn, Eu or Yb that leads to a strong shift of the transition energy with little lattice constant variation. Because of the small Auger recombination rate, operation up to 60°C at $\lambda \cong 5$ μm could be achieved in pulsed mode[24] but, because of the low thermal conductivity of those materials, CW operation was observed only up to 223 K[25], and thus requires liquid nitrogen cooling. The typical output powers are of the order of hundreds of microwatts. Although single-mode distributed-feedback devices have been demonstrated, the limited market has not allowed the necessary investments to turn them into a commercial product. The standard devices are Fabry-Pérot chips tuned by current and/or temperature. The typical tuning range is 100-200 cm^{-1} by changing the device temperature, or several tens of cm^{-1} by changing the injection current. Both tuning mechanisms, however, produce semicontinuous wavelength coverage since the laser structure is a Fabry-Pérot device. Varying the injection current generally allows continuous tunability over a $\approx$ 1-2 cm^{-1} spectral region before the output jumps to a new longitudinal mode. In some cases the gain is broad enough to support multiple longitudinal modes simultaneously, resulting in wavelength regions where the lasing output gradually shifts from one mode to another[20].

Lead salt diode lasers have proven effective in scientific applications, but are less often used in industrial applications because of several important practical drawbacks. One of them is the need for cryogenic cooling, but, in addition, the characteristics of the diode may change with temperature cycling or lead wire manipulation. Although all present Pb-salt devices are temperature-cycled by the manufacturer to minimize these problems, the finite probability of such changes is unacceptable for many applications.

Lead salt lasers based on PbSe emitting between 3 and 15 μm are commercially available from Laser Components GmbH, Olching, Germany.

1.2.3 Antimonide-based semiconductor lasers

The semiconductor system composed of (AlGaIn) III elements and (AsSb) V elements on GaSb substrate is widely used for production of infrared laser chips. The large number

of possible alloys gives a large freedom for the active region and waveguide design. I will discuss the three highest performance classes of such devices: type-I quantum well diode lasers, type-II W diode lasers, and interband cascade lasers.

Type-I quantum well diode lasers

The active region of (AlGaIn)(AsSb)-based quantum well (QW) diode lasers is composed of GaInAsSb QWs surrounded by low-Al-content AlGaAsSb barriers and high-Al-content AlGaAsSb separate confinement layers grown on a n-GaSb substrate. The wavelength can be tailored between $\approx$1.8 and 3 μm by varying the In concentration in the wells. These lasers can operate in continuous-wave at room temperature up to a wavelength of 3 μm. Room temperature CW operation has been demonstrated at 2.8 μm by Kim et al.[26] with an output power of 160 mW and at 3.04 μm by Lin et al.[27] with an output power of a few mWs. In both cases QWs containing 50% of In have been used. To reach longer wavelengths it is necessary not only to increase the In content in the wells but also the amount of As in order to stay within the strain limits for pseudomorphic growth on GaSb. This has the effects of decreasing the valence band offset with respect to the barriers, thus reducing the hole confinement, and of degrading the material quality.

Single-mode DFB QW antimonide lasers operating CW at room temperature up to a wavelength of 2.8 μm, are commercially available from at least two companies: Sarnoff Corporation, Princeton, NJ, USA and Nanoplus GmbH, Gerbrunn, Germany.

Type-II "W" diode lasers

Given the above-discussed material limitations, type-I QWs active regions in which electron and holes are confined in the same GaInAsSb layer are well suited for the realization of laser diodes with emission wavelengths up to 3 μm. For semiconductor lasers emitting in the 3 to 5 μm atmospheric transparency window, another approach, taking advantage of the broken-gap type-II band alignment between InAs and GaInSb, is generally used. Because the valence-band edge of GaInSb (well material for holes) lies above the conduction band

edge of InAs (well material for electrons), the transition energy depends only on the confinement energies and can be tailored over a wide range from nearly zero to several hundreds of meVs. A superlattice active region based on this material system has first been proposed by Grein et al.[28] in 1994 and realized by Hasengerg et al.[29] in 1995. The same year Meyer et al.[30] proposed another design, later called "W" quantum well because of its conduction band profile (see Fig. 1.2), in which three-layer InAs/GaInSb/InAs QWs (one hole well between two electron wells) are surrounded by AlGaAsSb barriers. The W design has the advantages of a strong overlap of the electron and hole wavefunctions resulting in a large dipole matrix element for the radiative transition, a two-dimensional density of states for both types of carriers, and a significant reduction of the Auger recombination rate. These lasers demonstrated their best performance in the 3-4 μm range with pulsed operation up to 317 K[31] and CW operation up to 230K[32]. Higher operating temperature and output power in the same wavelength range have been reported using interband cascade lasers based on the same material system.

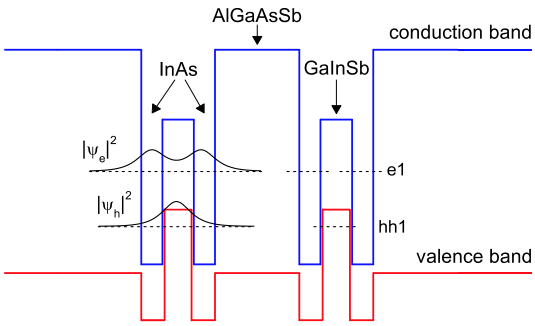

Figure 1.2: Band structure of a W multi-quantum-well diode laser. The moduli squared of the electron and hole wavefunctions are showed at the corresponding energy levels.

Interband cacade lasers

Interband cascade lasers (ICLs) are semiconductor lasers exploiting a cascade scheme similar to that of quantum cascade lasers, but in which the radiative transition occurs between the conduction and valence bands. The ICL concept has been first proposed by Yang[33]

in 1995, one year after the first realization of a QCL. An improved design together with a gain calculation were published later by Meyer et al.[34]. Meyer's design is presented in Fig. 1.3. After a diagonal radiative transition between an InAs electron QW and a GaInSb hole QW, carriers undergo a resonant interband tunelling into a further InAs well and are injected in the upper state of the next period by an InAs/AlSb superlattice injector. The first realization of an ICL, at 3.8 μm, has been reported in 1997 by Lin et al.[35]. In 1998, Vurgaftman et al.[36] proposed an ICL design based on a W active region similar to that of W diodes (see inset of Fig. 1.3) in which the optical coupling is $\sim$2 times stronger because of the better overlap of the electron and hole wavefunctions. Even though devices with wavelength as large as 5.4 μm have been reported[37], ICLs demonstrated their best performance in the 3-4 μm wavelength range. CW operation on thermoelectric cooler has recently been reported at 3.3 μm by Mansour et al.[38] up to a temperature of 264 K and at 3.7 μm by Bewley et al.[39] up to a temperature of 257 K with an output power in excess of 20 mW at 240 K.

Fabry-Pérot and single-mode DFB ICLs are commercially available from Maxion Technologies Inc., Hyattsville, MD, USA.

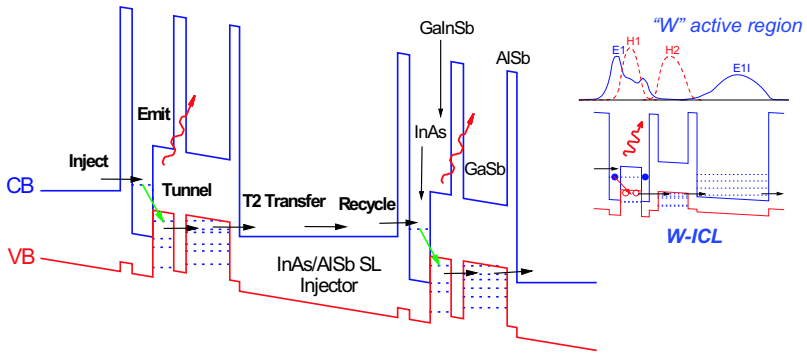

Figure 1.3: Band diagram of the type-II interband cascade active region design proposed by Meyer et al.[34]. Inset: band diagram of a W ICL active region with moduli squared of the relevant wavefunctions.

1.2.4 Sources based on optical parametric generation

In this section I will give an overview of coherent mid-IR light sources based on optical parametric generation in nonlinear cristals. There are two principal methods of mid-IR generation using nonlinear materials: difference frequency generation (DFG) and optical parametric oscillation (OPO), as schematically illustrated in Fig. 1.4. Both techniques allow exchange of energy between three optical frequencies, known as pump (ν_p), signal (ν_s), and idler (ν_i) and related by the energy conservation relation: $\nu_p = \nu_s + \nu_i$.

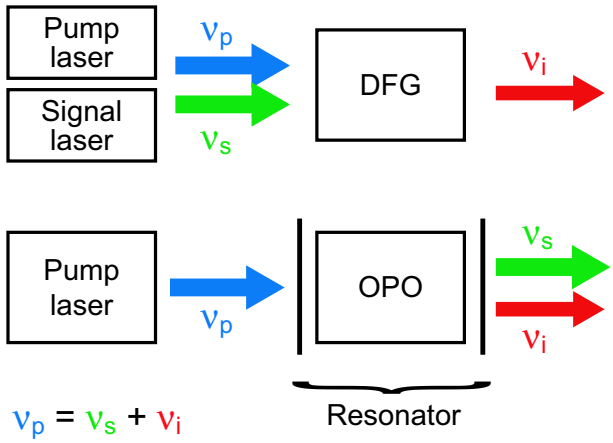

Figure 1.4: Schematic illustrations of the difference frequency generation and optical parametric oscillation processes.

Difference frequency generation

Difference frequency generation is the process of mixing two single-frequency sources, called pump and signal, on a single pass through a nonlinear material to generate tunable narrowband radiation at a third frequency, called idler, equal to the difference between the two input frequencies. The narrow emission spectra of the two input sources are convolved during the frequency conversion, resulting into a similarly narrow spectrum for the idler wave. Idler wavelength tuning is accomplished by tuning of the pump or the signal laser, or both. In order that the idler wave continues to build up as the beams travel through the nonlinear material, the three waves must stay in phase. This phase matching condition

can be satisfied in a birefringent nonlinear crystal by polarizing some of the waves along an ordinary axis and some along the extraordinary axis.

A more convenient way to overcome the phase matching problem is to use periodically poled materials in which the sign of the second order susceptibility changes periodically, bringing back the three waves in the right phase relation. This technique is called quasi phase matching. Periodic poling is most easily achieved in ferroelectric crystals, like $LiNbO_3$, in which the poling can be permanently reversed locally by the application of an external electric field at high temperature[40]. The high nonlinearity and long interaction length of periodically poled lithium niobates (PPLNs) make them the material of choice for such applications. In addition, the ability to engineer its poled structure with a photolithographic mask allows the integration of multiple grating periods in a single crystal or the realization of a fan-out structure for continuous phase matching[41].

The development of PPLNs permits to use near-infrared diode or fiber lasers as pump lasers, making it feasible to construct compact mid-infrared sources that can operate at room temperature and generate sufficient CW output powers to be useful in spectroscopic applications.

An interesting feature of DFG is that the tuning range of the pump, in frequency units, is transmitted to the generated radiation, resulting in a much larger relative tuning. As an example, in the DFG source described in Ref. [42], based on two tunable diode lasers, tuning the signal at 980 nm over 32 nm (3% relative tuning) results in a tuning of the output from 3.6 to 4.3 μm, or 17%.

The principal limitation of the technique is that the efficiency of conversion is extremely low, resulting in maximum output power levels of the order of hundreds of microwatts to a few milliwatts.

Optical parametric oscillators

In an optical parametric oscillator (OPO), the pump beam is divided into two beams of smaller frequencies ν_s (signal), and ν_i (idler). How the frequency is divided between the new waves is determined by the phase matching condition. Contrary to the case of DFG, the nonlinear crystal is placed inside an optical cavity which resonates the signal (singly resonant

OPO) or both the signal and the idler (doubly resonant OPO). For the signal to oscillate in the resonator, the power dependent parametric gain has to compensate the losses. Thus there is a threshold pump power for optical parametric oscillation.

Like DFG systems, OPOs greatly benefited from the development of PPLNs and other periodically poled crystals. When using such nonlinear materials in singly resonant configuration, the continuous-wave oscillation threshold is as low as a few watts, allowing diode-pumped solid state lasers and fiber lasers to be used as pump lasers. The threshold power level can even be further reduced by placing the nonlinear crystal inside the cavity of the pump laser. Stothard et al. have reported a threshold of only 310 mW using intracavity pumping by a diode-pumped Nd:YVO_4 laser[43]. Coarse tuning of such a system is usually achieved by changing the poling period of the nonlinear crystal, which in the case of a fan-out PPLN is done simply by translating it, and fine tuning by adjusting the cavity length with a piezo-driven mirror, varying the temperature of the crystal or of an etalon, or tuning of the pump laser.

Today, state of the art mid-infrared OPOs can deliver up to several watts CW output power and have coarse tuning ranges larger than 1 μm and mode-hop free fine tuning ranges of several tens of cm^{-1}[44][45][46][47], making them useful sources for spectroscopy[48]. Ngai et al. from Radboud University, Nijmegen, The Netherlands have recently reported an OPO tunable from 2.75 to 3.8 μm with a mode-hop free tuning range of 450 cm^{-1} per poling period and have demonstrated its suitability for photoacoustic and cavity ring-down spectroscopy[49]. Methane (at 3.2 μm) and ethane (at 3.3 μm) were detected using cavity ring-down spectroscopy with detection limits of 0.16 and 0.07 ppb by volume, respectively.

1.3 Quantum cascade lasers

1.3.1 Fundamentals

Quantum cascade lasers (QCLs) are unipolar semiconductor lasers based on intersubband transitions in heterostructures. In a QCL, radiative transitions occur between confined

electronic states of the conduction band (even though in theory QCLs based on confined states of the valence band are possible as well, up to now only electroluminescence has been reported from p-type QC structures[50][51]). The principal characteristics of interband and intersubband transitions in quantum wells are illustrated in Fig. 1.5. In contrast to interband transitions, for which the joint density of states is constant for energies larger than the transition energy E_{21}, intersubband transitions have an atomic-like joint density of states peaked at E_{21}, resulting in narrow gain linewidth. Furthermore, because the initial and final subbands have the same curvature (neglecting nonparabolicity), this linewidth depends only indirectly on the subband populations through collision processes. Another fundamental characteristic of intersubband transitions is their short lifetimes. For subbands separated by more than an optical phonon energy $\hbar\omega_{\mathrm{LO}}$, the dominant scattering process is the emission of such phonons, resulting in lifetimes of the order of one picosecond.

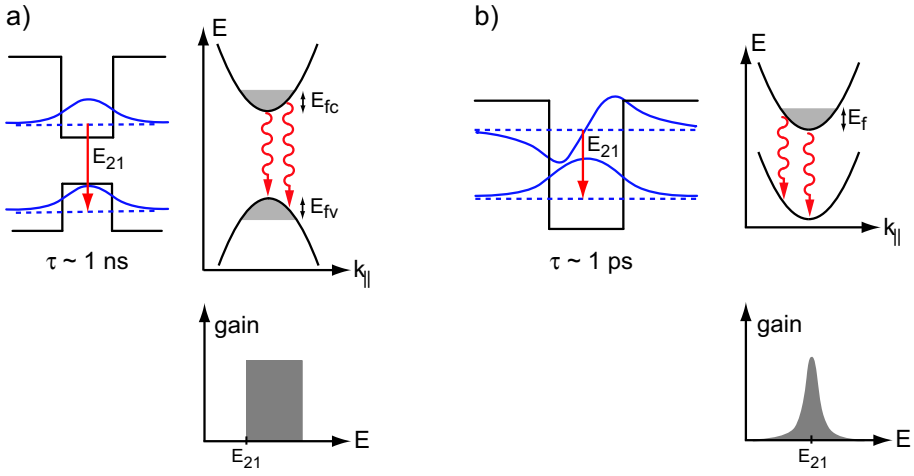

Figure 1.5: Principal characteristics of a) an interband transition and b) an intersubband transition in a quantum well.

The first proposal to use intersubband transitions in a semiconductor heterostructure for light amplification goes back to the early seventies with the seminal work of Kazarinov and Suris[52]. In their scheme, electrons tunnel from the ground state of a QW to the excited state of the neighboring one in a superlattice, emitting a photon in the process (photon-assisted tunneling). Following nonradiative relaxation to the ground state, electrons are

injected into the next stage and so forth sequentially for many stages. Population inversion is made possible by the relatively long scattering time associated with the diagonal transition between adjacent wells, compared with the short intrawell relaxation.

The first experimental observation of intersubband absorption in a GaAs/AlGaAs multi-quantum-well structure grown by MBE has been reported in 1985 by West and Eglash [53]. Early attempts to implement experimentally the proposal of Kazarinov and Suris in a GaAs/AlGaAs superlattice followed. They led to the observation intersubband luminescence pumped by resonant tunneling in 1989 by Helm et al.[54]. A large number of other schemes for mid- and far-infrared intersubband lasers have been proposed in the eighties and early nineties (see Ref. [55][56][57][58][59][60]).

The first realization of an intersubband laser, named quantum cascade laser by its inventors, has been reported in 1994 by Jérôme Faist and coworkers in Federico Capasso's group at AT&T Bell Laboratories, Murray Hill, NJ, USA[17]. This breakthrough was achieved using a cascaded structure in which each period consists of an undoped active region and an n-doped relaxation/injection region (see Fig. 1.6). The active region, which in this case consisted of three coupled QWs, is a three-level system in which population inversion between levels 3 and 2 is achieved by engineering of the lifetimes. The nonradiative relaxation time between levels 3 and 2 is increased by employing a transition with a reduced spatial overlap of the wavefunctions (diagonal transition), and the lifetime of state 2 is minimized by making the spacing with level 1 resonant with the optical phonon energy. The active region is left undoped because the presence of dopants significantly broadens the lasing transition by introducing a tail of impurity states[61]. The relaxation/injecton region has several functions. It is in this region that the electrons relax after the optical transition and are injected in the next period by resonant tunnelling. It also introduces an additional energy drop between the lower state of the laser transition and the ground state of the period, thus reducing the thermal backfilling of the former. Finally, it is doped to act as an electron reservoir, insuring that the integrated negative charge in the structure is compensated by the positive donors, even in the situation of strong injection to prevent the formation of space-charge domains.

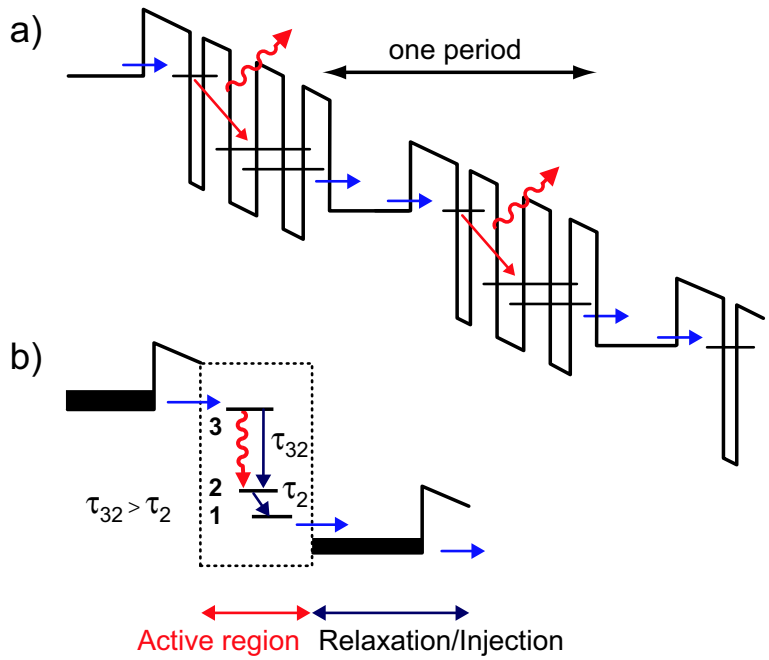

Figure 1.6: a) Schematic conduction band diagram of a quantum cascade laser. Each stage of the structure consists of an active region and a relaxation/injection region. Electrons can emit up to one photon per stage. b) General philosophy of the design. The active region is a three-level system. The lifetime of the $3 \rightarrow 2$ transition has to be longer than the lifetime of level 2 to obtain population inversion.

The fundamentally different nature of the quantum cascade laser compared with other MIR semiconductor lasers has strong consequences on the device properties:

1. Since the transition energy is determined only by the confinement energy of the electrons in the quantum wells and not by the bandgap energy of the material, devices emitting over a large wavelength range (up to about 50% of the conduction band offset) can be realized using the same material system.

2. The short lifetime of the upper state, limited by emission of optical phonons, results in a larger threshold current density at cryogenic temperature ($\geq$ 200 A/cm^2) but, on the other hand, it allows higher operating temperature because the temperature dependence of the relaxation time is weaker than in the case of Auger recombination. QCLs commonly have a characteristic temperature T_0 of the threshold current between

150 and 200 K.

3. The cascaded geometry of the structure in which electrons are recycled N_p times (where N_p is the numer of periods, typically 20 to 50) results in a larger differential quantum efficiency η_d proportional to N_p. High output power can thus be obtained from single-spatial-mode narrow ridge devices and not only from broad area devices.

4. The unipolarity (absence of holes in the structure) results in an increased robustness of the devices because there is no surface recombination.

5. The symmetric gain curve results in a very small linewidth enhancement factor ($\leq$ 0.2[62]) and thus a narrower linewidth.

6. The short lifetime of the upper state allows high frequency modulation without relaxation oscillations.

The first device reported by Faist et al., grown by MBE in the InGaAs/InAlAs/InP material system, emitted at a wavelength of 4.2 μm in pulsed mode at cryogenic temperature, up to $\sim$90 K. In the following years, the main performance improvements were due to optimization of the active region design. In 1995, Faist et al. introduced an injector designed to act as a Bragg reflector for the electrons in the upper state, in order to reduce escape in the continuum[63]. In 1996, Faist presented a three quantum well vertical transition active region with a narrow well close to the injection barrier to enhance the injection efficiency in the upper state and minimize the injection in the lower states and reported for the first time pulsed operation at room temperature[64]. The three QW design demonstrated excellent performance over a large wavelength range spanning from 3.4 μm[65] to 13 μm[66].
The Bell Labs group also investigated a radically different kind of designs based on interminiband transitions in superlattices (Scamarcio et al., 1997[67]). Those designs, in which population inversion relies on the long interminiband relaxation time compared with the intraminiband one, demonstrated very high current carrying capabilities and optical powers. Especially the chirped superlattice design presented by Tredicucci et al.[69] in which the

size of the wells is varied along the structure to obtain flat minibands without the need for dopants demonstrated good performance at long wavelengths, up to 24 μm[70].

Both above-mentioned designs demonstrated pulsed operation above room temperature and high power CW operation at cryogenic temperature, but none of them could be operated CW at room temperature because of totally different reasons. The 3 QW design suffers from a limited extraction from the active region which induces an thermal population of the lower state of the transition at high temperature. The chirped superlattice on the other hand suffers from a limited injection efficiency into the upper state since injection is not achieved through resonant tunnelling. In 2001, two new designs for high temperature, high duty cycle operation have been presented by Prof. Faist's group at University of Neuchâtel, Switzerland: the bound-to-continuum design[71] and the two-phonon resonance or four quantum well design[72].

The former is intended to combine the advantages of the three QW and the chirped superlattice designs. Electrons are injected in the upper state by resonant tunnelling and extracted from the lower state by intraminiband relaxation. This design, which is the basis of all the epilayers studied in this thesis, will be discussed in more details in Chap. 4.

The latter is based on a four level active region in which the radiative transition occurs between levels 4 and 3 and the three lower levels are separated by two optical phonon energies (see Fig. 1.7). Even if the tunnelling time out of the active region is similar to that of the three well design, the larger energy spacing between level 1 and 3 prevent a thermal population of the latter. This design served as basis for the realization of the first room temperature continuous wave QCL by Beck et al. at University of Neuchâtel in 2001[73].

The fundamental property of QCLs, that the emitting wavelength is determined by the thicknesses of the wells and barriers and can be tailored by bandgap engineering, allows the realization of devices emitting over a large wavelength range using the same material system, from 3.4 to 24 μm using InGaAs/InAlAs heterostructures on InP substrate as mentioned above. It also allows the fabrication of heterogeneous cascades emitting at several wave-

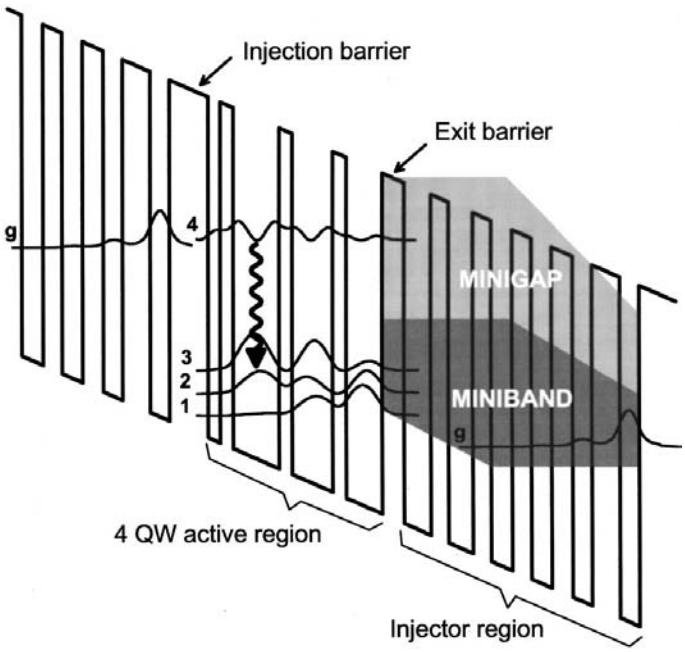

Figure 1.7: Schematic conduction band diagram with the moduli squared of the relevant wave functions of a 5.3 μm QC laser with a 4 QW active region. An electric field of 75 kV/cm was applied to align the structure. Reprinted from Ref. [72].

lengths simultaneously. This concept has been demonstrated by Gmachl et al. who realized a two-wavelength laser emitting at 5.2 and 8 μm[74] and an ultra-broadband laser covering all wavelengths from 6 to 8 μm[75].

Until now, I discussed only devices based on the InGaAs/InAlAs/InP material system, but QCLs based on other material systems have also been demonstrated. In 1998, Sirtori et al. from Thomson-CSF, Orsay, France, in collaboration with University of Neuchâtel, reported laser action in GaAs/AlGaAs[76]. This system seemed particularly promising because it offers a large flexibility for active region design and laser processing. Nevertheless the performance of the devices realized in the MIR, between 7.2 μm[77] and 23 μm[78], was always lower than that of the InP based devices.

In 2002, the GaAs/AlGaAs material system served as platform for a breakthrough in the development of QCLs and semiconductor lasers in general; the first realization of a device

emitting in the THz range by Köhler et al. from NEST-INFM and Scuola Normale Superiore, Pisa, Italy in collaboration with University of Cambridge, UK[79]. This first structure was based on a chirped superlattice design and emitted at 67 μm (4.4 THz). Today the wavelength coverage have been extended up to $\approx$250 μm (1.2 THz)[80] and maximum operating temperatures of 164 K in pulsed mode and 117 K in CW have been achieved at $\lambda \sim 100$ μm[81].

Laser action has recently been demonstrated in two other interesting material systems. In 2003, Ohtani and Ohno from Tohoku University, Sendai, Japan reported an InAs/AlSb QCL grown on an InAs substrate[82]. The large conduction band offset $\Delta E_c \cong 2.1$ eV of this heterostrucutre is well suited for the realization of short wavelength lasers. A device lasing at 3.1 μm and operating up to a temperature of 230 K has been demonstrated in this material system by Devenson et al. from University of Montpellier, France[83].

The material system InGaAs/AlAsSb, which has a conduction band offset of 1.6 eV and is lattice-matched to InP, is also interesting for the realization of short wavelength QCLs. The first laser based on these alloys has been reported in 2004 by Revin et al. from University of Sheffield, UK[84] and devices working at room temperature below 4 μm have been realized[85].

A milestone in the development of QCLs was the first growth of a QC structure by metalorganic vapor phase epitaxy (MOVPE) at University of Sheffield in 2003[94][95]. This alternative growth technique presents several advantages over MBE for commercial production of QCLs. MOVPE reactors offer the possibility of multiwafer deposition and can be maintained without needing long baking cycles to recover from atmospheric contamination, resulting in a shorter down time. Additionally, since the growth of phosphide materials is greatly simplified, the complete structure including cladding can be grown in a single step using a faster growth rate for the cladding, thus reducing the total growth time.

1.3.2 State of the art

The first demonstration of continuous-wave operation at room temperature by Beck et al.[73] was achieved by optimizing three key elements: high gain at high temperature was obtained with the help of the four quantum well active region, heat dissipation was maximized by means of buried heterostructure processing and junction down mounting, and finally optical losses were minimized by high-reflection facet coatings. This breakthrough was followed by a rapid development of room temperature CW devices.

In 2003, Yu et al. from Northwestern University, Evaston, IL, USA demonstrated CW operation at λ=6 μm up to a maximum heat-sink temperature of 35°C with an output power of 106 mW at room temperature (25°C)[86]. The authors used a double-phonon resonant design similar to the one previously published by our group[72] and grew their structure by gas source MBE. It is noteworthy that this high level of performance was achieved without the need for buried heterostructure processing or junction down mounting. The samples were processed in double channel ridge waveguides and bonded epilayer up on copper submounts. Efficient heat dissipation was provided by a 5 μm-thick gold layer electroplated around the laser ridges.
Using the same kind of design and technology, the Northwestern University group developed room temperature CW QCLs with output powers higher than 100 mW at wavelengths of 4.8 μm[87], 4.3 μm[88], 5.3 μm[89][90], 4 μm[91], 9.5 μm[92], and 3.8 μm[93]. Record high temperature for CW operation of 90°C was achieved at $\lambda \sim 5.25$ μm with this processing[90], as well as record high CW output power of 640 mW at room temperature with a buried heterostructure processing[89].

High performance QCLs grown by MOVPE have been developed at Agilent Labs, Palo Alto, CA, USA in collaboration with Prof. Capasso's group at Harvard University, Cambridge, MA, USA. In 2005, Troccoli et al. have reported CW operation above room temperature, with an output power in excess of 20 mW at 300 K, of devices based on a three quantum well active region design[96]. This impressive result was achieved using an op-

timized narrow ridge buried heterostructure processing with lateral regrowth of insulating Fe-doped InP. CW operation up to 400 K at 8.4 μm[97] and 380 K at 5.3 μm[98] were later demonstrated by combining this processing with four quantum well active regions.

The best performance of QCLs reported in the literature at the time of writing in terms of highest CW output power at room temperature (295-300 K) and highest CW operation temperature are summarized in Fig 1.8.

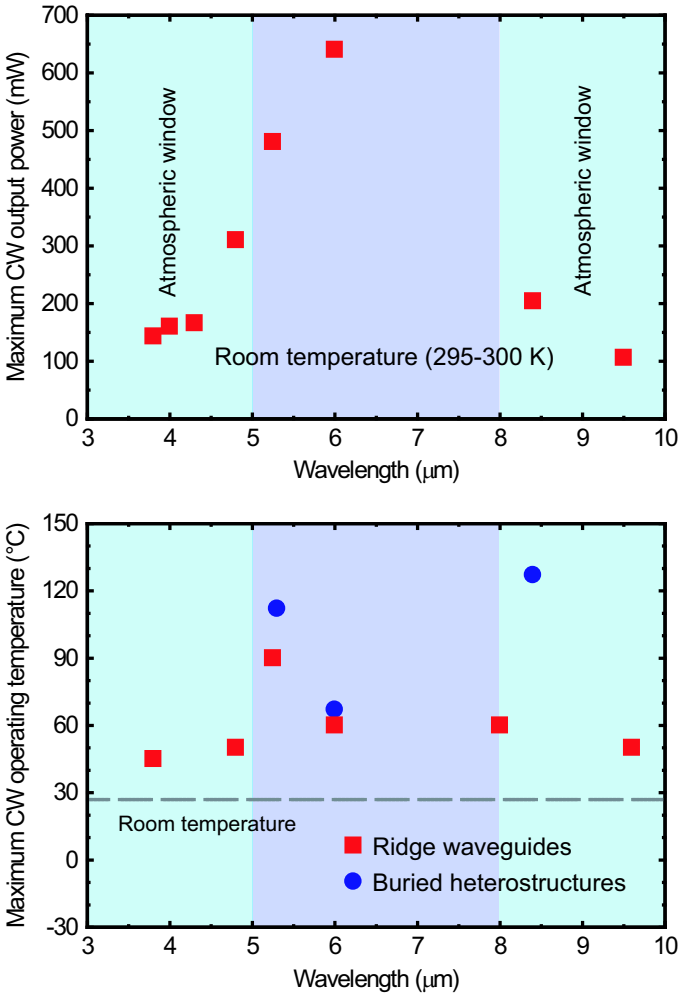

Figure 1.8: Highest CW output power and CW operating temperature reported in the literature at the time of writing.

1.3.3 Single-mode devices

Distributed feedback quantum-cascade lasers

Since the main application of QCLs is gas sensing, an application which needs single-mode tunable devices, distributed feedback QCLs were developed very early. The first realization has been reported in 1997 by Faist et al.[99]. It was a loss-coupled DFB in which the grating was etched on top of the device and covered with metal. In a companion paper the same year, Gmachl et al. reported an index-coupled DFB with the grating etched into an InGaAs layer directly on top of the active region before the regrowth of an InP cladding[100]. This second method, which provides large coupling without degrading the laser performance, is still used for production of high-performance DFB QCLs today.

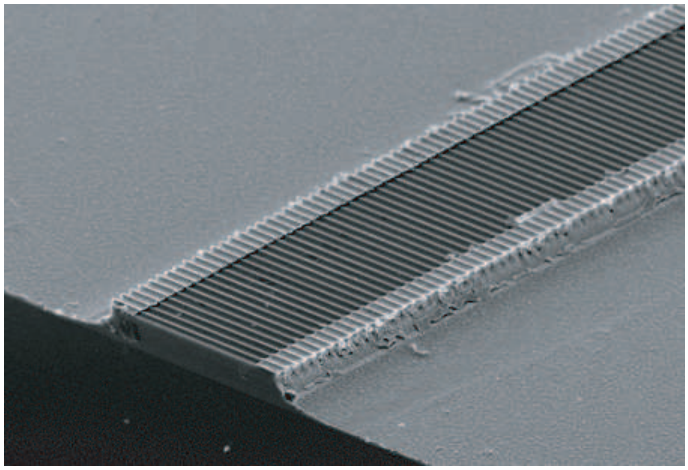

Figure 1.9: Scanning electron microscope (SEM) picture of a distributed feedback QC laser fabricated without epitaxial regrowth. Reprinted from Ref. [104].

The DFB QCLs were developed by the Bell Labs Group[101][102][103], University of Neuchâtel [104][72][105][106], and recently Northwestern University[107][108].
Single-mode devices emitting CW at room temperature based on bound-to-continuum active regions have been developed for commercialization by a collaboration between Alpes Lasers SA, Neuchâtel, Switzerland, and University of Neuchâtel[109][110]. The broad gain spectrum of this design allows the fabrication of high-performance devices over a large wavelength

range, making easier to reach a particular wavelength. Wittmann et al.[110] demonstrated single-mode continuous-wave operation between 7.7 and 8.3 μm from chips fabricated out of the same epilayer with different grating periods.
These lasers have been selected by NASA to be a part of the sample analysis at Mars (SAM) experiment during the Mars science laboratory (MSL) mission that will take off in 2009 and whose goal is to assess whether Mars ever had an environment capable of supporting microbial life.

State of the art DFB QCLs typically show the same level of performance as Fabry-Pérot devices in terms of operating temperature, threshold current density and output power. The side-mode suppression ratio (SMSR) of these devices is commonly larger than 25 dB. In fact, most of the values reported in the literature, generally measured with Fourier transform infrared (FTIR) spectrometers, are instrument limited. Nelson et al. recently investigated the spectral purity of a CW device by scanning its emission wavelength over a NO absorption line[111]. A short reference cell was filled with enough gas to absorb 100% of the light at the line center. The residual transmission when the laser is tuned at line center is a direct indication of its mode purity. They determined this residual transmission to be less than $2{\cdot}10^{-5}$ of the laser intensity, indicating a mode purity greater than 99.99%. DFB QCLs can be tuned by means of thermo-optic effect, either directly by varying the heatsink temperature, or via the injection current. The frequency usually varies with temperature with a coefficient $\mathrm{d}\nu/\mathrm{d}T$ of -0.05 to -0.2 cm^{-1}/K. The typical tuning range on a thermoelectric cooler is thus of the order of 10 cm^{-1}.

External cavity quantum-cascade lasers

DFB QCLs are very convenient light sources for trace gas monitoring in the mid-infrared spectral range. They have the advantages of being compact, delivering several tens of mWs of single-mode radiation with a narrow linewidth, and having simple tuning mechanisms (varying temperature or injection current). However they remain of limited usefulness for spectroscopic investigations because of their limited tuning range, of the order of 10 cm^{-1} on

a thermoelectric cooler, which is quite small compared with gain bandwidth of QC structures (> 100 cm^{-1} FWHM at room temperature).

On the other hand, external cavity semiconductor lasers, in which wavelength selection is achieved with the help of an external dispersive element such as a grating, are less compact and have more complicated tuning mechanisms, but their tuning range is determined only by the bandwidth of the gain medium.

In this section I will go back over the adaptation of this technology to QCLs and the new developments that followed. Since the field is relatively new (5 years old), I will give an exhaustive review of the existing publications.

The first realization of an external cavity quantum cascade laser has been reported in 2001, seven years after the first QCL and four years after the the first DFB QCL, by a collaboration between University of Houston, TX, USA and Applied Optoelectronics Incorporated, Sugar Land, TX, USA[112]. The authors used uncoated chips operated in pulsed mode in a liquid nitrogen dewar with an anti-reflection (AR) coated window. The grating was mounted in Littrow configuration (see Section 2.2) and the output was taken fron the zeroth order reflection. In this first paper, they report tuning ranges of 65 nm (32 cm^{-1}) for a 4.5 μm laser and 88 nm (34 cm^{-1}) for a 5.1 μm laser at 80 K and $\sim$10 cm^{-1} at 203 K. Because the coupling facet was not AR coated, the grating allowed only discrete tuning on the Fabry-Pérot modes of the gain chip.

In a following paper by the same group in 2002[113], an improved tuning range of 140 nm (54 cm^{-1}) at 80 K and still 127 nm (49 cm^{-1}) at 243 K was reported for a 5.1 μm laser. This time, an AR coating with a residual reflectivity of 3-5% was used and continuous wavelength tuning was possible. The grating was again mounted in Littrow configuration, but the light was extracted by a 3% beamsplitter inserted in the cavity.

The same year Totschnig et al. from the University of Technology of Vienna, Austria, using a chip from Alpes Lasers, have reported an EC-QCL operating in pulsed mode at room temperature at a wavelength of 10.4 μm[114]. A smaller tuning range of 7 cm^{-1} was

observed with the coupling facet of the chip left uncoated.

In 2003, Peng et al. from University of Houston, also using a chip from Alpes Lasers, reported a thermoelectrically cooled, pulsed, EC-QCL tunable from 9.08 to 9.36 μm (33 cm^{-1})[115]. An uncoated gain element mounted in Littmann configuration was used and the fine tuning relied on shifting the Fabry-Pérot modes of the chip with temperature. The authors performed spectroscopic absorption measurements of ammonia in order to estimate the laser linewidth. A linewidth of 500-750 MHz was measured, a value very similar to that of pulsed DFB QCLs.
In a following paper the same year, Peng used a two-segment chip for fast, power independent, fine tuning[116]. The chip was operated in pulsed mode at 80 K. A subthreshold current pulse in the 0.75 mm-long phase section preceded the actual current pulse in the 2 mm-long gain section. Varying the integrated energy of the first pulse and/or the delay time before the second one allowed precise control of the cavity phase. The intracavity side of the gain segment waveguide was bent by 6.5° with respect to the normal of the facet to reduce its reflection. A 3 dB modulation bandwidth of 33 kHz was demonstrated for fine tuning.

In 2004, we have demonstrated a broadband tuning of 150 cm^{-1} at $\lambda \cong 10$ μm using a bound-to-continuum active region design with a gain full width at half maximum equal to 297 cm^{-1}[117]. The lasers were operated in pulsed mode at room temperature. As for the aforementioned works, the side mode suppression ratio (SMSR) was relatively poor ($\leq$ 25 dB), but time resolved spectra showed that it was due to Fabry-Pérot modes of the chip lasing at the beginning of the pulses because of their shorter round trip time compared to the grating selected mode. An instrument-limited SMSR of 30 dB was observed after the first 12 ns of the pulse. We concluded that single-mode operation would be observed in CW. The work described in this paper is the subject of Chapter 4.

Another interesting innovation of the University of Houston group, in collaboration with the Bell Labs group, was the realization, in 2005, of an EC-QCL in which the external grating is replaced by an integrated surface-emitting Bragg grating (SEBG) coupler[118]. In

this configuration, shown in Fig. 1.10, the only external elements needed are a mirror and a lens. A two segment approach was again used for separate control of power and wavelength. Coarse tuning over 29 cm^{-1} was achieved by tilting the external mirror and fine tuning over ~ 0.3 cm^{-1} by adjusting the SEBG current.

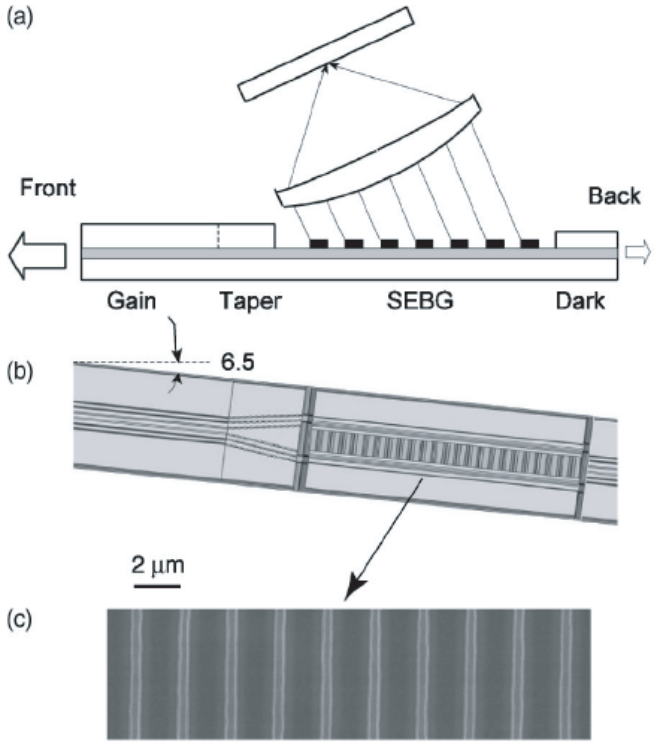

Figure 1.10: Schematic side view (a) and top view (b) of the external cavity QCL with off-band surface-emitting Bragg grating coupler. The drawing is not to scale. (c) SEM image of the grating. Reprinted from Ref. [118].

The same year, we reported CW operation of an EC-QCL on a thermoelectric cooler at a wavelength of 5.2 μm[119]. As expected, single-mode behavior was observed over nearly the whole tuning range. The SMSR was in excess of 30 dB (the instrumental limit) over more than 140 cm^{-1} and in excess of 25 dB over $\sim$170 cm^{-1}. The output power was in excess of 10 mW over $\sim$100 cm^{-1} and in excess of 5 mW over $\sim$130 cm^{-1}. An upper limit to the laser linewidth of 5 MHz was determined by means of an heterodyne beating experiment. The conception and characterization of this laser is reported in Chapter 5.

Very soon after this first demonstration of a CW EC-QCL, we collaborated with Dr. Gerard Wysocki of Prof. Tittel's group at Rice University, Houston, TX, USA to demonstrate the suitability of such a laser for high-resolution spectroscopic applications. The setup was modified to allow mode-hop free tuning, by varying the cavity length together with the chip current and the grating angle, and spectroscopic absorption measurements of NO were performed[120]. More than twenty absorption lines of that gas could be scanned and two peaks separated by 0.006 cm^{-1} could be resolved.

Our last published result to date is an EC-QCL tunable over 265 cm^{-1} (2.25 μm) from 8.2 to 10.4 μm, that is over 24% of the center wavelength, using a gain element with a heterogeneous cascade[121]. The active region consisted of two substacks of 20 periods of bound-to-continuum designs centered at 9.6 and 8.4 μm. Its room temperature spontaneous emission spectrum had a FWHM of 350 cm^{-1} and a variation of intensity of less than 20% over more than 200 cm^{-1}. As in our first paper, the lasers were operated in pulsed mode at room temperature. Time-resolved spectra again showed single-mode operation after the first 12 ns of the pulses. Our work on heterogeneous cascades is presented in Chapter 6.

It's interesting to notice that only four years after the first demonstration of an EC-QCL, a company was already created to develop and sell such lasers. Founded by Dr. Timothy Day, co-founder of New Focus in the early nineties, Daylight Solutions, Poway, CA, USA, adapted the technology of telecommunication external cavity diode lasers (ECDLs) to develop a miniaturized commercial EC-QCL package[122][123]. In particular, miniature MIR aspheric lenses have been developed. Made of molded chalcogenide glass, these lenses have a diameter of 4 mm, and a focal length of less than 2 mm. At the time of writing, the company sells pulsed EC-QCL at wavelengths of 4.5, 5.5, 8.5, 9.5, and 10.5 μm with a tuning range of $\sim$10% of the center wavelength. Nevertheless, the potential of EC-QCLs is not fully exploited. The spectra of these lasers, which contain several modes spanning over $\sim$1 cm^{-1}, are not narrow enough for high-resolution spectroscopy and sensitive gas sensing.

Daylight solution is not the only company involved in the development of EC-QCLs. The development of such a device and its use in a gas sensing application has been recently reported by Pushkarsky et al. from Pranalytica Inc., Santa Monica, CA, USA[124]. The authors built a high power room temperature CW EC-QCL tunable over 75 cm^{-1} centered at 6.25 μm using a chip from Prof. Razeghi's group at Northwestern University. The power was in excess of 160 mW over the whole tuning range with a maximum of 300 mW near the center of the tuning curve. The 4 mm-long, uncoated gain chip was mounted in Littmann configuration. A very long cavity length of 1 m was used so that the extended cavity modes were spaced by only 0.005 cm^{-1} (150 MHz). This device was used to demonstrate photoacoustic spectroscopy of NO_2.

Bibliography

[1] Kincade, Kathy and Stephen Anderson, "Laser Marketplace 2005: Consumer applications boost laser sales 10%", Laser Focus World, **41**, no. 1 (2005).

[2] J. P. Gordon, H. J. Zeiger, and C. H. Townes , "Molecular Microwave Oscillator and New Hyperfine Structure in the Microwave Spectrum of NH3", Phys. Rev. **95**, 282 (1954).

[3] J. P. Gordon, H. J. Zeiger, and C. H. Townes, "The maser–New type of microwave amplifier, frequency standard, and spectrometer", Phys. Rev. **99**, 1264 (1955).

[4] A. L. Schawlow and C. H. Townes, "Infrared and optical masers", Phys. Rev. **112**, 1940 (1958).

[5] T. H. Maiman, "Stimulated optical radiation in ruby", Nature **187**, 493 (1960).

[6] P. P. Sorokin and M. J. Stevenson, "Stimulated infrared emission from trivalent uranium", Phys. Rev. Lett. **5**, 557 (1960).

[7] R. N. Hall, G. E. Fenner, J. D. Kingsley, T. J. Soltys, and R. O. Carlson, "Coherent light emission from GaAs junctions", Phys. Rev. Lett. **9**, 366 (1962).

[8] M. I. Nathan, W. P. Dumke, G. Burns, F. H. Dill, Jr., and G. Lasher, "Stimulated emission of radiation from GaAs p-n junctions", Appl. Phys. Lett. **1**, 62 (1962).

[9] N. Holonyak, Jr. and S. F. Bevacqua, "Coherent (visible) light emission from $Ga(As_{1-x}P_x)$ junctions", Appl. Phys. Lett. **1**, 82 (1962).

[10] T. M. Quist, R. H. Rediker, R. J. Keyes, W. E. Krag, B. Lax, A. L. McWhorter, and H. J. Zeiger, "Semiconductor maser of GaAs", Appl. Phys. Lett. **1**, 91 (1962).

[11] I. Melngailis, "Maser action in InAs diodes", Appl. Phys. Lett. **2**, 176 (1963).

[12] J. F. Butler, A. R. Calawa, R. J. Phelan, Jr., T. C. Harman, A. J. Strauss, and R. H. Rediker, "PbTe diode laser", Appl. Phys. Lett. **5**, 75 (1964).

[13] C. K. N. Patel, "Interpretation of CO_2 optical maser experiments", Phys. Rev. Lett. **12**, 588 (1964).

[14] C. K. N. Patel, "Continuous-wave laser action on vibrational-rotational transitions of CO_2", Phys. Rev. **136**, A1187 (1964).

[15] C.C. Wang and G. W. Racette, "Measurement of parametric gain accompanying optical difference frequency generation", Appl. Phys. Lett. **6**, 169 (1965).

[16] J. A. Giordmaine and R. C. Miller, "Tunable coherent parametric oscillation in LiNbO3 at optical frequencies", Phys. Rev. Lett. **14**, 973 (1965).

[17] J. Faist, F. Capasso, D. L. Sivco, C. Sirtori, A. L. Hutchinson, and A. Y. Cho, "Quantum cascade laser", Science **264**, 553 (1994).

[18] B. N. Murdin, "Key issues for mid-infrared emission", Phil. Trans. R. Soc. A **359**, 459 (2001).

[19] "Solid-State Mid-Infrared Laser Sources", Edited by I.T. Sorokina and K.L. Vodopyanov, Springer Topics Appl. Phys. **89**, 445-510 (2003).

[20] F. K. Tittel, D. Richter, and A. Fried, "Mid-Infrared Laser Applications in Spectroscopy", in *Solid-State Mid-Infrared Laser Sources*, Edited by I.T. Sorokina and K.L. Vodopyanov, Springer Topics Appl. Phys. **89**, 445-510 (2003).

[21] M. B. Pushkarsky, M. E. Webber, and C. K. N. Patel, "Ultra-sensitive ambient ammonia detection using CO_2-laser-based photoacoustic spectroscopy", Appl. Phys. B **77**, 381 (2003).

[22] M. E. Webber, M. Pushkarsky, and C. K. N. Patel, "Optical detection of chemical warfare agents and toxic industrial chemicals: Simulation", J. Appl. Phys. **97**, 113101 (2005).

[23] M. Tacke, "Lead-salt lasers", Phil. Trans. R. Soc. A **359**, 547 (2001).

[24] U. P. Schiessl and J. Rohr, "60 °C lead salt laser emission near 5-μm wavelength", Infrared Phys. Technol. **40**, 325 (1999).

[25] Z. Feit, M. McDonald, R. J. Woods, V. Archambault, and P. Mak, "Low threshold PbEuSeTe/PbTe separate confinement buried heterostructure diode lasers", Appl. Phys. Lett. **68**, 738 (1996).

[26] J. G. Kima, L. Shterengas, R. U. Martinelli, and G. L. Belenky, "High-power room-temperature continuous wave operation of 2.7 and 2.8 mm In(Al)GaAsSb/GaSb diode lasers", Appl. Phys. Lett. **83**, 1926 (2003).

[27] C. Lin, M. Grau, O. Dier, and M.-C. Amann, "Low threshold room-temperature continuous-wave operation of 2.243.04 μm GaInAsSb/AlGaAsSb quantum-well lasers", Appl. Phys. Lett. **84**, 5088 (2004).

[28] C. H. Grein, P. M. Young, and H. Ehrenreich, "Theoretical performance of InAs/ $In_xGa_{1x}Sb$ superlattice-based midwave infrared lasers", J. Appl. Phys. **76**, 1940 (1994).

[29] T. C. Hasenberg, D. H. Chow, A. R. Kost, R. H. Miles, and L. West, "Demonstration of 3.5 μm $Ga_{1-x}In_xSb$/InAs superlattice diode laser", Electron. Lett. **31**, 275 (1995).

[30] J. R. Meyer, C. A. Hoffman, F. J. Bartoli, and L. R. Ram-Mohan, "Type-II quantum-well lasers for the mid-wavelength infrared", Appl. Phys. Lett. **67**, 757 (1995).

[31] C. L. Canedy, W. W. Bewley, J. R. Lindle, I. Vurgaftman, C. S. Kim, M. Kim, and J. R. Meyer, "High-power continuous-wave midinfrared type-II "W" diode lasers", Appl. Phys. Lett. **86**, 211105 (2005).

[32] C. L. Canedy, W. W. Bewley, C. S. Kim, M. Kim, J. R. Lindle, I. Vurgaftman, and J. R. Meyer, "cw midinfrared "W" diode and interband cascade lasers", J. Vac. Sci. Technol. B **24**, 1613 (2006).

[33] R. Q. Yang, "Infrared laser based on intersubband transitions in quantum wells", Superlatt. Microstruct. **17**, 77 1995.

[34] J. R. Meyer, I. Vurgaftman, R. Q. Yang, and L. R. Ram-Mohan, "Type-II and type-I interband cascade lasers", Electron. Lett. **32**, 45 (1996).

[35] C.-H. Lin, R. Q. Yang, D. Zhang, S. J. Murry, S. S. Pei, A. A. Allerman, and S. R. Kurtz, "Type-II interband quantum cascade laser at 3.8 μm", Electron. Lett. **33**, 598 (1997).

[36] I. Vurgaftman, J.R. Meyer, and L.R. Ram-Mohan, "Mid-IR vertical-cavity surface-emitting lasers", IEEE J. Quantum Electron. **34**, 147 (1998).

[37] C.J. Hill, C.M. Wong, B. Yang, and R.Q. Yang, "Type-II interband cascade lasers emitting at wavelengths beyond 5.1 μm", Electron. Lett. **40**, 878 (2004).

[38] K. Mansour, Y. Qiu, C. J. Hill, A. Soibel, and R. Q. Yang , "Mid-infrared interband cascade lasers at thermoelectric cooler temperatures", Electron. Lett. **42**, 1034 (2006).

[39] W. W. Bewley, J. A. Nolde, D. C. Larrabee, C. L. Canedy, C. S. Kim, M. Kim, I. Vurgaftman, and J. R. Meyer", Interband cascade laser operating cw to 257 K at λ=3.7 μm", Appl. Phys. Lett. **89**, 161106 (2006)

[40] W.K. Burns, W. McElhanon, L. Goldberg, "Second harmonic generation in field poled, quasi-phase-matched, bulk $LiNbO_3$", IEEE Photon. Technol. Lett. **6**, 252(1994).

[41] P. E. Powers, Thomas J. Kulp, and S. E. Bisson, "Continuous tuning of a continuous-wave periodically poled lithium niobate optical parametric oscillator by use of a fan-out grating design", Opt. Lett. **23**, 159 (1998).

[42] S. Sanders, R. J. Lang, L. E. Myers, M. M. Fejer, and R. L. Byer, "Broadly tunable mid-IR radiation source based on difference frequency mixing of high power wavelength-tunable laser diodes in bulk periodically poled $LiNbO_3$", Electron. Lett. **32**, 218 (1996).

[43] D. J. M. Stothard, M. Ebrahimzadeh, and M. H. Dunn, "Low-pump-threshold continuous-wave singly resonant optical parametric oscillator," Opt. Lett. **23**, 1895 (1998).

[44] M. van Herpen, S. te Lintel Hekkert, S. E. Bisson, and F. J. M. Harren, "Wide single-mode tuning of a 3.0 - 3.8- μm, 700-mW, continuous-wave Nd:YAG-pumped optical parametric oscillator based on periodically poled lithium niobate ," Opt. Lett. **27**, 640 (2002).

[45] F. Mller, A. Popp, F. Khnemann, and S. Schiller, "Transportable, highly sensitive photoacoustic spectrometer based on a continuous-wave dualcavity optical parametric oscillator", Opt. Express **11**, 2820 (2003).

[46] M. M. J. W. van Herpen, S. E. Bisson, A. K. Y. Ngai, and F. J. M. Harren, "Combined wide pump tuning and high power of a continuous-wave, singly resonant optical parametric oscillator", Appl. Phys. B **78**, 281 (2004).

[47] I. Lindsay, B. Adhimoolam, P. Gro, M. Klein, and K. Boller, "110 GHz rapid, continuous tuning from an optical parametric oscillator pumped by a fiber-amplified DBR diode laser," Opt. Express **13**, 1234 (2005).

[48] M. M. J. W. van Herpen, S. C. Li, S. E. Bisson, F. J. M. Harren, "Photoacoustic trace gas detection of ethane using a continuously tunable, continuous-wave optical parametric oscillator based on periodically poled lithium niobate", Appl. Phys. Lett. **81**, 1157 (2002).

[49] A. K. Y. Ngai, S. T. Persijn, G. von Basum, and F. J. M. Harren, "Automatically tunable continuous-wave optical parametric oscillator for high-resolution spectroscopy and sensitive trace-gas detection", Appl. Phys. B **85**, 173 (2006).

[50] G. Dehlinger, L. Diehl, U. Gennser, H. Sigg, J. Faist, K. Ensslin, D. Grützmacher, and E. Müller, "Intersubband electroluminescence from silicon-based quantum cascade structures", Science **290**, 2277 (2000).

[51] O. Malis, L. N. Pfeiffer, K. W. West, A. M. Sergent, and C. Gmachl, "Mid-infrared hole-intersubband electroluminescence in carbon-doped GaAs/AlGaAs quantum cascade structures", Appl. Phys. Lett. **88**, 081117 (2006).

[52] R. F. Kazarinov and R. A. Suris, "Possibility of the amplification of electromagnetic waves in a semiconductor superlattice", Sov. Phys. Semicond. **5**, 707 (1971).

[53] L. C. West and S. J. Eglash, "First observation of an extremely large-dipole infrared transition within the conduction band of a GaAs quantum well", Appl. Phys. Lett. **46**, 1156 (1985).

[54] M. Helm, P. England, E. Colas, F. DeRosa, and S. J. Allen, Jr., "Intersubband emission from semiconductor superlattices excited by sequential resonant tunneling", Phys. Rev. Lett. **63**, 74 (1989).

[55] F. Capasso, K. Mohammed, and A. Cho, "Resonant tunneling through double barriers, perpendicular quantum transport phenomena in superlattices, and their device applications", IEEE J. Quantum Electron. **22**, 1853 (1986).

[56] P. Yuh and K. L. Wang, "Novel infrared band-aligned superlattice laser", Appl. Phys. Lett. **51**, 1404 (1987).

[57] H. C. Liu, "A novel superlattice infrared source", J. Appl. Phys. **63**, 2856 (1988).

[58] S. I. Borenstain and J. Katz, "Evaluation of the feasibility of a far-infrared laser based on intersubband transitions in GaAs quantum wells", Appl. Phys. Lett. **55**, 654 (1989).

[59] A. Kastalsky, V. J. Goldman, and J. H. Abeles, "Possibility of infrared laser in a resonant tunneling structure", Appl. Phys. Lett. **59**, 2636 (1991).

[60] Q.Hu and S. Feng, "Feasibility of far-infrared lasers using multiple semiconductor quantum wells", Appl. Phys. Lett. **59**, 2923 (1991).

[61] J. Faist, F. Capasso, C. Sirtori, D. L. Sivco, A. L. Hutchinson, S. N. G. Chu, and A. Y. Cho, "Narrowing of the intersubband electroluminescent spectrum in coupled-quantum-well heterostructures", Appl. Phys. Lett. **65**, 94 (1994).

[62] T. Aellen, R. Maulini, R. Terazzi, N. Hoyler, M. Giovannini, J. Faist, S. Blaser, and L. Hvozdara, "Direct measurement of the linewidth enhancement factor by optical heterodyning of an amplitude-modulated quantum cascade laser", Appl. Phys. Lett. **89**, 91121 (2006).

[63] J. Faist, F. Capasso, C. Sirtori, D. L. Sivco, A. L. Hutchinson, and A. Y. Cho, "Vertical transition quantum cascade laser with Bragg confined excited state", Appl. Phys. Lett. **66**, 538 (1995).

[64] J. Faist, F. Capasso, C. Sirtori, D. L. Sivco, J. N. Baillargeon, A. L. Hutchinson, S.-N. G. Chu, and A. Y. Cho, "High power mid-infrared ($\lambda \sim 5$ μm) quantum cascade lasers operating above room temperature", Appl. Phys. Lett. **68**, 3680 (1996).

[65] J. Faist, F. Capasso, D. L. Sivco, A. L. Hutchinson, S.-N. G. Chu, and A. Y. Cho, "Short wavelength ($\lambda \sim 3.4$ μm) quantum cascade laser based on strained compensated InGaAs/AlInAs", Appl. Phys. Lett. **72**, 680 (1998).

[66] C. Gmachl, F. Capasso, A. Tredicucci, D. L. Sivco, A. L. Hutchinson, and A. Y. Cho, "Long wavelength ($\lambda \simeq 13$ μm) quantum cascade lasers", Electron. Lett. **34**, 1103 (1998).

[67] G. Scamarcio, F. Capasso, C. Sirtori, J. Faist, A. L. Hutchinson, D. L. Sivco, and A. Y. Cho, "High-power infrared (8-micrometer wavelength) superlattice lasers", Science bf 276, 773 (1997).

[68] A. Tredicucci, F. Capasso, C. Gmachl, D. L. Sivco, A. L. Hutchinson, A. Y. Cho, J. Faist, and G. Scamarcio, "High-power inter-miniband lasing in intrinsic superlattices", Appl. Phys. Lett. **72**, 2388 (1998).

[69] A. Tredicucci, F. Capasso, C. Gmachl, D. L. Sivco, A. L. Hutchinson, and A. Y. Cho, "High performance interminiband quantum cascade lasers with graded superlattices", Appl. Phys. Lett. **73**, 2101 (1998)

[70] R. Colombelli, F. Capasso, C. Gmachl, A. L. Hutchinson, D. L. Sivco, A. Tredicucci, M. C. Wanke, A. M. Sergent, and A. Y. Cho, "Far-infrared surface-plasmon quantum-cascade lasers at 21.5 μm and 24 μm wavelengths", Appl. Phys. Lett. **78**, 2620 (2001).

[71] J. Faist, M. Beck, T. Aellen, and E. Gini, "Quantum-cascade lasers based on a bound-to-continuum transition", Appl. Phys. Lett. **78**, 147 (2001).

[72] D. Hofstetter, M. Beck, T. Aellen, and J. Faist, "High-temperature operation of distributed feedback quantum-cascade lasers at 5.3 μm", Appl. Phys. Lett. **78**, 396 (2001).

[73] M. Beck, D. Hoffstetter, T. Aellen, J. Faist, U. Oesterle, M. Ilegems, E. Gini and H. Melchior, "Continuous-wave operation of a mid-infrared semiconductor laser at room-temperature", Science **295**, 301 (2002).

[74] C. Gmachl, D.L. Sivco, J. N. Baillargeon, A. L. Hutchinson, F. Capasso, and A. Y. Cho, "Quantum cascade lasers with a heterogeneous cascade: Two-wavelength operation", Appl. Phys. Lett. **79**, 572 (2001)

[75] C. Gmachl, D. L. Sivco, R. Colombelli, F. Capasso, and A. Y. Cho, "Ultra-broadband semiconductor laser", Nature (London) **415**, 883 (2002).

[76] C. Sirtori, P. Kruck, S. Barbieri, P. Collot, J. Nagle, M. Beck, J. Faist, and U. Oesterle, "GaAs/$Al_xGa_{1-x}As$ quantum cascade lasers", Appl. Phys. Lett. **73**, 3486 (1998).

[77] L. R. Wilson, D. A. Carder, J. W. Cockburn, R. P. Green, D. G. Revin, M. J. Steer, M. Hopkinson, G. Hill, and R. Airey, "Intervalley scattering in GaAsAlAs quantum cascade lasers", Appl. Phys. Lett. **81**, 1378 (2002).

[78] J. Ulrich, J. Kreuter, W. Schrenk, G. Strasser, and K. Unterrainer, "Long wavelength (15 and 23 μm) GaAs/AlGaAs quantum cascade lasers", Appl. Phys. Lett. **80**, 3691 (2002).

[79] R. Köhler, A. Tredicucci, F. Beltram, H. E. Beere, E. H. Linfield, A. G. Davies, D. A. Richie, R. C. Lotti, and F. Rossi, "Terahertz semiconductor-heterostructure laser", Nature (London) **417**, 156 (2002).

[80] Ch. Walther, G. Scalari, M. Fischer, N. Hoyler, and J. Faist, unpublished results (2006).

[81] B. Williams, S. Kumar, Q. Hu, and J. Reno, "Operation of terahertz quantum-cascade lasers at 164 K in pulsed mode and at 117 K in continuous-wave mode", Opt. Express **13**, 3331 (2005).

[82] K. Ohtani and H. Ohno, "InAs/AlSb quantum cascade lasers operating at 10 μm", Appl. Phys. Lett. **82**, 1003 (2003).

[83] J. Devenson, D. Barate, O. Cathabard, R. Teissier, and A. N. Baranov, "Very short wavelength (λ=3.13.3 μm) quantum cascade lasers", Appl. Phys. Lett. **89**, 191115 (2006).

[84] D. G. Revin, L. R. Wilson, E. A. Zibik, R. P. Green, J. W. Cockburn, M. J. Steer, R. J. Airey, and M. Hopkinson, "InGaAs/AlAsSb quantum cascade lasers", Appl. Phys. Lett. **85**, 3992 (2004).

[85] Q. Yang, C. Manz, W. Bronner, K. Khler, and J. Wagner, "Room-temperature short-wavelength (λ ~3.73.9 μm) GaInAs/AlAsSb quantum-cascade lasers", Appl. Phys. Lett. **88**, 121127 (2006).

[86] J. S. Yu, S. Slivken, A. Evans, L. Doris, and M. Razeghi, "High-power continuous-wave operation of a 6 μm quantum-cascade laser at room temperature", Appl. Phys. Lett. **83**, 2503 (2003).

[87] A. Evans, J. S. Yu, S. Slivken, and M. Razeghi, "Continuous-wave operation of λ ~4.8 μm quantum-cascade lasers at room temperature", Appl. Phys. Lett. **85**, 2166 (2004).

[88] J.S. Yu, A. Evans, S. Slivken, S.R. Darvish, M. Razeghi, "Short wavelength (λ ~4.3 μm) high-performance continuous-wave quantum-cascade lasers", IEEE Photon. Technol. Lett. **17**, 1154 (2005).

[89] W. W. Bewley, J. R. Lindle, C. S. Kim, I. Vurgaftman, J. R. Meyer, A. J. Evans, J. S. Yu, S. Slivken, and M. Razeghi, "Beam Steering in High-Power CW Quantum Cascade Lasers", IEEE J. Quantum Electron. **41**, 883 (2005).

[90] A. Evans, J. Nguyen, S. Slivken, J. S. Yu, S. R. Darvish, and M. Razeghi, "Quantum-cascade lasers operating in continuous-wave mode above 90 °C at λ ~5.25 μm", Appl. Phys. Lett. **88**, 051105 (2006).

[91] J. S. Yu, S. R. Darvish, A. Evans, J. Nguyen, S. Slivken, and M. Razeghi, "Room-temperature continuous-wave operation of quantum-cascade lasers at λ ~4 μm", Appl. Phys. Lett. **88**, 041111 (2006).

[92] J. S. Yu, S. Slivken, A. Evans, S. R. Darvish, J. Nguyen, and M. Razeghi, "High-power λ ~9.5 μm quantum-cascade lasers operating above room temperature in continuous-wave mode", Appl. Phys. Lett. **88**, 091113 (2006).

[93] J. S. Yu, A. Evans, S. Slivken, S. R. Darvish, and M. Razeghi, "Temperature dependent characteristics of $\lambda \sim 3.8$ μm room-temperature continuous-wave quantum-cascade lasers", Appl. Phys. Lett. **88**, 251118 (2006).

[94] J. S. Roberts, R. P. Green, L. R. Wilson, E. A. Zibik, D. G. Revin, J. W. Cockburn, and R. J. Airey, "Quantum cascade lasers grown by metalorganic vapor phase epitaxy", Appl. Phys. Lett. **82**, 4221 (2003).

[95] R. P. Green, A. Krysa, J. S. Roberts, D. G. Revin, L. R. Wilson, E. A. Zibik, W. H. Ng, and J. W. Cockburn, "Room-temperature operation of InGaAs/AlInAs quantum cascade lasers grown by metalorganic vapor phase epitaxy", Appl. Phys. Lett. **83**, 1921 (2003).

[96] M. Troccoli, S. Corzine, D. Bour, J. Zhu, O. Assayag, L. Diehl, B. G. Lee, G. Höfler, and F. Capasso, "Room temperature continuous-wave operation of quantum-cascade lasers grown by metal organic vapour phase epitaxy", Electron. Lett. **41**, 1059 (2005).

[97] L. Diehl, D. Bour, S. Corzine, J. Zhu, G. Höfler, M. Lončar, M. Troccoli, and F. Capasso, "High-power quantum cascade lasers grown by low-pressure metal organic vapor-phase epitaxy operating in continuous wave above 400 K", Appl. Phys. Lett. **88**, 201115 (2006).

[98] L. Diehl, D. Bour, S. Corzine, J. Zhu, G. Höfler, M. Lončar, M. Troccoli, and F. Capasso, "High-temperature continuous wave operation of strain-balanced quantum cascade lasers grown by metal organic vapor-phase epitaxy", Appl. Phys. Lett. **89**, 081101 (2006).

[99] J. Faist, C. Gmachl, F. Capasso, C. Sirtori, D. L. Sivco, J. N. Baillargeon, and A. Y. Cho, "Distributed feedback quantum cascade lasers", Appl. Phys. Lett. **70**, 2670 (1997).

[100] C. Gmachl, J. Faist, J.N. Bailargeon, F. Capasso, C. Sirtori, D.L. Sivco, S.N.G. Chu, A.Y. Cho, "Complex-coupled quantum cascade distributed-feedback laser", IEEE Photon. Technol. Lett. **9**, 1090 (1997).

[101] C. Gmachl, F. Capasso, J. Faist, A. L. Hutchinson, A. Tredicucci, D. L. Sivco, J. N. Baillargeon, S. N. G. Chu, and A. Y. Cho, "Continuous-wave and high-power pulsed operation of index-coupled distributed feedback quantum cascade laser at 8.5 μm", Appl. Phys. Lett. **72**, 1430 (1998).

[102] C. Gmachl, F. Capasso, A. Tredicucci, D. L. Sivco, J. N. Baillargeon, A. L. Hutchinson, and A. Y. Cho, "High-power, continuous-wave, current-tunable, single-mode quantum-cascade distributed-feedback lasers at $\lambda \sim 5.2$ and $\lambda \sim 7.95$ μm," Opt. Lett. **25**, 230 (2000).

[103] R. Köhler, C. Gmachl, F. Capasso, A. Tredicuddi, D. L. Sivco, S. N. G. Chu, and A. Cho, "Single-mode tunable, pulsed, and continuous wave quantum-cascade distributed feedback lasers at $\lambda \cong 4.64.7$ μm", Appl. Phys. Lett. **76**, 1092 (2000).

[104] D. Hofstetter, J. Faist, M. Beck, A. Mller, and U. Oesterle, "Demonstration of high-performance 10.16 μm quantum cascade distributed feedback lasers fabricated without epitaxial regrowth", Appl. Phys. Lett. **75**, 665 (1999).

[105] M. Rochat, D. Hofstetter, M. Beck, and J. Faist, "Long wavelength ($\lambda \sim$16 μm), room-temperature, single frequency quantum-cascade lasers based on a bound-to-continuum transition", Appl. Phys. Lett. **79**, 4271 (2001).

[106] T. Aellen, S. Blaser, M. Beck, D. Hofstetter, J. Faist, and E. Gini, "Continuous-wave distributed-feedback quantum-cascade lasers on a Peltier cooler", Appl. Phys. Lett. **83**, 1929 (2003).

[107] J. S. Yu, S. Slivken, S. R. Darvish, A. Evans, B. Gokden, and M. Razeghi, "High-power, room-temperature, and continuous-wave operation of distributed-feedback quantum-cascade lasers at $\lambda \sim$4.8 μm", Appl. Phys. Lett. **87**, 041104 (2005).

[108] S. R. Darvish, S. Slivken, A. Evans, J. S. Yu, and M. Razeghi, "Room-temperature, high-power, and continuous-wave operation of distributed-feedback quantum-cascade lasers at $\lambda \sim$9.6 μm", Appl. Phys. Lett. **88**, 201114 (2006).

[109] S. Blaser, D. A. Yarekha, L. Hvozdara, Y. Bonetti, A. Muller, M. Giovannini, and J. Faist, "Room-temperature, continuous-wave, single-mode quantum-cascade lasers at $\lambda \simeq$5.4 μm", Appl. Phys. Lett. **86**, 41109 (2005).

[110] A. Wittmann, M. Giovannini, J. Faist, L. Hvozdara, S. Blaser, D. Hofstetter, and E. Gini, "Room temperature, continuous wave operation of distributed feedback quantum cascade lasers with widely spaced operation frequencies", Appl. Phys. Lett. **89**, 141116 (2006).

[111] D. D. Nelson, J. B. McManus, S. C. Herndon, J. H. Shorter, M. S. Zahniser, S. Blaser, L. Hvozdara, A. Muller, M. Giovannini, and J. Faist, "Characterization of a near-room-temperature, continuous-wave quantum cascade laser for long-term, unattended monitoring of nitric oxide in the atmosphere", Opt. Lett. **31**, 2012 (2006).

[112] G. P. Luo, C. Peng, H. Q. Le, S. S. Pei, W.-Y. Hwang, B. Ishaug, J. Um, J. N. Baillargeon, and C.-H. Lin, "Grating-tuned external-cavity quantum-cascade semiconductor lasers", Appl. Phys. Lett. **78**, 2834 (2001).

[113] G. Luo, C. Peng, H. Q. Le, S.-S. Pei, H. Lee, W.-Y. Hwang, B. Ishaug, and J. Zheng, "Broadly wavelength-tunable external cavity, mid-infrared quantum cascade lasers", IEEE J. Quantum Electron. **38**, 486 (2002).

[114] G. Totschnig, F. Winter, V. Pustogov, J. Faist, and A. Mller, "Mid-infrared external-cavity quantum-cascade laser", Opt. Lett. **27**, 1788 (2002).

[115] C. Peng, G. Luo, H. Q. Le , "Broadband, continuous, and fine-tune properties of external-cavity thermoelectric-stabilized mid-infrared quantum-cascade lasers", Appl. Opt. **42**, 4877 (2003).

[116] C. Peng, H. L. Zhang, and H. Q. Le, "Mid-infrared external-cavity two-segment quantum-cascade laser", Appl. Phys. Lett. **83**, 4098 (2003).

[117] R. Maulini, M. Beck, J. Faist, and E. Gini, "Broadband tuning of external cavity bound-to-continuum quantum-cascade lasers", Appl. Phys. Lett. **84**, 1659 (2004).

[118] H. L. Zhang, C. Peng, A. Seetharaman, G. P. Luo, H. Q. Le, C. Gmachl, D. L. Sivco, and A. Y. Cho, "External-cavity tunable mid-infrared laser using off-band surface-emitting Bragg grating coupler" Appl. Phys. Lett. **86**, 111112 (2005).

[119] R. Maulini, D. A. Yarekha, J.-M. Bulliard, M. Giovannini, J. Faist, and E. Gini, "Continuous-wave operation of a broadly tunable thermoelectrically cooled external cavity quantum-cascade laser", Opt. Lett. **30**, 2584 (2005).

[120] G. Wysocki, R. F. Curl, F. K. Tittel, R. Maulini, J. M. Bulliard, and J. Faist, "Widely tunable mode-hop free external cavity quantum cascade laser for high resolution spectroscopic applications", Appl. Phys. B **81**, 769 (2005).

[121] R. Maulini, A. Mohan, M. Giovannini, J. Faist, and E. Gini, "External cavity quantum-cascade laser tunable from 8.2 to 10.4 μm using a gain element with a heterogeneous cascade", Appl. Phys. Lett. **88**, 201113 (2006).

[122] T. Day, D. Arnone, S. F. Crivello, and M. J. Weida, "Miniaturized external cavity quantum cascade lasers for broad tunability in the mid-infrared," in CLEO/QELS 06 Technical Digest (CD), (Optical Society of America, 2006), paper CTuFF5.

[123] M. J. Weida, D. Arnone, and T. Day, "Tunable QC laser opens up mid-IR sensing applications", Laser Focus World, July 2006, S13 (2006).

[124] M. Pushkarsky, A. Tsekoun, I. G. Dunayevskiy, R. Go, and C. K. N. Patel, "Sub-parts-per-billion level detection of NO_2 using room-temperature quantum cascade lasers", Proc. Natl. Acad. Sci. USA **103**, 10846 (2006).

Chapter 2

Theory

2.1 Quantum cascade lasers

2.1.1 Electronic states in heterostructures

The active region of a quantum cascade laser is a planar semiconductor heterostructure whose conduction band edge profile along the growth axis $E_c(z)$ is designed to create localized electronic subbands by quantum confinement. The building blocks for this bandstructure engineering are quantum wells, as illustrated in Figure 2.1.

We computed the eigenstates of our heterostructures in the envelope function formalism[1]. In this approximation the wavefunctions are written as

$$\psi(\mathbf{r}) = \sum_m \varphi_m(\mathbf{r})\, u_{m,\mathbf{k}=0}(\mathbf{r}) \tag{2.1}$$

where m runs over the N bands taken into account in the model, $u_{m,\mathbf{k}=0}(\mathbf{r})$ is the Bloch function at the edge of band m, and $\varphi_m(\mathbf{r})$ is a slowly varying envelope function. The Bloch functions are assumed to be the same in all the layers of the heterostructure. Because of the translation invariance in the plane of the layers, one has

$$\varphi_m(\mathbf{r}) = \frac{1}{\sqrt{A}}\, e^{i(k_x x + k_y y)}\, \chi_m(z) = \frac{1}{\sqrt{A}}\, e^{i\mathbf{k}_\parallel \cdot \mathbf{r}_\parallel}\, \chi_m(z) \tag{2.2}$$

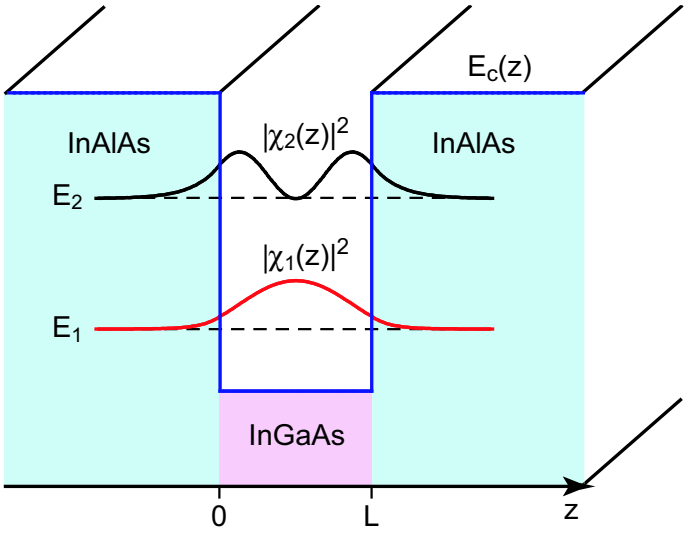

Figure 2.1: Schematic illustration of an InGaAs/InAlAs quantum well heterostructure with the moduli squared of the envelope functions. The wavefunctions are confined along the growth axis z and delocalized (plane waves) in the plane of the layers.

where A is the sample area. The envelope functions can be written as the product of a plane wave propagating parallel to the layers and an N-component envelope function χ depending only on z determined by the band edge profiles $E_m(z)$.

In the most general case, an eight band model has to be used to take into account the heavy-hole, light-hole, and split-off valence bands, the conduction band, and the spin degree of freedom. In absence of magnetic field, the spin degeneracy allows to reduce the number of bands to four. Since we are interested only in the conduction band states, we used an effective two-band model in which only one valence band is considered[2]. This model was previously shown to predict the correct confinement energies with an accuracy of a few meVs[3].

We neglect the dependence of the envelope function on the in-plane momentum and solve only for $\mathbf{k}_{\|} = (k_x, k_y) = 0$. The wavefunction is written as

$$\psi(\mathbf{r}) = \chi_c(z)\, u_{c,\mathbf{k}=0}(\mathbf{r}) + \chi_v(z)\, u_{v,\mathbf{k}=0}(\mathbf{r}) \tag{2.3}$$

where $u_{c,\mathbf{k}=0}$ and $u_{v,\mathbf{k}=0}$ are the conduction and valence band Bloch functions at the center of

the Brillouin zone and $\chi(z) = \Big(\chi_c(z), \chi_v(z)\Big)$ the envelope function. In this approximation, the conduction band component of the envelope wavefunction has to satisfy the Schrödinger-like equation

$$\Big[-\frac{\hbar^2}{2}\frac{\mathrm{d}}{\mathrm{d}z}\frac{1}{m^*(E,z)}\frac{\mathrm{d}}{\mathrm{d}z} + E_c(z)\Big]\chi_c(z) = E\,\chi_c(z) \tag{2.4}$$

where the energy dependent effective mass $m^*(E) = m^*(E_c)\Big[1+\frac{E-E_c}{E_G}\Big]$ accounts for the band non parabolicity.

This equation leads to the Bastard boundary conditions[4] at an interface between two materials A and B:

$$\chi_c^{(A)}(z) = \chi_c^{(B)}(z) \tag{2.5}$$

$$\frac{1}{m_A^*(E,z)}\frac{\mathrm{d}\chi_c^{(A)}(z)}{\mathrm{d}z} = \frac{1}{m_B^*(E,z)}\frac{\mathrm{d}\chi_c^{(B)}(z))}{\mathrm{d}z} \tag{2.6}$$

Since the coupling to the valence band is small, the conduction band wavefunctions $\chi_c(z)$ is a good approximation for the complete envelope function $\chi(z)$. We compute this component by solving numerically Equ. 2.4 by means of a shooting method. The effect of the applied electric field is taken into account by digitizing the potential in 0.1 to 1 nm steps. To get rid of the normalization problems associated with scattering states, we enclose the whole structure in a large quantum well.

In order to evaluate correctly the relevant physical quantities such as dipole matrix elements, lifetimes, etc. one has to use formulas which take into account the effect of the valence band part of the wavefunction. In particular, since χ_c is not the complete wavefunction, it should not be normalized to 1, but according to[5]

$$\left\langle \chi_{c,i} \middle| 1 + \frac{E_i - E_c(z)}{E_i - E_v(z)} \middle| \chi_{c,i} \right\rangle = 1 \tag{2.7}$$

For the dipole matrix element between two states $z_{ij} = \langle\chi_i|z|\chi_j\rangle$, which is a key quantity because it determines the optical coupling between these states, the influence of the valence

band part leads to the formula

$$z_{ij} = \frac{-i\hbar}{2(E_i - E_j)} \left\langle \chi_{c,i} \middle| p_z \frac{1}{m^*(E_i, z)} + \frac{1}{m^*(E_j, z)} p_z \middle| \chi_{c,j} \right\rangle \tag{2.8}$$

where the momentum operator is defined as $p_z = -i\hbar\frac{\partial}{\partial z}$.

2.1.2 Intersubband relaxation times

The population inversion in quantum cascade lasers does not rely on an intrinsic property of the material but is obtained by a careful design of the lifetimes. It is thus crucial to be able to evaluate the scattering times between subbands. Nonradiative intersubband transitions are induced by impurity scattering, interface roughness scattering, acoustical and optical phonon scattering and electron-electron scattering. For subbands spaced by more than an optical phonon energy $\hbar\omega_{\mathrm{LO}}$, the most efficient process is the optical phonon scattering[6]. We took into account only this process. The scattering time between two subbands i and f is computed for emission and absorption of bulk phonons, following Ferreira and Bastard's approach[6]. Since the sheet density in the excited subbands is always low, we assume the electron to be at $\mathbf{k}_{\|} = 0$ in subband i. At zero temperature, the scattering rate τ_{if}^{-1} is equal to the rate of spontaneous emission of phonons

$$\frac{1}{\tau_{\mathrm{em}}} = \frac{\pi m^* e^2 \omega_{\mathrm{LO}}}{\hbar^2 \epsilon_\rho \, q_{if}} \int \mathrm{d}z \int \mathrm{d}z' \, \chi_i(z)\chi_f(z) e^{-q_{if}|z-z'|} \chi_i(z')\chi_f(z') \tag{2.9}$$

where $q_{if} = \sqrt{2m^*(E_i - E_f - \hbar\omega_{\mathrm{LO}})}/\hbar$ is the norm of the in-plane transfered momentum and $\epsilon_\rho^{-1} = \epsilon_\infty^{-1} - \epsilon_s^{-1}$, ϵ_∞ and ϵ_s being the high-frequency and static relative dielectric constants, respectively. To simplify the numerical evaluation, we neglected the contribution of the valence band component of the envelope function. This formula leads to lifetimes of the order of a few picoseconds, with a minimum of ≈ 0.25 ps when the subband spacing is resonant with $\hbar\omega_{\mathrm{LO}}$.

At nonzero temperature, absorption and stimulated emission processes are possible as well,

and the scattering rate reads

$$\tau_{if}^{-1} = (1+n)\ \tau_{\mathrm{em}}^{-1} + n\ \tau_{\mathrm{abs}}^{-1} \tag{2.10}$$

where τ_{abs} is computed similarly to τ_{em}, but with $q_{if} = \sqrt{2m^*(E_i - E_f + \hbar\omega_{\mathrm{LO}})}/\hbar$, and n is the thermal population of optical phonons (Bose-Einstein factor):

$$n = \left[\exp\left(\frac{\hbar\omega_{\mathrm{LO}}}{kT}\right) - 1\right]^{-1} \tag{2.11}$$

The LO phonon scattering lifetime is very weakly dependent on temperature. In the InGaAs material, which has an optical phonon energy $\hbar\omega_{\mathrm{LO}} = 34$ meV, the ratio between room temperature and zero temperature lifetimes is as high as $\tau(300\ \mathrm{K})/\tau(0\ \mathrm{K}) \cong 0.58$.

2.1.3 Spontaneous emission and gain between subbands

The rate of spontaneous emission of photons between subbands is obtained in the framework of quantum electrodynamics by applying Fermi's golden rule to the electric dipole hamiltonian $H_{DE} = -q\mathbf{E}\cdot\mathbf{r}$. One finds

$$\frac{1}{\tau_{\mathrm{sp}}} = W_{ij}^{sp} = \frac{e^2 n}{3\pi c^3 \varepsilon_0 \hbar^4} E_{ij}^3 |z_{ij}|^2 \tag{2.12}$$

where $E_{ij} = E_i - E_j$ is the energy of the transition, $z_{ij} = \langle\chi_i|z|\chi_j\rangle$ is called the dipole matrix element, and n is the refractive index of the medium.

The absorption or gain in presence of an electromagnetic field in the cavity is related to the spontaneous emission rate by the Einstein's equations. In presence of an inverted population, the material gain (in cm^{-1}) reads[3]

$$G(E) = \frac{2\pi^2 e^2 |z_{ij}|^2}{\varepsilon_0 n \lambda_{ij}} \frac{n_i - n_j}{L_p} L(E - E_{ij}) \tag{2.13}$$

where $\lambda_{ij} = hc/E_{ij}$ is the photon wavelength in vacuum, L_p is a normalization length chosen as the length of one period in the case of quantum cascade lasers and $L(E - E_{ij})$ is the

normalized lineshape function of the transition, usually assumed to be lorentzian:

$$L(E - E_{ij}) = \mathcal{L}(E - E_{ij}, \gamma_{ij}) = \frac{1}{\pi} \frac{\gamma_{ij}}{(E - E_{ij})^2 + \gamma_{ij}^2} \tag{2.14}$$

The full width at half maximum $2\gamma_{ij}$ of the transition is determined from the luminescence spectrum. The peak material gain G_p is inversely proportional to the linewidth:

$$G_p(E) = \frac{2\pi e^2}{\varepsilon_0 n \lambda_{ij}} \frac{|z_{ij}|^2}{\gamma_{ij} L_p} (n_i - n_j) \tag{2.15}$$

The modal gain is given by $G_M(E) = G(E)\Gamma$ where Γ is the overlap factor of the electromagnetic mode with the active region. It is often useful to define also the gain cross section $g_c(E)$ (in cm) of the transition and the differential gain $g(E)$ (in cm/kA) which are related to the modal gain by $G_M = g_c \Delta n = gJ$.

2.1.4 Intersubband absorption linewidth

As we have seen in the previous section, the intersubband absorption linewidth $2\gamma_{ij}$ has a determinant influence on the performance of quantum cascade lasers since it is inversely proportinal to the peak gain. Unuma et al. have shown theoretically and experimentally that the dominant scattering mechanism responsible for the linewidth broadening in quantum wells is interface roughness scattering[7][8]. This broadening is of course dependent on the growth, but relative broadening for different transitions can nevertheless be computed using Ando's theory[9].

The roughness $h(\mathrm{r}_\parallel)$ is assumed to have a gaussian autocorrelation function

$$\langle h(\mathrm{r}_\parallel) h(\mathrm{r}'_\parallel) \rangle = \Delta^2 \exp\Big(- \frac{|r_\parallel - r'_\parallel|^2}{\Lambda^2} \Big) \tag{2.16}$$

with an average height Δ and an in-plane correlation length Λ. This leads to, in the case of a single quantum well[7]

$$\gamma_{ij} = \frac{m^*\Delta^2\Lambda^2}{2\hbar^2}(F_{ii} - F_{jj})^2 \int_0^\pi \mathrm{d}\theta\, e^{-q^2\Lambda^2/4} \tag{2.17}$$

where $F_{ii} = |\partial E_i/\partial L|$, L being the well width, and $q^2 = 4m^*E(1-\cos\theta)/\hbar^2$. For a multi-quantum well structure like the quantum cascade laser, one has to take into account the contributions $F_{ii}^k = |\partial E_i/\partial z_k|$ of all the interfaces z_k[10]. Since the wavefunctions are known, one can use the more convenient expression $F_{ii}^k = \Delta E_c|\chi_i(z_k)|^2$.

$$\gamma_{ij} = \frac{m^*\Delta^2\Lambda^2}{2\hbar^2}\Delta E_c^2 \sum_k \left\{|\chi_i(z_k)|^2 - |\chi_j(z_k)|^2\right\}^2 \int_0^\pi \mathrm{d}\theta e^{-q^2\Lambda^2/4} \tag{2.18}$$

To compute γ_{ij} with this formula, one needs to know the growth-dependent parameters Δ and Λ which are difficult to estimate, but this formula allows to predict ratios between the linewidths of different structures grown in the same conditions.

We used this theory to compute the relative broadenings of the various transitions of a bound-to-continuum active region in order to reduce the number of free parameters needed to describe the spontaneous emission lineshape (see Section 4.2.2).

2.1.5 Rate equations

We described the transport in the active region by means of a rate equation model[3]. This set of equations describes the time evolution of the electronic populations (cm^{-2} per period) of the upper and lower states of the radiative transition, labeled 3 and 2 for historical reasons, because the model was applied first to a three quantum well active region which is a three level system, coupled to the photon flux density S ($\mathrm{cm}^{-1}\mathrm{s}^{-1}$ per period):

$$\frac{\mathrm{d}n_3}{\mathrm{d}t} = \frac{J}{e} - \frac{n_3}{\tau_3} - Sg_c(n_3 - n_2) \tag{2.19}$$

$$\frac{\mathrm{d}n_2}{\mathrm{d}t} = \frac{n_3}{\tau_{32}} + Sg_c(n_3 - n_2) - \frac{n_2 - n_2^{\mathrm{therm}}}{\tau_2} \tag{2.20}$$

$$\frac{\mathrm{d}S}{\mathrm{d}t} = \frac{c}{n}\Big[\Big(g_c(n_3 - n_2) - \alpha_{tot}\Big)S + \beta\frac{n_3}{\tau_{\mathrm{sp}}}\Big] \tag{2.21}$$

where τ_3 and τ_2 are the lifetimes of states 3 and 2, τ_{32} is the nonradiative relaxation time from level 3 to level 2, g_c is the peak gain cross section, n_2^{therm} is the thermal population (backfilling) of level 2, $\alpha_{\mathrm{tot}} = \alpha_w + \alpha_{m,1} + \alpha_{m,2}$ are the total optical losses, which are equal to the sum of the waveguide losses α_w and the mirror losses $\alpha_{m,i} = \frac{1}{2L}\ln\frac{1}{R_i}$ of the two facets, and β is the fraction of the spontaneous light emitted into the lasing mode.

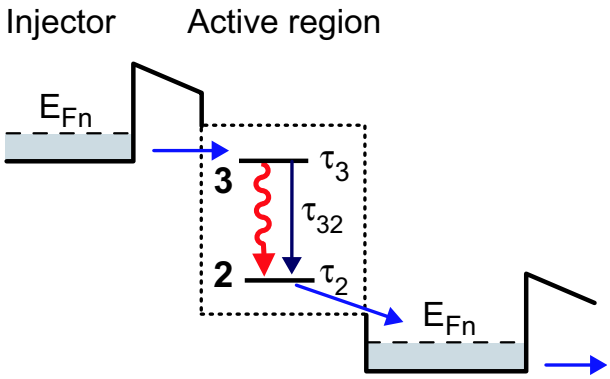

Figure 2.2: Schematic illustration of the states and lifetimes implied in the rate equation model.

The behavior below threshold is obtained by setting the derivatives and S to zero. From the first equation, we get a relation between the upper state population and the electrical pumping: $n_3 = J\tau_3/e$. Making use of the second, one obtains for the population inversion $\Delta n = n_3 - n_2$,

$$\Delta n = \frac{J\tau_3}{e}\Big(1 - \frac{\tau_2}{\tau_{32}}\Big) - n_2^{\mathrm{therm}} = \frac{J\tau_{\mathrm{eff}}}{e} - n_2^{\mathrm{therm}} \tag{2.22}$$

where the effective lifetime $\tau_{\mathrm{eff}} = \tau_3(1 - \tau_2/\tau_{32})$ relates the population inversion to the electrical pumping.

The threshold current density is reached when the modal gain $g_c\Delta n$ compensates for the losses α_{tot},

$$J_{\mathrm{th}} = e\,\frac{\alpha_{\mathrm{tot}}/g_c + n_2^{\mathrm{therm}}}{\tau_{\mathrm{eff}}} \tag{2.23}$$

Above threshold, the gain is clamped and S increases linearly. By again setting the time derivatives to zero and derivating by J, one can compute the slope efficiency

$$\frac{\mathrm{d}P}{\mathrm{d}I} = N_p h\nu \alpha_{m,1} \frac{\mathrm{d}S}{\mathrm{d}J} = \frac{N_p h\nu}{e} \frac{\alpha_{m,1}}{\alpha_{\mathrm{tot}}} \frac{\tau_{\mathrm{eff}}}{\tau_{\mathrm{eff}} + \tau_2} \tag{2.24}$$

2.2 Grating-coupled external cavity lasers

The most common grating-coupled external cavity configurations for semiconductor lasers are the Littrow and Littman-Metcalf[11] configurations illustrated in Fig. 2.3.

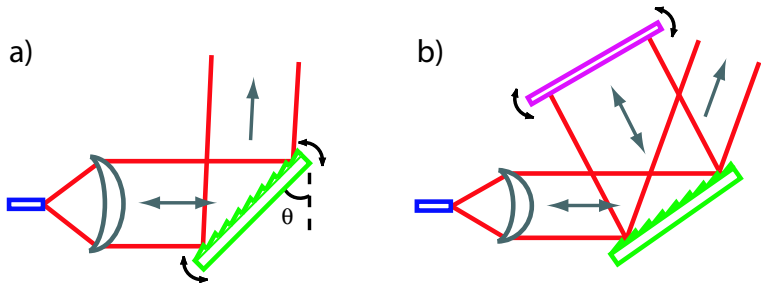

Figure 2.3: a) Littrow and b) Littman external cavity configurations. The large grey arrows indicate the directions of propagation of light and the small black arrows show how coarse tuning is achieved.

In the Littrow setup, the first-order diffracted beam from the grating is directly fed back into the chip. Coarse tuning is achieved by rotating the grating. This has the advantages of requiring only two optical elements, a lens and a diffraction grating, hence making the alignment easier, and providing a strong feedback since light is diffracted only once by the grating.

In the Littman setup, the first-order diffracted beam is sent back to the grating by an additional mirror to be diffracted again and the first-order beam of this second diffraction is sent back into the chip. Coarse tuning is usually achieved by rotating the mirror since it allows to keep unchanged the direction of the zeroth order, which can be used for extraction. The double-pass on the grating results in an increased wavelength selectivity, but it has the drawback of decreasing the feedback strength.

In order to maximize the tuning range, we selected the Littrow configuration. A sufficient selectivity for single-mode operation was obtained by using large gratings (4 cm).

2.2.1 Modeling of the Littrow configuration

When neglecting the reflectivity of the AR coated lens, the effect of the external part of the cavity can be taken into account by introducing a wavelength dependent amplitude reflection coefficient of the form (see Fig. 2.4.c for the meaning of the terms)

$$\begin{aligned} \tilde{r}_1(\theta_G, \lambda) &= r_1 + t_1^{(+)} e^{ikl} r_{\text{ext}} e^{ikl} t_1^{(-)} + t_1^{(+)} e^{ikl} r_{\text{ext}} e^{ikl} r_1 e^{ikl} r_{\text{ext}} e^{ikl} t_1^{(-)} + \dots \\ &= r_1 + r_{\text{ext}} \frac{t_1^{(+)} t_1^{(-)} e^{2ikl}}{1 - r_1 r_{\text{ext}} e^{2ikl}} \end{aligned} \tag{2.25}$$

where θ_G is the grating angle, r_1 the amplitude reflection coefficient of the facet, $t_1^{(+)}$ and $t_1^{(-)}$ its forward and backward amplitude transmission coefficients (satisfying $t_1^{(+)} t_1^{(-)} = T_1 =$ intensity reflection coefficient), $k = 2\pi/\lambda$, l is the distance from the facet to the grating, and $r_{\text{ext}}(\theta_G, \lambda)$ describes the reflection of the external part of the cavity. Since we are interested in the case $r_1 \ll 1$, we keep only the first term

$$\tilde{r}_1(\theta_G, \lambda) \cong r_1 + T_1 \, r_{\text{ext}}(\theta_G, \lambda) \, e^{2ikl} \tag{2.26}$$

The external reflection coefficient can be written as $r_{\text{ext}}(\theta_G, \lambda) = T_L \sqrt{R_G} \, \eta$ where T_L is the transmission of the lens, R_G the first-order efficiency of the grating, and $\eta(\theta_G, \lambda)$ the coupling of the reflected wave to the initial waveguide mode. The latter is given by the overlap integral between the normalized amplitude profiles of these two beams on the coupling facet:

$$\eta = \int \mathrm{d}x \, \mathrm{d}y \, u_i^*(x, y) u_r(x, y) \tag{2.27}$$

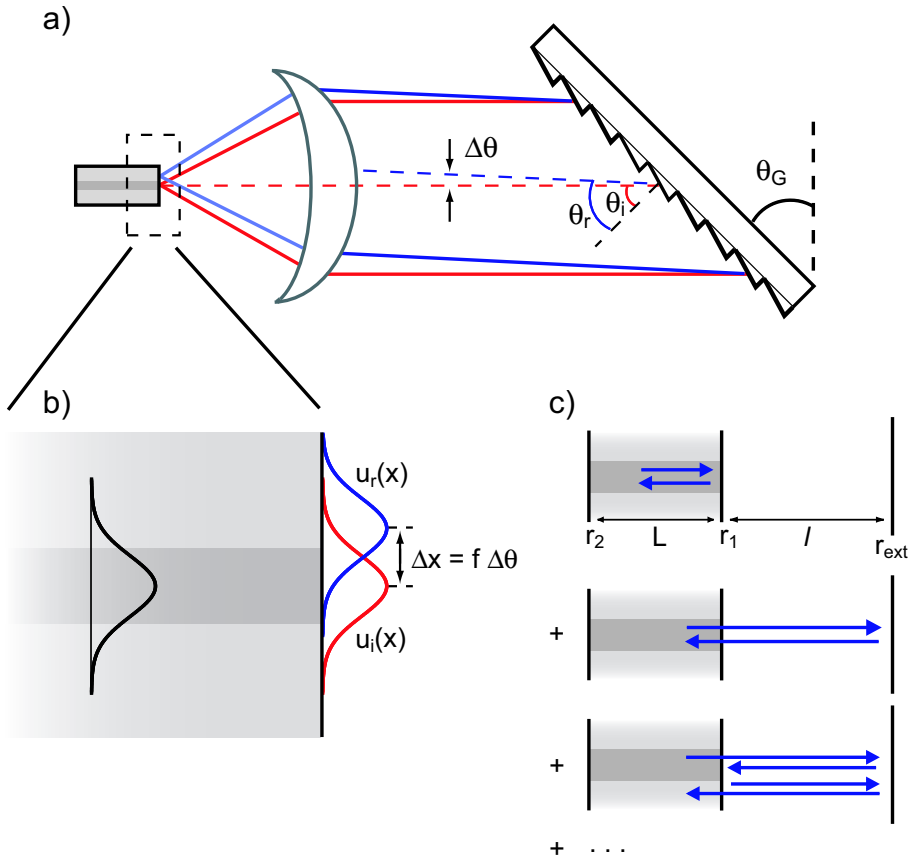

Figure 2.4: a) Schematic drawing of the Littrow configuration. The incident beam (in red) is diffracted by the grating at an angle $\Delta\theta$ depending on the wavelength λ. b) The angle $\Delta\theta$ introduces a shift of the reflected beam by a distance $\Delta x = f\Delta\theta$. c) Schematic representation of all the terms for the calculation of $\tilde{r}_1(\theta_G, \lambda)$.

We model the emitted beam by an elliptical gaussian beam[12] whose waist is located on the facet ($z = 0$). The intensity varies in space as

$$I(\mathbf{x}) = \frac{2P}{\pi W_x(z) W_y(z)} \exp\Big[-2\Big(\frac{x^2}{W_x^2(z)} + \frac{y^2}{W_y^2(z)}\Big)\Big] \tag{2.28}$$

where P is the total optical power carried by the beam, $W_i(z) = W_{0i}\sqrt{1 + (\frac{z}{z_{0i}})^2}$ its half-width in direction i, and $z_{0i} = \pi W_{0i}^2/\lambda$ its Rayleigh length in this direction. The parameters W_{0i} can be determined by measuring the far field profile. For $z \gg z_{0i}$, we have $W_i(z) \rightarrow$

$W_{0i}\frac{z}{z_{0i}} = \frac{\lambda}{\pi W_{0i}}z$. Setting $\tan\theta_x = \frac{x}{z}$ et $\tan\theta_y = \frac{y}{z}$, the angular intensity takes the form

$$I(\theta_x, \theta_y) \propto \exp\Big[- \frac{2\pi^2}{\lambda^2}\Big(W_{0x}^2 \tan\theta_x^2 + W_{0y}^2 \tan\theta_y^2\Big)\Big] \tag{2.29}$$

The parameters W_{0i} are hence inversely proportional to the half widths at half maximum $\theta_{\frac{1}{2},i}$ of the far field profile: $\tan\theta_{\frac{1}{2},i} \cong 0.187\frac{\lambda}{W_{0i}}$

We assume that the beam is colimated by the lens, then diffracted by the grating in a direction making an angle $\Delta\theta(\lambda, \theta_R)$ with the direction of incidence, and finally focalized on the facet at a distance $\Delta x = f\Delta\theta$ from the starting point, while remaining gaussian (see Fig. 2.4.a and b).

The directions of the various orders of diffraction of the grating $\theta_{r,m}$ with respect to the normal are given by

$$\sin\theta_i + \sin\theta_{r,m} = m\frac{\lambda}{d} \tag{2.30}$$

where θ_i is the angle of incidence, d is the period of the grating, and $m = 0,\ \pm1,\ \pm2, \ldots$. We used the first order diffracted beam ($m = 1$). The angle of incidence is equal to θ_G, the angle between the grating and the normal to the beam (see Fig. 2.4.a). The feedback is maximum when the incident and diffracted beams are colinear. This defines the grating selected wavelength $\lambda_G = 2d\sin\theta_G$. For others wavelength, we write $\theta_{r,1} = \theta_G + \Delta\theta$, where $\Delta\theta$ is the angle between the incident and reflected beams, and linearize the grating equation in the vicinity of λ_G:

$$\Delta\theta = \frac{\lambda - \lambda_G}{d\cos\theta_G} \tag{2.31}$$

The normalized amplitude profile of the beam on the facet reads

$$U(x, y) = \Big(\frac{2}{\pi W_{0x} W_{0y}}\Big)^{\frac{1}{2}} \exp\Big[- \Big(\frac{x^2}{W_{0x}^2} + \frac{y^2}{W_{0y}^2}\Big)\Big] \tag{2.32}$$

Inserting in Equ. 2.27, one gets

$$\eta = \int \mathrm{d}x\,\mathrm{d}y\,U(x,y)U(x-\Delta x,y) = \exp\Big(-\frac{\Delta x^2}{2W_{0x}^2}\Big) \tag{2.33}$$

Making use of expression 2.31 for the diffraction angle, one finally finds

$$r_{\mathrm{ext}}(\theta_G,\lambda) = T_L\sqrt{R_G}\exp\Big[-\frac{f^2(\lambda-\lambda_G)^2}{2W_{0x}^2 d^2\cos^2\theta_G}\Big] \tag{2.34}$$

Let's notice that this expression has been derived for an ideal (diffraction limited) lens. In the case of an imperfect lens, the size of the reflected beam on the facet is larger and consequently r_{ext} has a broader and less intense peak at λ_G.

The allowed modes of the external cavity and the corresponding threshold gains are determined by the stationary condition

$$\tilde{r}_1(\theta_G,\lambda)r_2\,e^{2inkL}e^{(G_M-\alpha_w)L} = 1 \tag{2.35}$$

(the wave should have the same amplitude and phase after one round-trip in the cavity), where n is the refractive index of the chip and L its length. The condition on the amplitude readily gives the threshold modal gain as a function of wavelength:

$$G_{M,th}(\lambda) = \alpha_{\mathrm{tot}}(\lambda) = \alpha_w + \frac{1}{L}\ln\frac{1}{|\tilde{r}_1(\theta_G,\lambda)\,r_2|} \tag{2.36}$$

and the condition on the phase gives the allowed modes:

$$\arg\Big[\tilde{r}_1(\theta_G,\lambda)\Big] + \frac{4\pi nL}{\lambda} = N\cdot 2\pi \tag{2.37}$$

For wavelengths far from λ_G, the first term in $\tilde{r}_1(\theta_G,\lambda)$ dominates and the usual results for a Fabry-Pérot chip are recovered. The modes are spaced by $\Delta\nu_{FP} = \frac{c}{2nL}$ and the threshold gain equals

$$G_{M,th}^{FP}(\lambda) = \alpha_{FP} = \alpha_w + \frac{1}{2L}\ln\frac{1}{R_1R_2} \tag{2.38}$$

On the contrary, for wavelengths close to λ_G the second term dominates. In this case, $\arg(\tilde{r_1}) \cong 2ikl$, resulting in a mode spacing equal to $\Delta\nu_{EC} = \frac{c}{2(nL+l)}$. The minimum threshold gain is

$$G^{EC}_{M,th}(\lambda_G) = \alpha_{EC} = \alpha_w + \frac{1}{2L}\ln\frac{1}{R_{EC}R_2} \tag{2.39}$$

with $R_{EC} = \left(r_1 + T_1 T_L \sqrt{R_G}\right)^2$.

2.3 Tuning properties

2.3.1 Coarse tuning range

The coarse tuning range of the external cavity laser can readily be obtained by comparing the threshold current density of the grating selected mode with that of the Fabry-Pérot modes of the chip:

$$J^{FP}_{\text{th}} = \frac{\alpha_{FP}}{g_{\max}}, \qquad J^{EC}_{\text{th}}(\lambda) = \frac{\alpha_{EC}}{g(\lambda)} \tag{2.40}$$

where α_{FP} and α_{EC} are defined in Equ. 2.38 and 2.39 and $g_{\max}$ is the maximum of the differential gain $g(\lambda)$. Tuning is possible on the range where $J^{EC}_{\text{th}}(\lambda) \leq J^{FP}_{\text{th}}$, that is where

$$\frac{g(\lambda)}{g_{\max}} \geq \frac{\alpha_{EC}}{\alpha_{FP}} = \xi \tag{2.41}$$

2.3.2 Fine tuning behavior

In order to investigate the fine tuning behavior we solved numerically Equation 2.35 to determine the external cavity modes. The lasing mode is the mode with the lowest losses. The results of this computation for the case in which only the grating angle is varied is shown in Fig. 2.5. The simulation is done for a 3 mm-long HR coated chip with waveguide losses of 10 cm^{-1} in our external cavity setup. The lasing frequency as a function of the grating angle is plotted for two values of the front facet reflectivity, 2% and 0.2%. In the first case, the tuning happens only on the external cavity modes that are close to the Fabry-Pérot

modes of the chip. In the second case, on the contrary, tuning between the chip FP modes is possible and mode hops occur only on the EC modes. These mode hops can be suppressed by varying the EC length together with the grating angle.

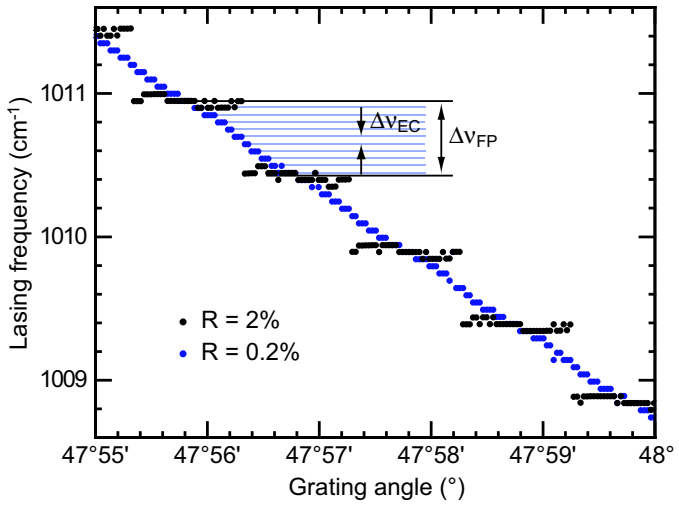

Figure 2.5: Fine tuning behavior of an external cavity QCL for two different values of the front facet reflectivity. With $R_1 = 2\%$ tuning is possible only on EC modes that are very close to the FP modes of the chip. With $R_1 = 0.2\%$ tuning is possible on all the EC modes.

Figure 2.6 shows the computed losses and allowed modes of the external cavity in the two cases for one given grating angle. The angle is chosen so that the grating selected wavelength λ_G is roughly midway between two chip FP modes. In this case the waves reflected by the grating and the facet interfere destructively. For $R_1 = 2\%$, the amplitude of these partial waves are of the same order of magnitude so that the modes near λ_G have a larger threshold than the modes near the next FP mode, for which r_{ext} is smaller but the partial waves are in phase. For $R_1 = 0.2\%$, the contribution from the grating dominates and consequently the modes which are the closest to λ_G have the lowest threshold despite the destructive interferences.

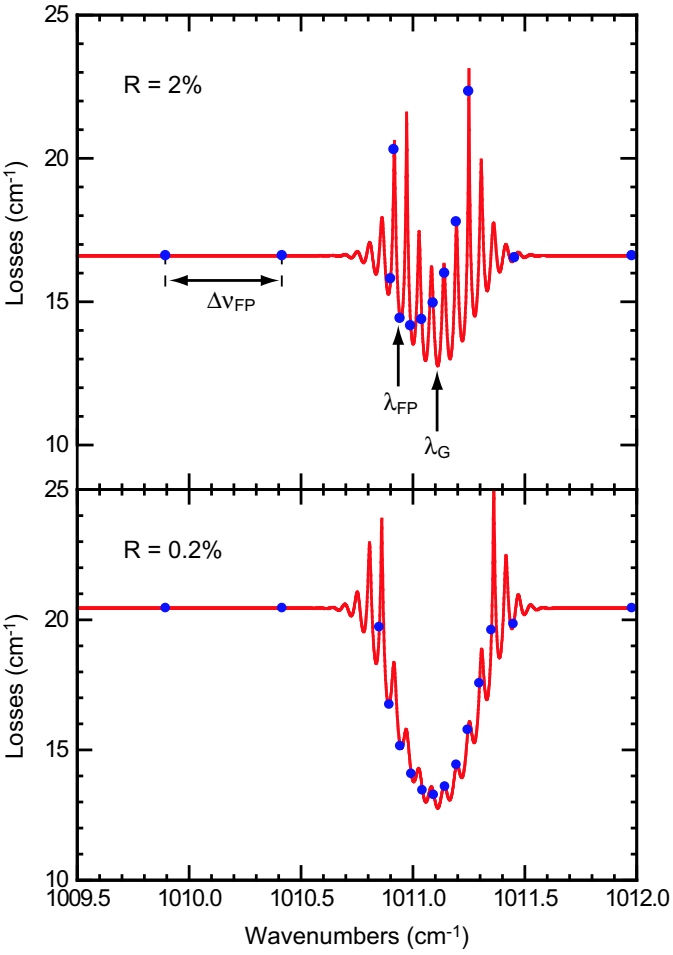

Figure 2.6: External cavity losses as a function of the wavenumber for a given grating angle and two different values of the front facet reflectivity. The blue disks mark the allowed modes. The angle is chosen so that the reflections from the facet and the grating interfere destructively.

2.4 Anti-reflection coating

The anti-reflection (AR) coating of the gain chip is a key element of an external cavity laser. We have seen in the last section that a low reflectivity allows a larger tuning range and mode-hop free fine tuning. It also allows single-mode operation even in pulsed mode by suppressing the mode competition occuring at the begining of the pulses described in chapter 4. In this section I will present the model that we used to compute the reflectivity of multilayer coatings.

We neglected the waveguide structure and computed the Fresnel reflectivity for a plane wave propagating in a semi-infinite medium of refractive index n_s, with n_s equal to the effective refractive index of the mode under consideration. We considered isotropic, linear, and nonmagnetic media without macroscopic charges ($\rho = 0$, $\mathbf{J} = 0$). Mawell's equations read

$$\begin{aligned} \nabla \cdot \mathbf{E} = 0 \qquad & \nabla \times \mathbf{E} + \frac{\partial \mathbf{B}}{\partial t} = 0 \\ \nabla \cdot \mathbf{B} = 0 \qquad & \nabla \times \mathbf{B} - \frac{n^2}{c^2}\frac{\partial \mathbf{E}}{\partial t} = 0 \end{aligned} \tag{2.42}$$

We consider monochromatic plane wave solutions propagating along the z axis and polarized along the x axis. In medium 0, the only non zero components of the electric and magnetic fields, E_x and B_y take the form:

$$E_0(\mathbf{x}, t) = \left[E_{f,0}e^{ik_0 z} + E_{b,0}e^{-ik_0 z}\right]e^{-i\omega t} \tag{2.43}$$

$$B_0(\mathbf{x}, t) = \left[\frac{n_0 E_{f,0}}{c}e^{ik_0 z} - \frac{n_0 E_{b,0}}{c}e^{-ik_0 z}\right]e^{-i\omega t} \tag{2.44}$$

where $k_0 = n_0\omega/c$. The absorption in the layers was taken into account via the imaginary part of the refractive index $n = n_R + in_I$ where n_I is related to the usual absorption coefficient α (in cm^{-1}) by the relation $\alpha = \frac{4\pi n_I}{\lambda}$. Of course similar expressions are found for the fields in medium 1. When imposing the continuity of E and B at the interface z_1, one finds

$$\begin{pmatrix} E_{f,0} \\ E_{b,0} \end{pmatrix} = P_{01}\begin{pmatrix} E_{f,1} \\ E_{b,1} \end{pmatrix} = \frac{1}{\tau_{01}}\begin{pmatrix} 1 & \rho_{01} \\ \rho_{01} & 1 \end{pmatrix}\begin{pmatrix} E_{f,1} \\ E_{b,1} \end{pmatrix} \tag{2.45}$$

where $\tau_{01} = \frac{2n_0}{n_0+n_1}$ and $\rho_{01} = \frac{n_0-n_1}{n_0+n_1}$. P_{01} is called interface coupling matrix, or passage matrix. The dephasing experienced by the waves between interfaces i and $i+1$ is described by a dephasing matrix D_i:

$$\begin{pmatrix} E_{f,i} \\ E_{b,i} \end{pmatrix} = D_i\begin{pmatrix} E'_{f,i} \\ E'_{b,i} \end{pmatrix} = \begin{pmatrix} e^{-ik_i d_i} & 0 \\ 0 & e^{ik_i d_i} \end{pmatrix}\begin{pmatrix} E'_{f,i} \\ E'_{b,i} \end{pmatrix} \tag{2.46}$$

where $E_{f,i}$ and $E_{b,i}$ are the electric fields of the forward and backward propagating waves at z_i, and $E'_{f,i}$ and $E'_{b,i}$ the electric fields of the same waves at z_{i+1} (see Fig. 2.7).

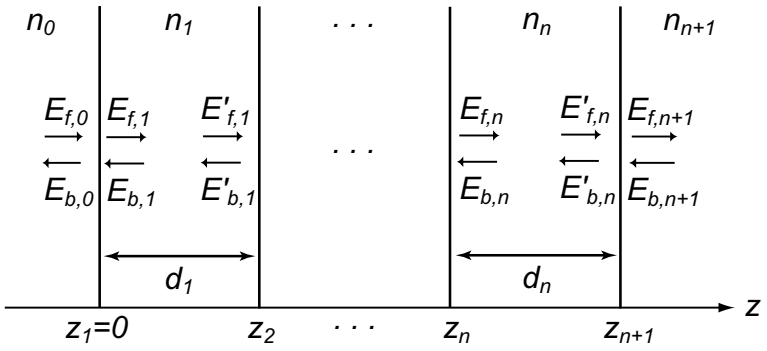

Figure 2.7: Model used for computing the reflectivity of the AR coating structures.

The interface coupling and dephasing matrices allow to propagate the boundary conditions across the structure. The complete structure is described by a transfer matrix S such as

$$\begin{pmatrix} E_{f,0} \\ E_{b,0} \end{pmatrix} = S \begin{pmatrix} E_{f,n+1} \\ E_{b,n+1} \end{pmatrix} \tag{2.47}$$

$$S = P_{01} D_1 P_{12} D_2 \ldots \ \ldots D_n P_{n,n+1} \tag{2.48}$$

To compute the intensity reflection and transmission coefficients (also called reflectance and transmitance) for a wave coming from the left, we set $E_{f,0} = E_i$, $E_{b,0} = E_r$, $E_{f,n+1} = E_t$, and $E_{f,n+1} = 0$. Recalling that the energy carried by a wave is given by its Poynting vector

$$\mathbf{S}(\mathbf{x}) = \frac{1}{2\mu_0} \mathrm{Re}\big[\mathbf{E}(\mathbf{x}) \times \mathbf{B}^*(\mathbf{x})\big] \tag{2.49}$$

which is proportional to $\mathrm{Re}(n)|E|^2$, one finally finds finds

$$R = \frac{|E_r|^2}{|E_i|^2} = \frac{|S_{21}|^2}{|S_{11}|^2} \tag{2.50}$$

$$T = \frac{\mathrm{Re}(n_{n+1})|E_t|^2}{\mathrm{Re}(n_0)|E_i|^2} = \frac{\mathrm{Re}(n_{n+1})}{\mathrm{Re}(n_0)|S_{11}|^2} \tag{2.51}$$

$$\tag{2.52}$$

The case of a single layer coating can be treated analytically. The reflectivity reads

$$R(\lambda) = \frac{R_{01} + R_{12} + 2\rho_{01}\rho_{12}\cos 2k_1 d_1}{1 + R_{01}R_{12} + 2\rho_{01}\rho_{12}\cos 2k_1 d_1} \tag{2.53}$$

with $R_{ij} = |\rho_{ij}|^2$. For $n_0 > n_1 > n_2$, $R(\lambda)$ reaches its minimum when $n_1 d_1 = \frac{\lambda}{4}$ (or any other odd multiple of $\frac{\lambda}{4}$) because the backward waves reflected by the two interfaces have a π phase difference and thus interfere destructively. This is called a quarter-wave layer. One can show that the reflectivity of such a layer is given by $\left(\frac{n_0 n_2 - n_1^2}{n_0 n_2 + n_1^2}\right)^2$ and hence cancels when $n_1 = \sqrt{n_0 n_2}$. In our case this requires a refractive index of $\sqrt{3.2} \cong 1.8$ for the coating material.

For the optimization of multi-layer AR coatings, we used a numerical program to track the minimum reflectivity. The wavelength-dependent refractive indices $n_i(\lambda)$ were computed by interpolating the data from Ref.[13].

Bibliography

[1] G. Bastard, "Wave mechanics applied to semiconductor heterostructures", (Les éditions de physique, Paris, 1990).

[2] D. F. Nelson, R. C. Miller, and D. A. Kleinman, "Band nonparabolicity effects in semiconductor quantum wells", Phys. Rev. B **35**, 7770 (1987).

[3] J. Faist, F. Capasso, C. Sirtori, D. L. Sivco, and A. Y. Cho, "Quantum cascade lasers", in *Intersubband Transitions in Quantum Wells: Physics and Device Applications II*, Edited by H. C. Liu and F. Capasso (Academic, San Diego, 2000), pp. 1-83.

[4] G. Bastard, "Superlattice band structure in the envelope-function approximation", Phys. Rev. B **24**, 5693 (1981).

[5] C. Sirtori, F. Capasso, J. Faist, and S. Scandolo, "Nonparabolicity and a sum rule associated with bound-to-bound and bound-to-continuum intersubband transitions in quantum wells", Phys. Rev. B **50**, 8663 (1994).

[6] R. Ferreira and G. Bastard, "Evaluation of some scattering times for electrons in unbiased and biased single- and multiple-quantum-well structures", Phys. Rev. B **40**, 1074 (1989).

[7] T. Unuma, T. Takahashi, T. Noda, M. Yoshita, H. Sakaki, M. Baba, and H. Akiyama, "Effects of interface roughness and phonon scattering on intersubband absorption linewidth in a GaAs quantum well", Appl. Phys. Lett. **78**, 3448 (2001).

[8] T. Unuma, M. Yoshita, T. Noda, H. Sakaki, and H. Akiyama , "Intersubband absorption linewidth in GaAs quantum wells due to scattering by interface roughness, phonons, alloy disorder, and impurities", J. Appl. Phys. **93**, 1586 (2003).

[9] T. Ando, A. B. Fowler, and F. Stern, "Electronic properties of two-dimensional systems", Rev. Mod. Phys. **54**, 437 (1982).

[10] S. Tsujino, A. Borak, E. Müller, M. Scheinert, C. V. Falub, H. Sigg, D. Grützmacher, M. Giovannini, and J. Faist, "Interface-roughness-induced broadening of intersubband electroluminescence in p-SiGe and n-GaInAs/AlInAs quantum-cascade structures", Appl. Phys. Lett. **86**, 062113 (2005).

[11] M. G. Littman and H. J. Metcalf, "Spectrally narrow pulsed dye laser without beam expander (ET)", Appl. Opt. **17**, 2224 (1978).

[12] B. E. A. Saleh, M. C. Teich, "Fundamentals of photonics", (Wiley, New York, 1991).

[13] E. D. Palik, "Handbook of optical constants of solids", Vol. I, II, (Academic Press Inc, 1985).

Chapter 3

Device fabrication and characterization

3.1 Epitaxial growth

The quantum cascade lasers studied during this thesis were grown in two steps using two different epitaxy techniques. The highly demanding active region, typically composed of 500-1000 layers with thicknesses between a few angstroms and a few nanometers, was grown by molecular beam epitaxy (MBE)[1], and the much simpler cladding structure, typically composed of 3-4 layers with thicknesses between 50 nm and a few microns, was subsequently grown by metalorganic vapor phase epitaxy (MOVPE, also called metalorganic chemical vapor deposition, MOCVD).

The MBE growth of the samples was carried out by Dr. Mattias Beck, Dr. Marcella Giovannini, and Nicolas Hoyler from University of Neuchâtel using the in-house facility, a V80H from VG Semicon (now Oxford Instruments) dedicated to the growth of InGaAs/InAlAs structures on InP substrates and GaAs/AlGaAs structures on GaAs substrates. The 22 to 35 active region periods, composed of 10 to 12 QWs each, were grown on 2-inches-diameter, n-doped (1-2$\times 10^{17}$ cm^{-3}), InP substrates between two InGaAs spacers designed to enhance the overlap of the optical mode with the active region. The bottom spacer, usually 200 nm

thick, has also the function of a buffer layer preventing from starting the growth of the active region directly on the substrate.

The MOVPE overgrowth was realized under the supervision of Dr. Emilio Gini at the FIRST Center for Micro- and Nanoscience of the Swiss Federal Institute of Technology (ETH), Zurich, Switzerland on some of the epilayers, and by IPAG Innovative Processing AG (now AL Technologies GmbH), Darmstadt, Germany on the others.

3.2 Sample processing

After the epitaxial growth, the samples were processed in ridge waveguides. The basic fabrication steps, illustrated in fig. 3.1, are a) patterning of the stripes, b) wet chemical etching of the ridges, c) deposition of an insulating layer, d) patterning of the insulator opening, e) opening of the insulating layer on top of the ridges for electrical contacting, f) deposition of a metallic top contact, g) thinning of the wafer, h) deposition of a bottom contact, and i) electroplating of a thick gold layer for heat dissipation.

Since the laser ridges are typically 8 to 30 μm wide, the pattern transfers are easily done with standard photolithography. As etchant we used a $HBr:HNO_3:H_2O$ (1:1:10) solution which has the advantages of being isotrope, non selective between InP and InGaAs/InAlAs, and diffusion limited. As insulator we used 300 nm of Si_3N_4 deposited by plasma enhanced chemical vapor deposition (PECVD). The top opening was realized by reactive ion etching (RIE) under $CHF_3/Ar/O_2$ atmosphere. The top contact was deposited by e-beam evaporation in two steps: first we deposited an alloyed Ge/Au/Ag/Au (12/27/50/100 nm) contact only on top of the ridges using the resist of the opening for liftoff, and then an extended Ti/Au (10/200 nm) contact covering the previous one plus the sides of the ridges. The first one is a low resistance ohmic contact and the second one demonstrates excellent adhesion because of the titanium layer. The 500 μm-thick substrate was then thinned down to $\sim$150 μm by mechanical polishing in order to reduce its thermal resistance and make the cleaving easier. Finally, a Ge/Au/Ag/Au (12/27/50/500 nm) alloyed contact was deposited on the

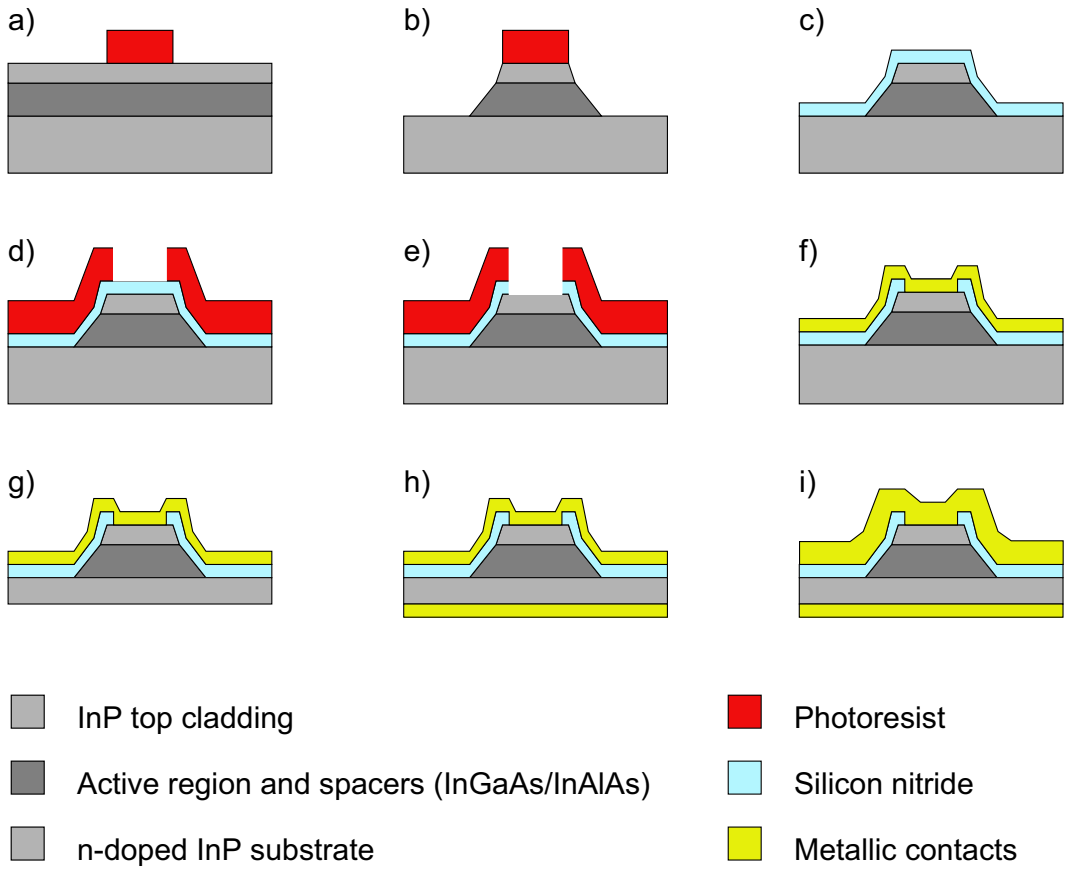

Figure 3.1: Process flow for the fabrication of ridge waveguide QCLs.

bottom side by e-beam evaporation and a thick gold layer of typically 5 μm was electroplated on the top contact.

The samples were then cleaved in laser bars, soldered to a copper plate using indium and wire bonded.

A high-reflection (HR) coating was often deposited on the back facet of the chips. Its functions are to reduce the threshold current density, hence allowing higher temperature operation, and to increase the output power. We used an Al_2O_3/Au (300 nm/100 nm) metallic coating, whose reflectivity is $\approx 95\%$, deposited by e-beam evaporation.

When a measurement of the spontaneous emission spectrum (electroluminescence in absence of optical feedback) of an epilayer was needed, we processed the sample in square mesas of typically 100 μm squared. Since these dimensions allow wire bonding directly on

top of the mesa, we didn't use any insulating layer and deposited the top contact only on top of the structures. The samples were polished with a 45° tilt in order to enhance light extraction out of the substrate.

3.3 Electrical and optical characterization

The QC chips were tested in a commercial thermoelectrically-cooled laboratory laser housing from Alpes Lasers. The original thermoelectric cooler was replaced by a more powerful one (Melcor Corporation, Trenton, NJ, USA, model UT8) able to maintain the heatsink temperature at -30°C when testing CW devices which generate up to $\approx$ 10 W of heat to dissipate. The temperature controler had to be modified as well to provide the 8 A (with a compliance of 14 V) needed by this TE cooler. The current pulses, typically 100 ns long, were generated by a LDD 100 laser diode driver also from Alpes Laser driven by an Agilent 33250 waveform generator. The output power was measured with a calibrated thermopile detector (Ophir Optronics Ltd., Jerusalem, Israel).
The electroluminescent samples where tested in liquid nitrogen cooled flow cryostat.

The optical characterization relied on Fourier transform infrared (FTIR) spectroscopy. We generally used a Nicolet 860 FTIR spectrometer with two internal detectors, a room temperature deuterated triglycine sulphate (DTGS) one and a liquid-nitrogen-cooled mercury cadmium telluride (MCT) one, plus an output port allowing the use of an external detector. When needed, we used a fast room temperature MCT external detector together with a gated integrator to acquire time-resolved spectra of the laser on a nanosecond scale, as described in Sect. 4.5.
For the measurement of electroluminesence spectra, a more sensitive LN_2 cooled MCT detector was used and the FTIR was operated in step scan mode. The sample was driven in pulsed mode and the signal was detected using a lock-in amplifier (EG&G Instruments, model 7265).

3.4 Anti-reflection coatings

As discussed in the previous chapter, the more straightforward way to make an anti-reflection coating on the facet of a QC laser is to deposit a quarter-wave layer of a material with a refractive index equal to $n_c = \sqrt{n_s} \cong 1.8$, where $n_s \cong 3.2$ is the refractive index of the chip. The whole problem is to find such a material with a good adhesion to the facet and a low absorption at the desired wavelength.

In our first paper, describing an EC-QCL emitting near 10 μm (see Chapter 4), we used a zinc sulphide quarter-wave layer. ZnS is transparent up to 13 μm, but it has a index of 2.2, quite far from the ideal one, which gives a residual reflectivity of 4%. Furthermore, we observed that these coatings tended to flake after several hours of use of the chips.

Later, for the realization of our CW EC-QCL near 5.2 μm, (see Chapter 5) we used aluminium oxide Al_2O_3 (also called alumina, or sapphire when it is in its single-crystal form), which has a refracive index of 1.6 in this region, corresponding to a reflectivity of 1%. We knew in advance that its adhesion to the facet is excellent because we use it as insulating layer for HR coatings. This material allowed us to reach reflectivites of the order of 1-3% in this region, but it cannot be used for longer wavelengths because it starts to absorb at 6 μm. In addition, it doesn't allow to reach the reflectivity needed for mode-hop free tuning ($R < 0.7\%$).

Yttrium oxide Y_2O_3 seemed to be a good candidate too, because its refractive index varies between 1.85 at 4 μm and 1.7 at 8.5 μm according to Ref. [2], resulting in $R < 0.3\%$ for a quarter wave-layer, and its absorption is low up to ≈ 9 μm. Unfortunately, we couldn't deposit a uniform film of this material on chip facets. Our trials with e-beam evaporation always resulted in a cracked surface.

Zero reflectivity can also be achieved using two-layer coatings in which one of the materials has a refractive index higher than $\sqrt{n_s}$ and the other one lower. We recently developed such a two-layer structure based on YF_3 and ZnSe which allows to realize low residual reflectivity AR coatings over the 3 to 12 μm wavelength range.

λ (μm)	$\tilde{\nu}$ (cm^{-1})	n_{YF_3}
5	2000	1.5
8	1250	1.37
10	1000	1.3

Table 3.1: Data from Ref. [3] used to evaluate the yttrium fluoride refractive index $n_{YF_3}(\tilde{\nu})$. The datapoints were fitted with a second order polynomial function.

Zinc selenide is a widespread material for infrared optics. It is transparent over the entire NIR and MIR regions, and has a quasi constant refractive index $n_{ZnSe} = 2.4$ between 2.5 and 16 μm. Yttrium fluoride has a lower refractive index varying between 1.5 at 5 μm and 1.3 at 10 μm[3] and a transparency region covering the NIR and the two atmospheric windows in the the MIR, up to $\approx$ 12 μm[4]. We computed its refractive index as a function of the wavenumber $\tilde{\nu} = \nu/c$ in cm^{-1} by interpolating the data from Ref. [3] listed in Table 3.1 with a second order polynomial function. We observed that YF_3 has an excellent adhesion to the facet, contrary to ZnSe, and ZnSe sticks very well on YF_3. So we designed coatings whose first layer is YF_3 and second layer is ZnSe.

According to our simuations, zero reflectivity coatings can be designed at any given wavelength within the transparency range of the materials. The computed layer thicknesses to deposit are plotted as functions of the wavenumber on top graph of Fig. 3.2. Because the materials are not deposited in order of decreasing refractive index, the bandwidth of the coating, defined as the range over which $R < 1\%$, is 10-15% smaller than that of a quarter wave layer (see bottom graph of Fig. 3.2). The reversed combination would give a larger bandwidth, but it does not stick to the facet.

We deposited the materials with a thermal evaporator. The thicknesses were monitored with a quartz crystal balance. The balance was first calibrated by deposing $\sim$ 900 nm of each material on partly masked pieces of InP substrate and measuring the actual thicknesses with a surface profilometer. The coating was then deposited on pieces of semi-insulating InP substrate with two optical quality surfaces and its transmission was measured with a FTIR

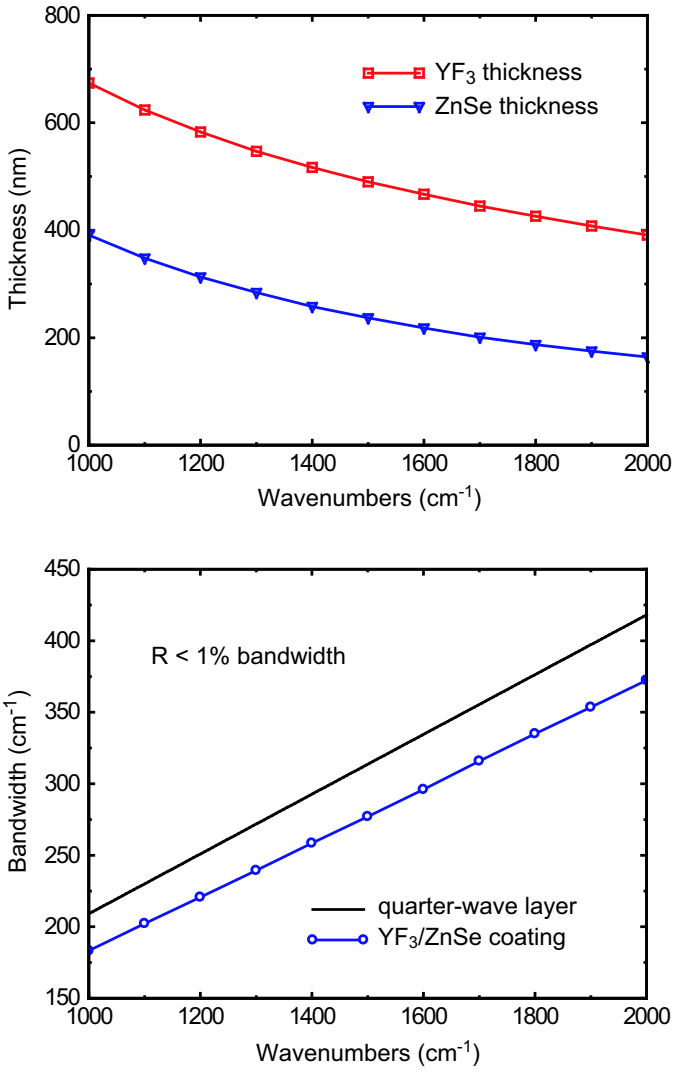

Figure 3.2: Top graph: Yttrium fluoride and zinc selenide layer thicknesses to deposit to obtain a zero reflectivity coating for various wavenumbers between 5 and 10 μm. Bottom graph: Bandwidths of the YF_3/ZnSe coating and a quarter-wave layer coating.

spectrometer. The resulting spectra were in good agreement with the theoretical predictions.

We could obtain reflectivities of 0.6-0.8% at 5.2 and 9 μm with this coating on ridge-waveguide devices. We later understood that we couldn't reach lower reflectivity with such devices because the thicknesses that we deposited were systematically thinner than expected. This is due to border effects related to the small surface of the facet ($\sim 5{\times}10\ \mu m^2$) and the

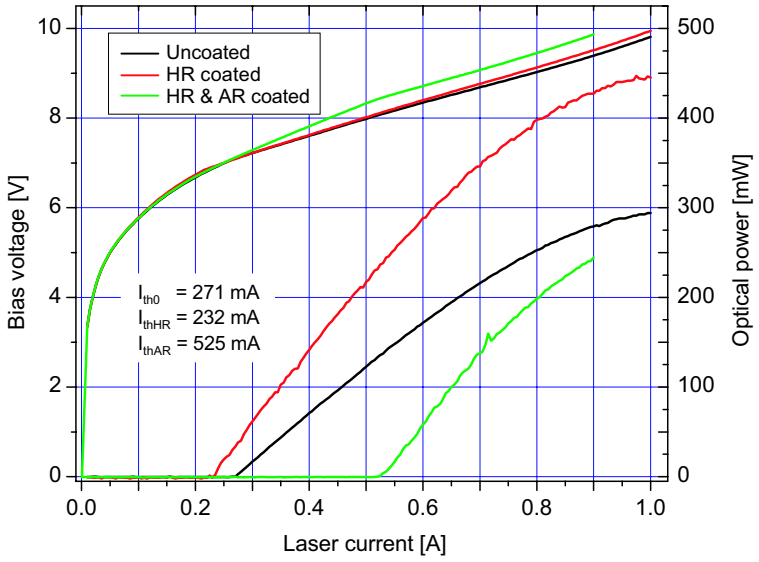

Figure 3.3: Optical power versus current characteristics at $T = -30°\text{C}$ of a buried heterostructure device with uncoated facets (black curve), HR coated back facet and uncoated front facet (red curve), and HR coated back facet and AR coated front facet (green curve).

large thickness that has to be deposited (~ 1 μm). This interpretation was confirmed by a red shift of the Fabry-Pérot spectra of the lasers after coating caused by a larger reflectivity on the long-wavelength side (see Chap. 6).

Better results were obtained on buried heterostructure devices, in which the active region is surrounded by InP material, creating a larger surface to deposit the coating. Figure 3.3 shows the results obtained with a 3 mm long device emitting at $\lambda \sim 8.4$ μm, fabricated by the Agilent Labs group, that we coated for Dr. Gerard Wysocki. The threshold current increased by a factor $\rho = 2.3$ after coating. Taking into account the waveguide losses $\alpha_w = 8$ cm^{-1} measured by Diehl et al. for those devices[5], one finds

$$R_{AR} = R_0^{\rho}\, e^{2L(\rho-1)\alpha_w} \cong 10^{-4} \tag{3.1}$$

This very low reflectivity was definitely a stroke of luck, because it requires a precision of ± 10 nm on the thickness of the first layer and ± 5 nm on the thickness of the second one (see Figure 3.4) which are beyond what is feasible with our apparatus. Nevertheless it

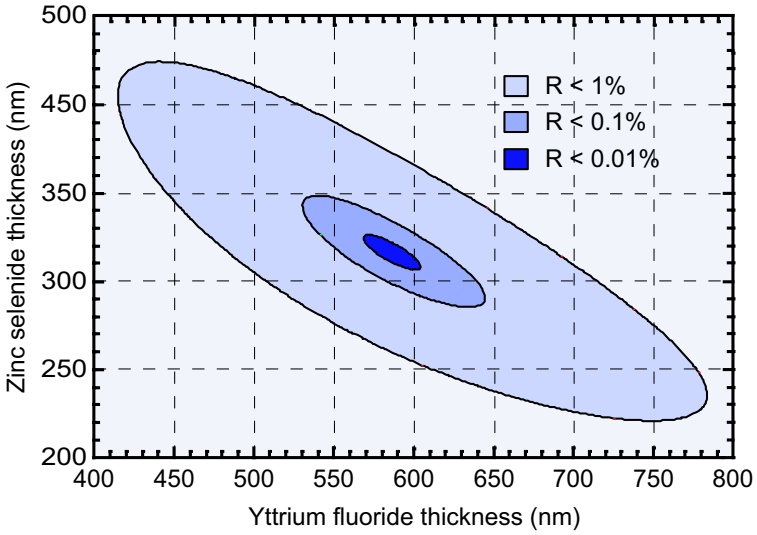

Figure 3.4: Reflectivity of the YF_3/ZnSe AR coating as a function of the thicknesses of the two layers. A reflectivity smaller than 0.1% requires a precision of ± 30 nm on the thickness of the first layer and ± 15 nm on the thickness of the second one.

demonstrates that such reflectivities are achievable with this pair of materials. We routinely achieved reflectivities below 0.5% at wavelength between ≈ 5 and 9 μm using this coating.

In order to reach routinely reflectivities of the order of 10^{-3} or smaller, one would need to estimate the facet reflectivity in situ during the deposition. This can be done by measuring the threshold current of the laser, which is a function of the mirror losses. A simple way to implement this is to acquire the electrical characteristic (bias versus current) of the chip and locate the differential resistance discontinuity. This feature is a clear signature of the threshold and can be determined by an all-electrical measurement. With the present generation of QCLs, which lase CW above room temperature, the implementation is even easier because it does not require a high frequency elecrical feedthrough in the vacuum chamber.

Bibliography

[1] A. Cho, "Molecular beam epitaxy", (AIP Press, Woodbury, NW, 1994).

[2] E. D. Palik, "Handbook of optical constants of solids", Vol. I, II, (Academic Press Inc, 1985).

[3] D. Benzuidenhout, R. Clarke, and R. Pretorius, "The optical properties of YF_3 films", Thin Solid Films **155**, 17 (1987).

[4] M. A. Gisin, R. M. Mustaev, "Optical properties of yttrium fluoride films in the IR region", J. Opt. Technol. **63**, 831 (1996).

[5] L. Diehl, D. Bour, S. Corzine, J. Zhu, G. Höfler, M. Lončar, M. Troccoli, and F. Capasso, "High-power quantum cascade lasers grown by low-pressure metal organic vapor-phase epitaxy operating in continuous wave above 400 K", Appl. Phys. Lett. **88**, 201115 (2006).

Chapter 4

Pulsed external cavity quantum cascade lasers emitting near 10 μm

4.1 Introduction

As mentioned in the introduction chapter, the first realization of an external cavity quantum cascade laser has been reported by Luo et al. in 2001[1]. In this first paper, the authors report tuning ranges of 65 nm (32 cm^{-1}) for a 4.5 μm laser and 88 nm (34 cm^{-1}) for a 5.1 μm laser at liquid nitrogen temperature (80 K). In a following paper by the same group in 2002[2], an improved tuning range of 140 nm (54 cm^{-1}) at 80 K and still 127 nm (49 cm^{-1}) at 243 K is reported for a 5.1 μm laser. These results demonstrated the potential of external cavity quantum cascade lasers as broadly tunable mid-infrared sources. This is mainly because the tuning range of such a laser is limited by the gain bandwidth of the chip and not by the tuning mecanism as in the case of distributed feedback devices. In both works the gain elements used, described in ref. [3], were based on a three-quantum-well vertical transition active region design. In this design, first presented by Faist et al.[4], the radiative transition occurs between two localized electronic states with a strong spatial overlap. That kind of transition is very little sensitive to interface rougness broadening and consequently has a narrow gain bandwidth of $\sim$16 meV (129 cm^{-1}) full width at half maximum at cryogenic temperature and 28 meV (225 cm^{-1}) at room temperature[4]. Knowing this,

one can interpret the aforementioned results as follows: the tuning range is about 50% of the FWHM at cryogenic temperature and then decreases slightly with temperature, even though the gain bandwidth increases, because the performance of the chip decreases. According to this interpretation, a broader tuning range can be obtained by using gain elements with a broader gain bandwidth and/or better performance at high temperature.

4.2 Active region design

Basing our judgement on the previous considerations, we decided to use a bound-to continuum active region design for our external cavity laser because it has a broad gain curve and high performance at room temperature.

4.2.1 The bound-to-continuum design

The bound-to-continuum design was introduced by Faist et al. in 2001[5]. This design and the four-quantum-well or double-phonon resonance design introduced by the same authors in a following paper[6], have been conceived to have a lower threshold current density at room temperature than the traditional three-quantum-well and superlattice ones. To achieve this, the bound-to-continuum structure combines the advantages of these two. It attempts to take advantage of the efficient injection, by resonant tunneling, of the three-quantum-well design and the fast electron extraction, by intraminiband scattering, of the superlattice design.

In this design, the active region spans over a whole period. It consists of a chirped superlattice presenting a tilted lower miniband whose width is maximum in the center and decreases on both sides, close to the injection barriers. The upper state is created in the first minigap by a small well adjacent to the injection barrier. Its wavefunction has its maximum in this well and decreases rapidly in the next ones, like that of an impurity state in a crystal lattice. This configuration of the wavefunction enables resonant tunelling injection with an efficiency comparable to that of the three-quantum-well active region. Furthermore, because the upper state is already confined by the superlattice minigap, the structure does not need

to be separated in an active and an injection region. The carrier extraction from the lower states occurs via fast intraminiband scattering by optical phonon, similarly to that of the superlattice active region.

As shown schematically in the inset of Fig. 4.1, in the bound-to continuum design the oscillator strength is not concentrated in a single transition as in the case of a symmetric superlattice but it is instead spread over two or three transitions, going from the localized upper state to the highest energy states of the lower miniband. As these states are typically separated by ≈ 20 meV, it creates a broader gain curve than for the traditional designs. In addition, because all the transitions share the same initial state and have a low final state population, the broadening of the gain is mainly homogeneous.

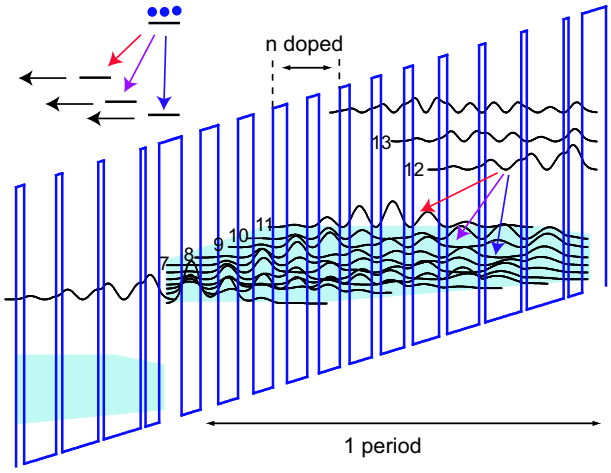

Figure 4.1: Schematic conduction band diagram of the bound-to-continuum design used in this study under an applied electric field of 35 kV/cm with the moduli squared of the computed wavefunctions.

The particular design used in this study (structure N80) is presented in Fig. 4.1. The layer sequence of one period, in nanometers, starting from the injection barrier is **3.9**/2.2/**0.8**/6/**0.9**/5.9/**1**/5.2/**1.3**/4.3/**1.4**/3.8/**1.5**/3.6/**1.6**/ 3.4/**1.9**/3.3/**2.3**/3.2/**2.5**/3.2/**2.9**/3.1 where $In_{0.52}Al_{0.48}As$ layers are in bold, $In_{0.53}Ga_{0.47}As$ in roman and the doped layers (Si 2.3×10^{17} cm^{-3}) are underlined.

4.2.2 Calculation of the gain and spontaneous emission spectra

To compute the lineshape of the gain in the bound-to-continuum design, we used a simple model neglecting the quantum interference[8] between the various transitions. The total gain is assumed to be the sum of the gains of the individual transitions from the upper level i to the lower levels j:

$$G(E) = \sum_j \frac{2\pi^2 e^2 |z_{ij}|^2}{\varepsilon_0 n \lambda_{ij} L_p} (n_i - n_j) \mathcal{L}(E - E_{ij}, \gamma_{ij}) \tag{4.1}$$

where $E_{ij} = E_i - E_j = hc/\lambda_{ij}$ is the photon energy of the $i \rightarrow j$ transition, z_{ij} the dipole matrix element of this transition, and $\mathcal{L}(E, \gamma) = \frac{1}{\pi} \frac{\gamma}{E^2 + \gamma^2}$ is the normalized Lorenzian lineshape function with a full width at half maximum equal to 2γ. When introducing the oscillator strengths $f_{ij} = 2m_0 E_{ij} |z_{ij}|^2 / \hbar^2$, one gets

$$G(E) = \frac{\pi \hbar e^2}{2 m_0 \varepsilon_0 n L_p c} \sum_j f_{ij} (n_i - n_j) \mathcal{L}(E - E_{ij}, \gamma_{ij}) \tag{4.2}$$

Because of the short lifetimes of the miniband levels j compared to the upper state i and the large energy separation between the ground state and the optically active levels of the miniband, the population of state j can be neglected compared to level i. In this approximation, the normalized lineshape function of the bound-to-continuum design is

$$L_{BTC}(E) = \frac{\sum_j f_{ij} \mathcal{L}(E - E_{ij}, \gamma_{ij})}{\sum_j f_{ij}} \tag{4.3}$$

It is a sum of lorentzian lineshapes for each individual transition weighted by their oscillator strengths. The integrated gain is proportional to the sum of the oscillator strengths.

The energies, dipole matrix elements, and oscillator strengths of the optically active transitions in structure N80 are listed in Table 4.1. Four transitions have a non negligible oscillator strength: the transitions from level 12 to levels 11, 10, 9, and 8.

Transition	E_{ij} (meV)	z_{ij} (nm)	f_{ij}	$\gamma_{ij}/\gamma_{12,10}$
12→11	105.8	1.58	6.96	1.29
12→10	128.2	2.42	19.70	1
12→9	143.6	1.25	5.87	1.03
12→8	162.8	0.35	0.54	1.06

Table 4.1: Photon energies, dipole matrix elements, oscillator strengths, and relative broadenings for the radiative transitions of structure N80 under an applied electric field of 35 kV/cm.

As we saw in chapter 2, the broadening of mid-infrared intersubband transition is mainly due to interface roughness and is given by:

$$\gamma_{ij} = \frac{m^*\Delta^2\Lambda^2}{2\hbar^2}\sum_k (F_{ii}^k - F_{jj}^k)^2 \int_0^\pi d\theta e^{-q^2\Lambda^2/4} \tag{4.4}$$

where the index k runs over the interfaces of the structure, $F_{ii}^k = |\partial E_i/\partial z_k| = \Delta E_c|\chi_i(z_k)|^2$, z_k being the position of the k^{th} interface, and $q^2 = 4m^*E(1-\cos\theta)/\hbar^2$. Since the rightmost integral depends weakly on energy for typical values of Λ, one can use this formula to compute ratios between linewidths of intersubband transitions without having to know the growth dependent parameters Δ and Λ. We evaluated these ratios numerically for the various optically active transitions of our structure. The results are listed in Table 4.1. The broadening of transitions 12→10, 12→9, and 12→8 are equal within a few percents and that of transition 12→11, the most diagonal one, is about 30% larger.

This calculation allows to reduce the number of parameters necessary to describe the structure. If in addition we admit that the energies of the transitions vary linearly with the structure thickness, keeping constant the ratios between them, we are left with only two parameters. For convenience, we choose the energy and the broadening of the transition with the strongest oscillator strength: $E_{12,10}$ and $\gamma_{12,10}$.

It should be noticed that, in opposition to the case of a single transition, the spontaneous emission spectrum is not proportional to the gain spectrum. Recalling the spontaneous

emission rate

$$W_{ij}^{sp} = \frac{e^2 n}{3\pi c^3 \varepsilon_0 \hbar^4} E_{ij}^3 |z_{ij}|^2 = \frac{e^2 n}{6\pi \hbar^2 m_0 \varepsilon_0 c^3} E_{ij}^2 f_{ij} \tag{4.5}$$

The spectrum of the emitted light is proportional to $\sum_j W_{ij}^{sp} E_{ij}$, that is to $\sum_j E_{ij}^3 f_{ij} \mathcal{L}(E - E_{ij}, \gamma_{ij})$.

4.2.3 Measured spontaneous emission spectra

35 periods of the structure presented in Section 4.2.1 were grown by MBE using lattice-matched InGaAs and AlInAs alloys on an InP substrate. An InP top cladding was then grown on it by MOVPE. In order to measure the spontaneous emission spectra of the structure, a part of the epilayer was processed in square mesas and the substrate was polished with a 45° tilt. The measurements were realized using a Nicolet 860 FTIR in step scan mode with a liquid-nitrogen cooled MCT detector and a lock-in signal recovery scheme. The repetition rate was 100 kHz and the pulse duration 200 ns. Spectra were recorded at heat-sink temperatures of 80 and 300 K for biases ranging from 8 to 12 V.

We observed a full width a half maximum of 175 cm^{-1} at 80 K and 295 cm^{-1} at 300 K with, in both cases, a weak dependence on the applied voltage. A spectrum taken at 300 K under a bias of 8 V is shown in Fig. 4.2. The experimental data (squares) are plotted along with a fit (solid line) based on the model presented in section 4.2.2. The best fit parameters obtained are $E_{12,10} = 124.4$ meV and $\gamma_{12,10} = 12.8$ meV. The agrement with the measured spectrum is good except for for the energy region below 100 meV. We attribute this to a value of 12-11 transition oscillator strength lower than the computed one resulting from dephasing scattering. Indeed, the difference between the expectation values of the position operator in states 12 and 11 equals 23.9 nm which is much larger than usually seen in QC structures. The extra luminescence intensity compared to the model observed in the energy ranges going from 150 to 190 meV and from 210 to 240 meV is attributed to the radiative transitions from level 13 to levels 11, 10, 8, and 7, the strongest ones from this state, which have energies of 158, 180, 215, and 230 meV, respectively.

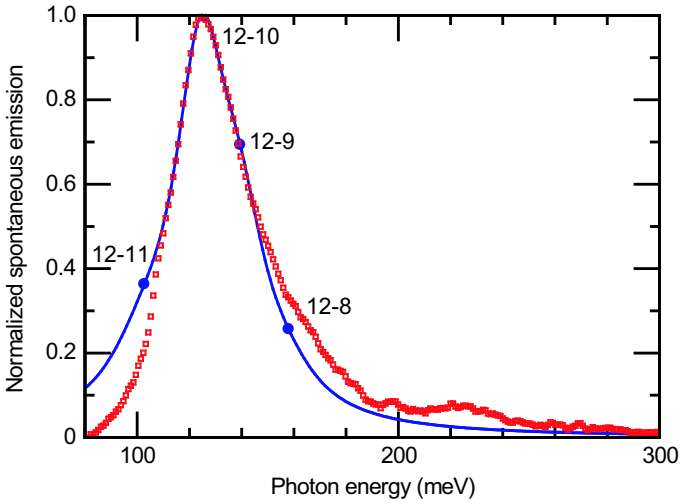

Figure 4.2: Squares: spontaneous emission (electroluminescence) spectrum of the structure measured at 300 K under a bias of 8V. Solid line: fit of the experimental data. The solid circles indicate the energies of the individual transitions.

4.3 Fabry-Pérot chip performance

The epilayer N80 described in previous section was processed in 32 μm wide ridge waveguides using standard processing without lateral regrowth or thick electroplated gold. The ridges were cleaved and soldered junction-side up on copper submounts. The LIV characteristics of a 750 μm-long sample are shown in Fig. 4.3. The measurements were performed using an AVTECH AVL-2-C pulse generator providing 100 ns pulses with a repetition rate of 5 kHz, i.e. at a duty cycle of 0.05%. The sample was mounted on a room temperature copper heatsink without any active cooling. The large noise on the output power curves is due to the small average power (< 0.5 mW). This chip had a threshold current density $J_{th} = 4.46$ kA/cm^2, a slope efficiency $dP/dI = 511$ mW/A and a maximum peak power $P_{max} = 516$ mW with facets as cleaved. With a ZnSe/Au high reflection coating on its back facet, we measured $J_{th} = 4.06$ kA/cm^2, $dP/dI = 678$ mW/A, and $P_{max} = 830$ mW. Its lasing spectrum was centered at 9.9 μm (1010 cm^{-1}) and was 90 cm^{-1} broad under an applied bias of 10.5 V. Chips with 1 and 1.5 mm-long cavities were also mounted and tested. They showed higher output power (more than 1.5 W for 1.5 mm-long devices with HR coating) but with a larger threshold current density. This unexpected behavior is attributed to

defects introduced in the structure most probably during the cladding overgrowth or the processing. We measured the lowest J_{th} in the shortest samples because the probability that they contain a defect is smaller.

For the external cavity experiments, the front facet of the chips were AR coated with a ZnS quarter-wave layer (1.14 μm). The computed Fresnel reflectivity is 4%. Because of the above mentioned defects in the waveguide, a measurement of the actual reflectivity of the facet was not possible.

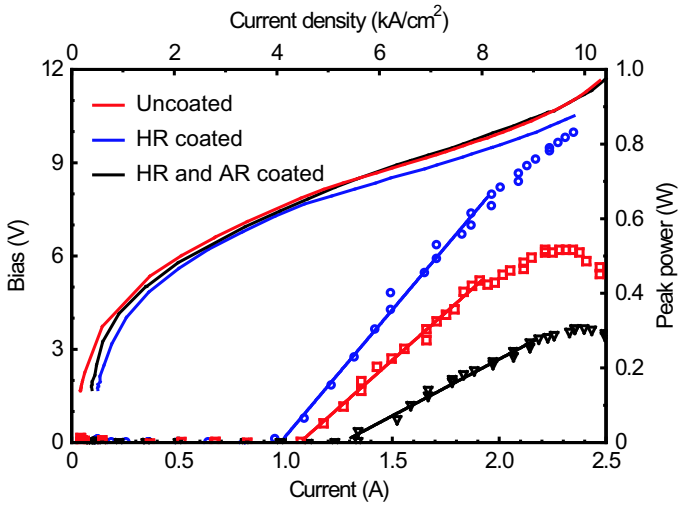

Figure 4.3: Light intensity and voltage versus current characteristics of a 0.75 mm long chip. Measurements were done at room temperature with a duty cycle of 0.05%.

4.4 External cavity laser performance

For the external cavity laser measurements, we used the Littrow configuration. The first order reflection of the grating provided the optical feedback and the output was taken from the zeroth order. The collimating lens was a broadband AR coated infinity-conjugate f/0.6 germanium aspheric with a numerical aperture of 0.83. The grating had a spatial frequency of 150 grooves per mm and was blazed for a wavelength of 9.3 μm. We deposited 60 nm of gold on its aluminum surface by ion-beam sputtering to improve its reflectivity. It was

placed on a manual precision rotation platform (1 arc minute resolution). A mirror was also mounted on the platform, parallel to the grating, to ensure that the output beam direction stays unchanged during the rotation. The chip was operated on a thermoelectric cooler in a commercial QC laser housing (Alpes Lasers SA) from which the ZnSe window has been removed to reduce intracavity losses. The orientation was chosen so that the light reached the grating in TE polarization.

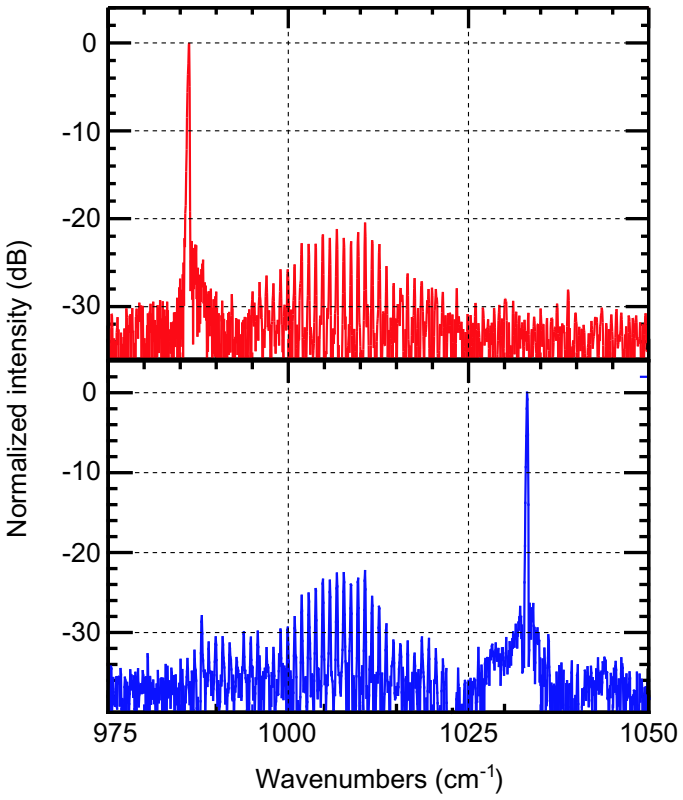

Figure 4.4: Spectra of the pulsed external cavity laser for two different grating angles.

The external cavity laser could be tuned on the Fabry-Pérot modes of the gain chip between 947 cm^{-1} (10.56 μm) and 1097 cm^{-1} (9.11 μm) by varying the grating angle. This tuning range of 150 cm^{-1} (1.45 μm) is equal to 15% of the free running frequency. Figure 4.4 shows two typical spectra of the laser with a logarithmic scale. The position of the main mode is determined by the grating angle but other modes are present around the maximum

of the gain curve. The FWHM of the grating selected mode is about 0.2 cm^{-1} (6 GHz).

The average optical power and side mode suppression ratio (SMSR) as functions of the emission frequency are shown in Fig. 4.5. These data were obtained in a series of measurements at a constant temperature of 20°C, under an applied bias of 8 V, with a pulse duration of 50 ns and a repetition rate of 500 kHz (duty cycle = 2.5%). The SMSR exceeds 20 dB over a range of 50 cm^{-1} and 10 dB over 110 cm^{-1}. The average optical power exceeds 1 mW (which corresponds to a peak power of 40 mW) over 100 cm^{-1}.

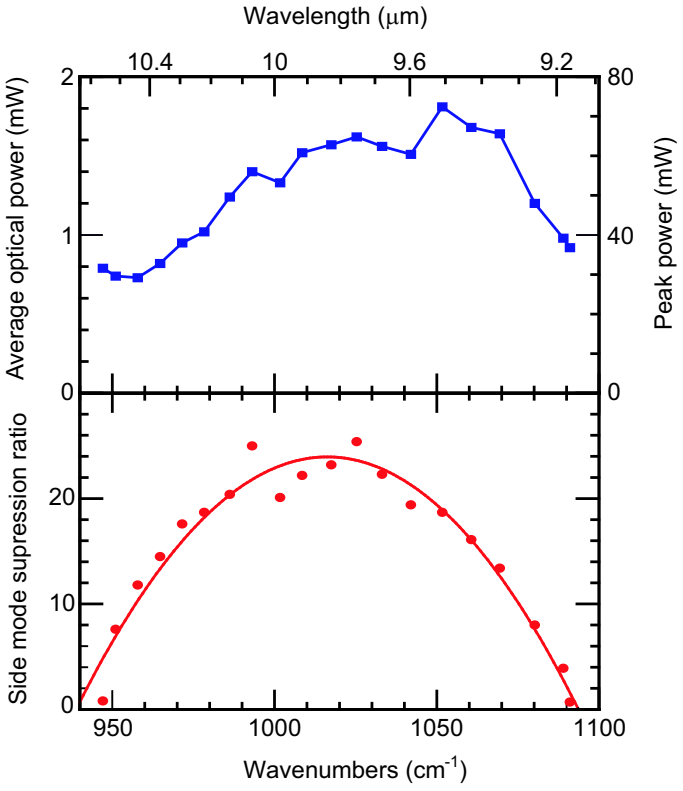

Figure 4.5: Measured average optical power and side mode suppression ratio of the external cavity laser for various emission frequencies.

4.5 Time-resolved spectra

Because of the large difference between the round-trip times of the chip Fabry-Pérot modes (30 ps for a 1.5 mm-long cavity) and the external cavity mode (570 ps for an 8 cm-long free space segment), we expected mode competition to occur at the beginning of the current pulses. To investigate this behavior, we measured laser spectra during short time windows at various instants during the pulse.

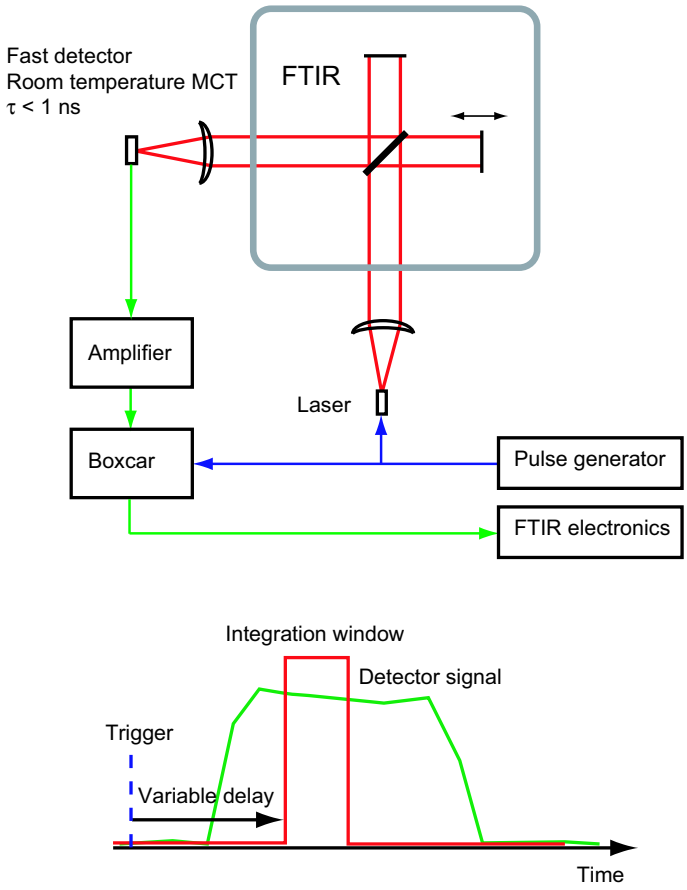

Figure 4.6: Schematic drawing of the setup for measurement of time-resolved spectra.

4.5.1 Experimental setup

A schematic drawing of the setup that we used for measurement of time-resolved spectra in presented in Fig. 4.6. It consists of a Nicolet 860 FT-IR spectrometer with a fast external detector (room temperature MCT with a response time $\tau < 1$ ns, Vigo Systems SA) followed by a 32 dB amplifier (Sonoma Instrument Co, model 310) and a gated boxcar integrator (Stanford Research System, model 250). The integrator is triggered by the pulse generator driving the laser. The variable gate delay and width allow to measure spectra of various parts of the pulses. The repetition rate was set to 18.5 kHz, slightly below the maximum operating frequency of our integrator (20 kHz), and the scanning speed v_{sc} of the FTIR was set to 0.3165 cm/s so that the sampling frequency $f_S = v_{sc}/(0.5\,\lambda_{HeNe})$ was equal to 10 kHz, ensuring that the output of the integrator is refreshed at least once between the aquisition of two consecutive data points.

4.5.2 Results

Some resulting spectra, taken at 2 ns intervals with a 2 ns long gate, are shown in Fig. 4.7. They clearly display the mode competition occurring at the beginning of the pulse. The Fabry-Pérot cavity modes lase first because of their shorter round trip time, but then vanish when the grating-selected mode, having a lower threshold gain, starts to lase. The linewidth of these spectra is smaller than the resolution of our spectrometer (3.75 GHz), proving that the relatively large time-averaged linewidth is due to the thermal drift of the wavelength during the pulse. The inset is a spectrum recorded using a gate covering the end of the pulse, from 12 ns to 50 ns. During this time interval the laser is single mode in the limit of our spectrometer resolution ($\sim$30 dB).

4.5.3 Dynamical model

In order to describe this transitory regime, we rewrote the QCL rate equations presented in Section 2.1.5 for two photon flux densities S_{FP} and S_{EC} describing the chip Fabry-Pérot modes and the external cavity mode, respectively. To take into account the longer round

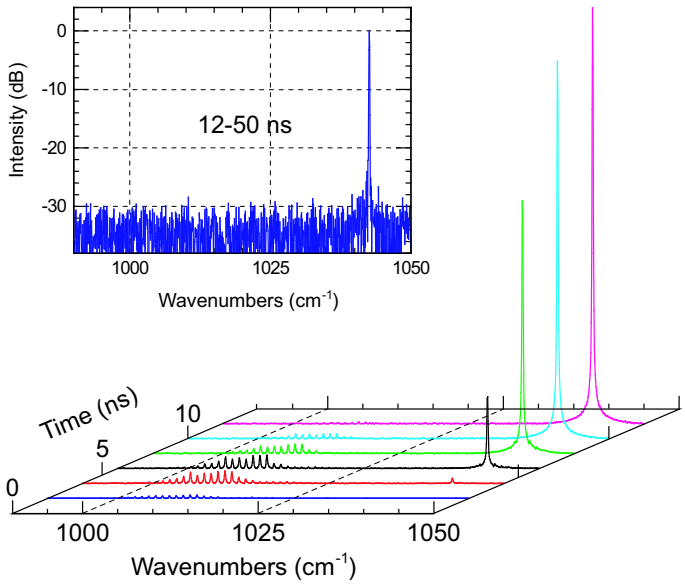

Figure 4.7: Time resolved spectra of an external cavity laser. The spectra are taken at 2 ns intervals with a 2 ns long gate. Inset: Logarithmic scale spectrum of the end of the pulse (from 12 ns to 50 ns).

trip time of the latter, we multiplied its speed by $1/\rho_{\text{cav}}$ where $\rho_{\text{cav}} = 1 + \frac{l}{nL}$ is the ratio of the (optical) lengths of the two cavities, L being the chip length, n its refractive index, and l the distance from its front facet to the external grating:

$$\frac{dn_3}{dt} = \frac{J}{q} - \Big[S_{\text{FP}} g_{\text{FP}} + S_{\text{EC}} g_{\text{EC}}\Big](n_3 - n_2) - \frac{n_3}{\tau_3} \tag{4.6}$$

$$\frac{dn_2}{dt} = \frac{n_3}{\tau_{32}} + \Big[S_{\text{FP}} g_{\text{FP}} + S_{\text{EC}} g_{\text{EC}}\Big](n_3 - n_2) - \frac{n_2}{\tau_2} \tag{4.7}$$

$$\frac{dS_{\text{FP}}}{dt} = \frac{c}{n}\Big[\Big(g_{\text{FP}}(n_3 - n_2) - \alpha_{\text{FP}}\Big) S_{\text{FP}} + \frac{\beta n_3}{\tau_{sp}}\Big] \tag{4.8}$$

$$\frac{dS_{\text{EC}}}{dt} = \frac{c}{\rho_{\text{cav}} n}\Big[\Big(g_{\text{EC}}(n_3 - n_2) - \alpha_{\text{EC}}\Big) S_{\text{EC}} + \frac{\beta n_3}{\tau_{sp}}\Big] \tag{4.9}$$

$$\tag{4.10}$$

where g_{FP} and g_{EC} are the values of the gain cross section $g_c(\nu)$ at its maximum and at the grating-selected frequency ν_{EC}, respectively. α_{FP} and α_{EC} are the total losses of the AR coated chip and the external cavity (see Section 2.2.1). β, the fraction of the spontaneous emission emitted in the mode, is supposed to be the same for both modes for simplicity. We

solved these coupled differential equations numerically. The resulting computed electronic populations and photon flux densities (per unit length, per period) are shown on Fig. 4.8. The experimentally observed behavior is well reproduced.

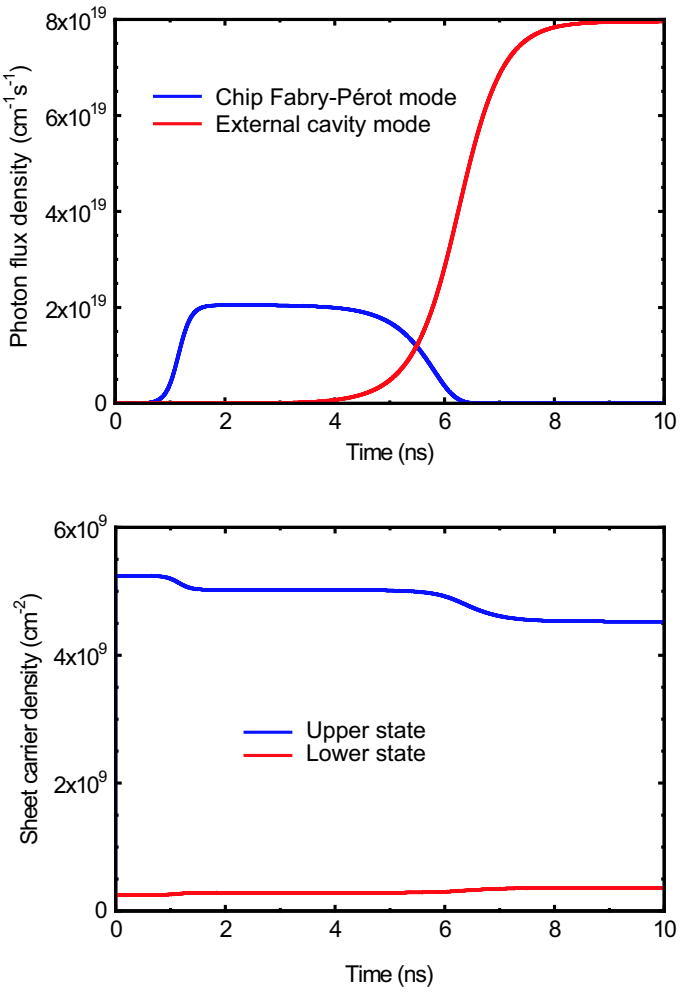

Figure 4.8: Simulated electronic populations and photon flux densities as functions of time. The time origin corresponds to the begining of the current pulse.

After a few picoseconds, the population inversion Δn reaches the value $J\tau_{\text{eff}}/q$. The photon flux densities grow as e^{Gvt} where $G = g_c\Delta n - \alpha$ is the net modal gain and v the speed of light. Despite a higher net gain due to smaller losses, S_{EC} increases more slowly because of its ≈ 10 times smaller effective speed $c/(\rho_{\text{cav}}n)$. As S_{FP} increases, Δn decreases because of stimulated emission until it reaches the value $\alpha_{\text{FP}}/g_{\text{FP}}$. Then S_{FP} is not amplified any more

and saturates, but S_{EC} continues to grow because its net gain is still positive. Doing this it decreases further the population inversion which becomes too small to compensate the losses for S_{FP}. The FP modes thus vanish and the external cavity mode continues to grow until the population inversion reaches the equilibrium value $\alpha_{\mathrm{EC}}/g_{\mathrm{EC}}$.

Bibliography

[1] G. P. Luo, C. Peng, H. Q. Le, S. S. Pei, W.-Y. Hwang, B. Ishaug, J. Um, J. N. Baillargeon, and C.-H. Lin, "Grating-tuned external-cavity quantum-cascade semiconductor lasers", Appl. Phys. Lett. **78**, 2834 (2001).

[2] G. Luo, C. Peng, H. Q. Le, S.-S. Pei, H. Lee, W.-Y. Hwang, B. Ishaug, and J. Zheng, "Broadly wavelength-tunable external cavity, mid-infrared quantum cascade lasers", IEEE J. Quantum Electron. **38**, 486 (2002).

[3] B. Ishaug, W.-Y. Hwang, J. Um, B. Guo, H. Lee, and C.-H. Lin, "Continuous-wave operation of a 5.2 μm quantum-cascade laser up to 210 K", Appl. Phys. Lett. **79**, 1745 (2001).

[4] J. Faist, F. Capasso, C. Sirtori, D. L. Sivco, J. N. Baillargeon, A. L. Hutchinson, S. N. G. Chu, and A. Y. Cho, "High power mid-infrared ($\lambda \sim 5$ μm) quantum cascade lasers operating above room temperature", Appl. Phys. Lett. **68**, 3680 (1996).

[5] J. Faist, M. Beck, T. Aellen, and E. Gini, "Quantum-cascade lasers based on a bound-to-continuum transition", Appl. Phys. Lett. **78**, 147 (2001).

[6] D. Hofstetter, M. Beck, T. Aellen, and J. Faist, "High-temperature operation of distributed feedback quantum-cascade lasers at 5.3 μm", Appl. Phys. Lett. **78**, 396 (2001).

[7] J. Faist, D. Hofstetter, M. Beck, T. Aellen, M. Rochat, and S. Blaser, "Bound-to-continuum and two-phonon resonance quantum cascade lasers for high duty cycle, high temperature operation", IEEE J. Quantum Electron. **38**, 533 (2002).

[8] J. Faist, F. Capasso, C. Sirtori, K. W. West, and L. N. Pfeiffer, "Controlling the sign of quantum interference by tunnelling from quantum wells", Nature (London) **390**, 589 (1997).

Chapter 5

Continuous-wave external cavity quantum cascade laser emitting near 5.2 μm

5.1 Introduction

In previous chapter, we presented broadly tunable (150 cm^{-1} around $\lambda \cong 10$ μm) external cavity QCLs based on a bound-to-continuum design. The major drawback of these lasers, which worked in pulsed mode on a thermoelectric cooler, for spectroscopic applications was the relatively poor side-mode suppression ratio (SMSR) $\leq$ 25 dB. However, time-resolved spectra showed that the unwanted Fabry-Pérot modes of the gain chip lased only during a few ns at the beginning of each pulse. Two strategies to supress these parasitic modes are conceivable. One is to reduce the coupling-facet reflectivity by improving its anti-reflection (AR) coating so that enough power can be extracted while keeping the current intensity lower than the threshold of these modes. The other is to operate the laser in continuous wave (CW) or quasi-CW mode. The latter has the advantage of producing a narrower linewidth. The laser linewidth is a very important parameter for spectroscopy because it determines the ultimate limit to the resolution of the measured spectra. A narrow linewidth is also beneficial for trace gas sensing because it enhances absorption depth for a given

concentration and improves discrimination of the targeted species from nearby interfering absorption features[1].

In this chapter I will present a broadly tunable EC-QCL that can be operated CW on thermoelectric cooler.

5.2 Active region design

The 5.2 μm active region that we used is based on a bound-to-continuum design similar in principle to the one described in chapter 4. Strain-compensated $In_{0.6}Ga_{0.4}As$ and $In_{0.44}Al_{0.56}As$ alloys were used instead of the lattice-matched ones used for the 10 μm laser. These relative concentrations of III elements create a larger conduction band discontinuity of 620 meV, enabling the design of structures emitting in the desired energy range ($\sim$ 240 meV) with an energy confinement that is strong enough to prevent electrons from escaping from the upper state into the continuum. The lattice mismatch parameter $(a - a_s)/a_s$ where a is the lattice parameter of the grown material and a_s that of the substrate ($\cong$ 0.5% for InGaAs and $\cong -0.5\%$ for InAlAs) is chosen so that the total strain is balanced over one period, and the thicknesses of each barrier and well are kept below the critical thickness to avoid strain relaxation. A schematic conduction band diagram of the structure with the moduli squared of the computed wavefunctions is given in Fig. 5.1. The layer sequence of one period, in nanometers, starting from the injection barrier is **4.2**/1.3/**1.4**/5.0/**1.5**/4.4/**1.6**/3.9/**1.8**/2.9/**1.9**/2.6/ **2.0**/2.3/**2.1**/2.2/**2.3**/2.1/**3.0**/2.1 where InAlAs barriers are in bold, InGaAs wells in roman, and the n-doped layers (Si, 1×10^{17} cm^{-3}) are underlined. The same active region design was previously used by Blaser, Yarekha et al. for the first demonstration of single-mode DFB QCLs operating CW at room temperature[2]. The core of the waveguide, consisting of a 200 nm-thick (lattice-matched) InGaAs (Si, 6×10^{16}cm^{-3}) spacer, 25 periods of active region, and a 300 nm-thick InGaAs (Si, 6×10^{16}cm^{-3}) spacer, was again grown by MBE. The upper cladding was subsequently grown by MOCVD. It consisted of a 1 μm-thick InP (Si, 2×10^{17}cm^{-3}) layer, a 0.85 μm-thick InP (Si, 2×10^{18}cm^{-3}) layer, and a 50 nm-thick InGaAs (Si, 2×10^{19}cm^{-3}) layer.

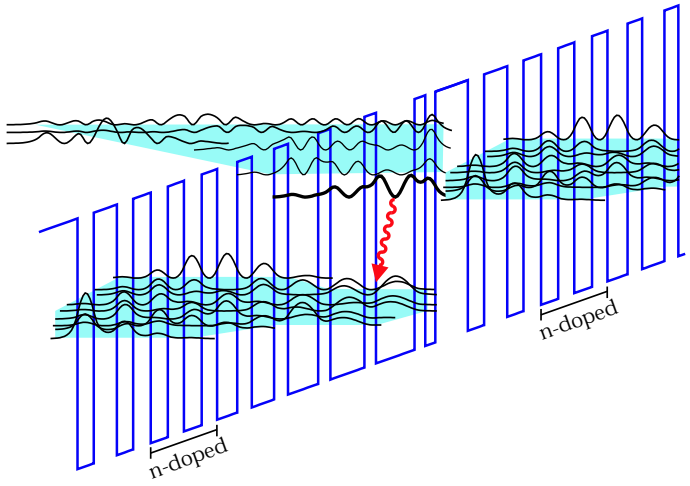

Figure 5.1: Schematic conduction band diagram of one stage of the structure under an applied electric field of 67 kV/cm. The moduli squared of the wavefunctions are shown (in bold the upper state of the laser transition) and the wavy arrow indicate the radiative transition.

Electroluminescence spectra of mesa processed samples, acquired in a similar way to those described in section 4.2.3 resulted in a full width at half maximum of 294 cm^{-1} at room temperature[2].

5.3 Chip fabrication and performance

The epilayer was processed in 10 to 16 μm-wide ridge waveguides by wet etching as described in chapter 3. A 300 nm-thick Si_3N_4 layer was deposited by plasma-enhanced chemical vapor deposition for electrical insulation and opened on top by reactive ion etching. After the evaporation of metallic contacts on the top and bottom of the sample, a 5 μm-thick gold layer was electroplated on the ridges to improve heat dissipation.

The lasers with the narrowest waveguides demonstrated CW operation at the highest temperatures thanks to a better heat dissipation. Figure 5.2 shows the applied bias voltage and CW output power of the gain element used in our external cavity experiments as functions of the injection current at a heat-sink temperature of -30°C. This chip was 10 μm wide and 3 mm long. With both facets as cleaved, the CW threshold current density J_{th} at

this temperature was 1.73 kA/cm^2 and the maximum CW operation temperature was 0°C. After deposition of an Al_2O_3/Au (300 nm/100 nm) high reflection coating on the back facet, J_{th} decreased to 1.35 kA/cm^2 at -30°C, and the maximum operating temperature reached 35°C, with still more than 20 mW of output power at 25°C. From this threshold variation, and assuming reflectivities of 27.4% for uncoated facets and 95% for HR coated facets, we deduced $\alpha_w = 5$ cm^{-1} for the waveguide losses.

As AR coating, we deposited a quarter-wave layer of Al_2O_3 on the front facet. This material have a slightly lower refractive index compared to the one needed for zero reflectivity (1.61 instead of 1.85) but has an excellent adhesion on the chip facets. The computed (Fresnel) reflectivity is 1%. After deposition, we measured $J_{th} = 2.03$ kA/cm^2 at -30°C. Using the value of α_w deduced before, we computed a residual reflectivity $R_{AR} = 3\%$.

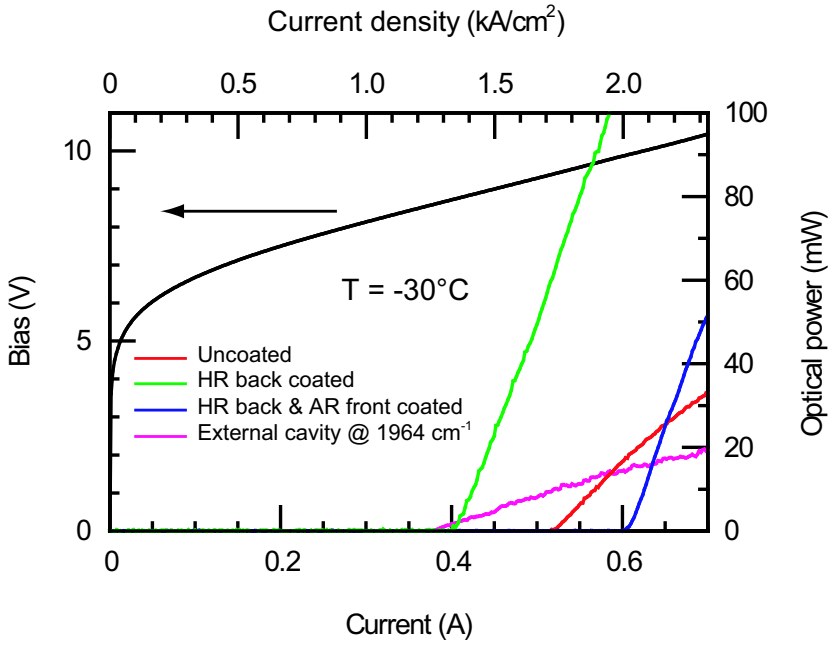

Figure 5.2: Bias voltage and CW optical power of the gain element and the external cavity laser as functions of the injection current at a heat-sink temperature of -30 °C. The sample is 10 μm wide and 3 mm long.

5.4 Setup for continuous-wave operation

Because the best QCL chips available at the time we developed our continuous-wave (CW) EC-QCL were lasing CW only up to room temperature or slightly above, we designed the setup for CW operation down to -30°C. Because water condensation (and ice formation below 0°C) would damage the chip, it is necessary to operate it in an airtight enclosure when the heatsink temperature is set below room temperature. Our previous experience with pulsed lasers demonstrated that a significantly larger tuning range can be achieved without window in the extended cavity, because even an AR coated ZnSe window introduces losses reducing the optical feedback. We thus decided to put the entire setup, that is the laser with its thermoelectric cooling, the collimating lens on a XYZ stage, and the grating on a rotation stage, in a large aluminum enclosure (see Fig. 5.3). A transparent plexiglass lid was used in order to make the alignment easier. The laser was operated under low vacuum ($\approx 10^{-2}$ mbar). The XYZ stage was actuated with three picomotors (New Focus, model 8321) and the rotation stage was a piezoceramic actuator with close-loop control (New focus, model 8103). As in our previous setup (see chapter 4), a mirror parallel to the grating was mounted on the rotation stage to keep the beam direction unchanged when rotating the grating and the output beam was extracted through a ZnSe window.

5.5 Laser performance

5.5.1 Threshold current

Figure 5.2 shows an output power versus current characteristic of the ECQCL tuned near the maximum of the gain curve. The addition of the grating feedback lowered the threshold current density of the chip down to 1.26 kA/cm^2 at -30°C. The ratio of this value to that of the HR coated chip allows one to calculate the equivalent reflectivity of the external part of the cavity $R_{EC} = 36\%$.

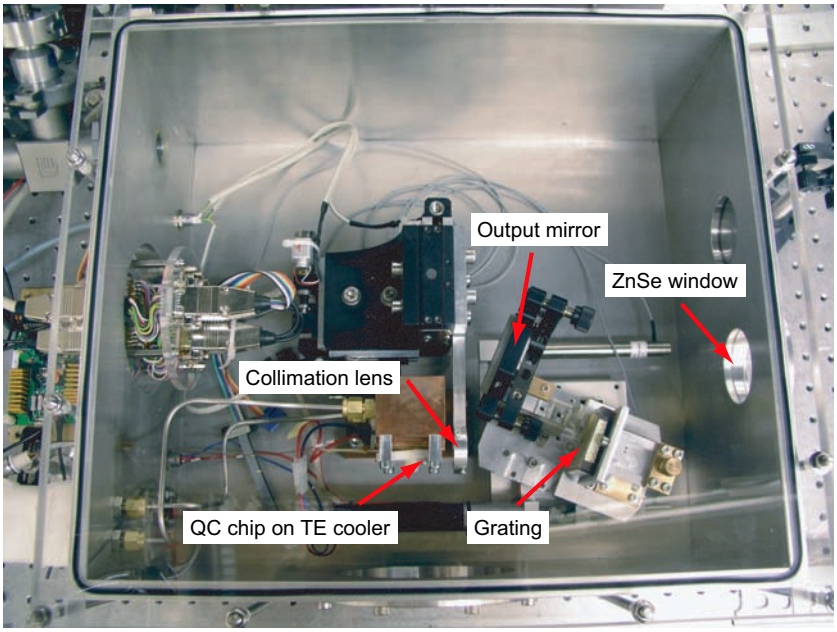

Figure 5.3: Photograph of the EC-QCL setup for continuous-wave operation. All the elements of the external cavity are placed in an airtight enclosure to avoid water condensation on the chip when it is operated below room temperature.

5.5.2 Coarse tuning range and spectral purity

The laser could be tuned over 174 cm^{-1} (0.46 μm) from 4.94 to 5.4 μm, that is over 9% of the center frequency. The side-mode suppression ration was larger than 25 dB over 169 cm^{-1} (see Fig. 5.4) and the laser was single-mode with a SMSR $\geq$ 30 dB (the noise level of the FTIR) over 142.5 cm^{-1} (0.37 μm) from 4.95 to 5.32 μm, i.e. over 7% of the center frequency. When trying to tune further away from the center of the gain curve, the laser jumped back to the chip Fabry-Pérot modes.

5.5.3 Output power

Figure 5.5 displays the optical power of the external cavity laser as a function of the lasing wavelength at constant current values of 600 and 650 mA, at a heat-sink temperature of $-30°C$. With 650 mA injected into the structure, the output power was in excess of 10 mW over $\sim$100 cm^{-1} and in excess of 5 mW over $\sim$130 cm^{-1}. This power level is sufficient

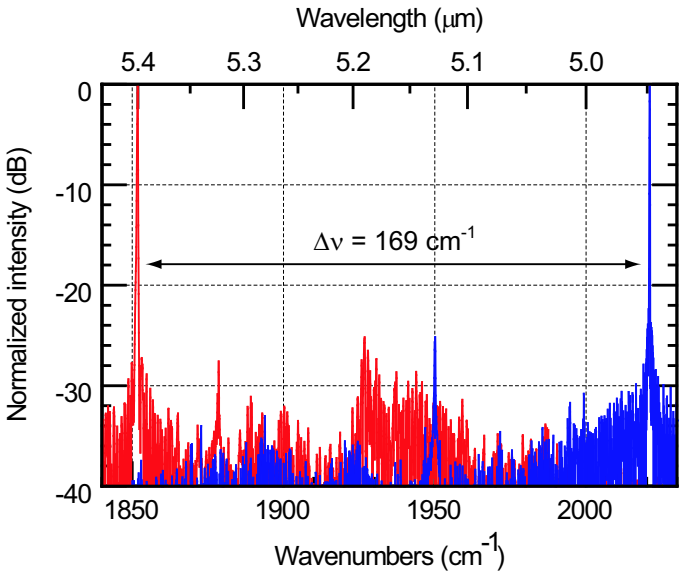

Figure 5.4: Extreme spectra of the external cavity laser with a SMSR $\geq$ 25 dB.

to achieve trace-gas detection with ppb sensitivity using multipass absorption spectroscopy with a thermoelectrically cooled detector (see for example ref. [1]).

5.5.4 Fine tuning

As for the 10 μm laser described in previous chapter, rotating the grating allowed only discrete tuning on the Fabry-Pérot modes of the gain element separated by $1/2nL \cong 0.5$ cm^{-1}. Fine tuning was achieved by varying simultaneously the grating angle and the injected current or the heat-sink temperature. As expected, the dependence of the lasing frequency on the electrical power was linear (see top part of Fig. 5.6), with a tuning coefficient $d\nu/dP = -0.98$ cm^{-1}/W, corresponding to $d\nu/dI = -0.013$ cm^{-1}/mA at $I = 600$ mA. The temperature tuning coefficient was -0.17 cm^{-1}/K (see the bottom part of Fig. 5.6).

Since the distance l between the gain element and the grating was not varied when the laser was tuned, mode hopping was expected on the Fabry-Pérot modes of the extended cavity, separated by $1/2(nL + l) \cong 0.05$ cm^{-1}. The resolution of our FTIR spectrometer (0.125 cm^{-1}) was insufficient to observe this behavior. It was however confirmed by an

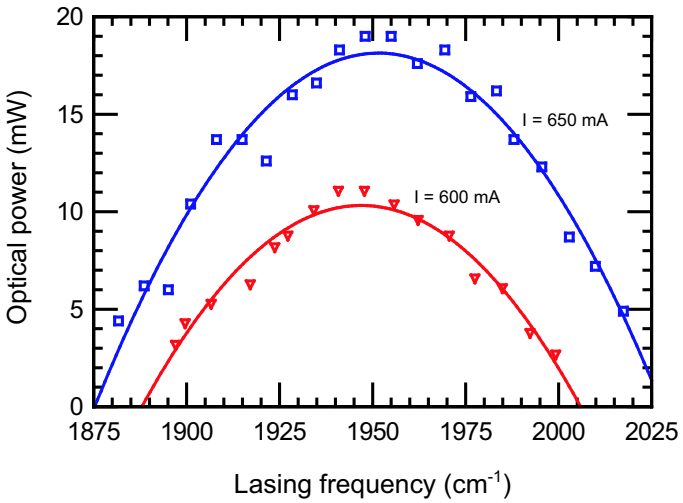

Figure 5.5: Output power of the external cavity laser as a function of frequency for two different values of injection current at $T = -30°\mathrm{C}$.

observed modulation superimposed on the usual linear behavior of the light intensity versus current curves of the external cavity laser (see Fig. 5.7). The average separation between two consecutive local minima of output power was 4.8 mA (see inset of Fig. 5.7) which corresponds well to the current needed to tune the gain chip over 0.05 cm^{-1}.

5.6 Laser linewidth

As mentioned in the indroduction of this chapter, the main advantage of CW QCLs compared to pulsed ones for spectroscopic applications is their narrower linewidth. In pulsed mode, the time-averaged linewidth is limited by the large drift of the instantaneous frequency accompanying the temperature increase during the pulse (thermal chirp). In CW the ultimate limit to the linewidth, given by the Schawlow-Townes formula, is very narrow for QCLs because of the small linewidth enhancement factor. In section 5.6.1 we will compute this limit for a free-running chip and see how it is modified in the case of an external cavity laser. Then, in section 5.6.2, we will present an experimental determination of an upper limit to the linewidth.

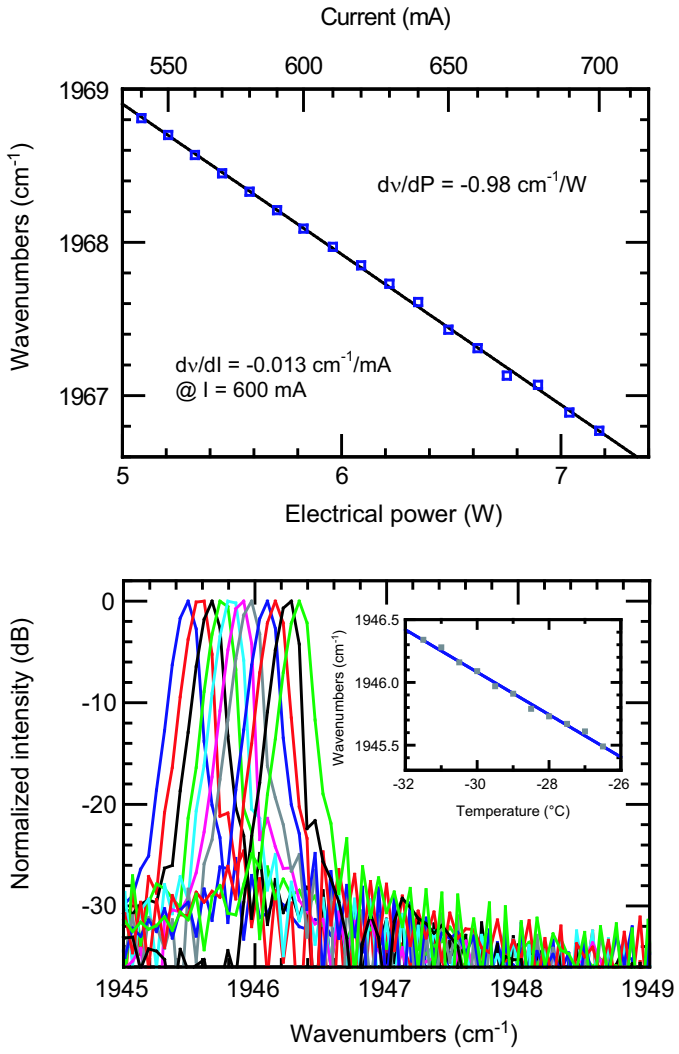

Figure 5.6: Top graph: fine tuning behavior of the external cavity laser when the grating angle and the injected current are varied simultaneously The current scale is quadratic. Bottom graph: Laser spectra measured at various heat-sink temperatures. Inset: dependence of the lasing frequency on temperature.

5.6.1 Theoretical model

The linewidth of a semiconductor laser is given by the Schawlow-Townes formula[3] modified by Henry[4]:

$$\Delta\nu = \frac{\pi h\nu\,{\Delta\nu_c}^2}{P}\,\frac{\alpha_m}{\alpha_{tot}}\,\frac{n_{3t}}{n_{3t}-n_{2t}}\,(1+\alpha_e^2) \tag{5.1}$$

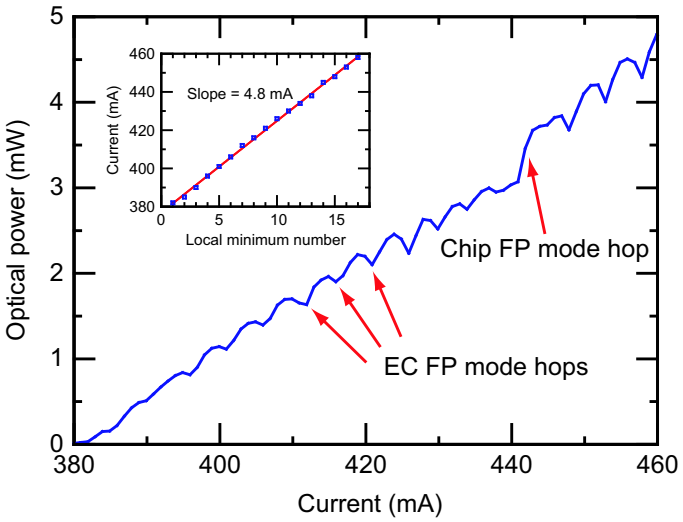

Figure 5.7: Optical power of the external cavity laser as a function of current. The measurement was done with 1 mA current steps and 200 ms integration time so that the temperature could stabilize at each point. The local minima correspond to mode hops between two consecutive modes of the extended cavity. Inset: values of the current at the local minima. The average spacing is 4.8 mA.

where ν is the lasing frequency, α_{tot} the total losses of the cavity, α_m the mirror losses of the output facet, P the output power, $\Delta\nu_c = \alpha_{tot}c/(2\pi n)$ the FWHM of the cavity resonance, n_{3t} and n_{2t} the populations of the upper and lower states of the laser transition at threshold, and α_e the linewidth enhancement factor introduced by Henry. Using the QCL rate equations presented in Section 2.1.5, one can show that

$$\frac{n_{3t}}{n_{3t} - n_{2t}} = \left(1 - \frac{\tau_2}{\tau_{32}} - \frac{q}{\tau_3 J_{th}}\, n_2^{\text{therm}}\right)^{-1} \tag{5.2}$$

where τ_3 and τ_2 are the lifetimes of the upper and lower states, τ_{32}^{-1} is the scattering rate from level 3 to level 2, and n_2^{therm} is the thermal population of level 2. Assuming a lorentzian lineshape with a FWHM equal to $2\gamma_{32}$ for the intersubband transition, the linewidth enhancement factor of a QCL can be expressed as $\alpha_e(\nu) = -(\nu - \nu_{32})/\gamma_{32}$ and thus is equal to zero at the maximum of the gain curve. For the gain element used in this study, $\Delta\nu = 88$ Hz is expected for an output power of 50 mW, without front facet coating and grating feedback. According to Kazarinov and Henry [5], the linewidth of a semiconductor laser is reduced

by a factor F^2 with $F = 1 + l/n_g L$ when its cavity (length L, group refractive index n_g) is extended by a passive free-space section of length l. For our setup, $F \cong 10$ and a linewidth smaller than 2 Hz is expected for the external cavity laser even at the extremities of the tuning range ($\nu - \nu_{32} \cong 100$ cm^{-1}) where $\alpha_e \cong 0.7$.

5.6.2 Experimental determination of an upper limit using heterodyne mixing

Standard FTIRs, which have a resolution of the order of 0.1 cm^{-1} (3 GHz), are not sufficient to measure the linewidth of continous-wave QCLs (typically of the order of a few MHz or smaller). The most common methods for that are the scanning Fabry-Pérot interferometers, also called optical spectrum analyzers, the heterodyne beating experiments, and the absorption experiments.

The first one consist of a Fabry-Pérot interferometer in which the distance between the mirrors is scanned. The free spectral range of such a spectrometer is FSR $= c/2L_{\mathrm{R}}$, where L_{R} is the length of the resonator. It is related to the resolution $\delta\nu$ by $\delta\nu = \mathrm{FSR}/\mathcal{F}$ where $\mathcal{F} = \pi\sqrt{R}/(1-R)$ is the finesse of the resonator. The finesse necessary for high resolution can be obtained only with mirrors having $R \geq 99\%$. This method was used by Blaser and al. to characterize a 10.1 μm laser based on a photon-assisted tunneling transition[6]. A linewidth of 3.9 MHz was observed with an instrumental resolution $\delta\nu \cong$2 MHz.

In the second one, the laser to test is superimposed to a reference one emitting at a close frequency on a optical detector and the resulting signal, which contains beatings at the frequency difference is sent to a spectrum analyzer. One can show that the spectrum of the beat note is a convolution of the spectra of the two lasers. The ultimate limit to the resolution of this method is thus the linewidth of the reference laser. It was used by Ganser et al. to determine the linewidth of a 5.2 μm QCL using a CO reference laser[7] and by Weidmann et al. to determine the linewidth of a 9.1 μm QCL using a CO_2 reference laser[8]. In the first case, the authors reported a linewidth of 0.5 MHz with a sweep time of 20 ms and in the second one, a linewidth varying between 1.3 and 6.5 MHz with a longer sweep

time of 0.5 s.

For the third method, one scans the laser frequency over a known gas absorption line. The measured absorption spectrum, which is a convolution of the known absorption spectrum and the laser lineshape, is then fitted to obtained the laser linewidth. This method was used by, among others, Sharpe et al.[9], Webster et al.[10], Weidmann et al.[11], and Nelson et al.[12]. All these authors reported larger linewidths than with the other measurement methods (24 MHz for Nelson et al. and more for the others) because of the frequency tuning.

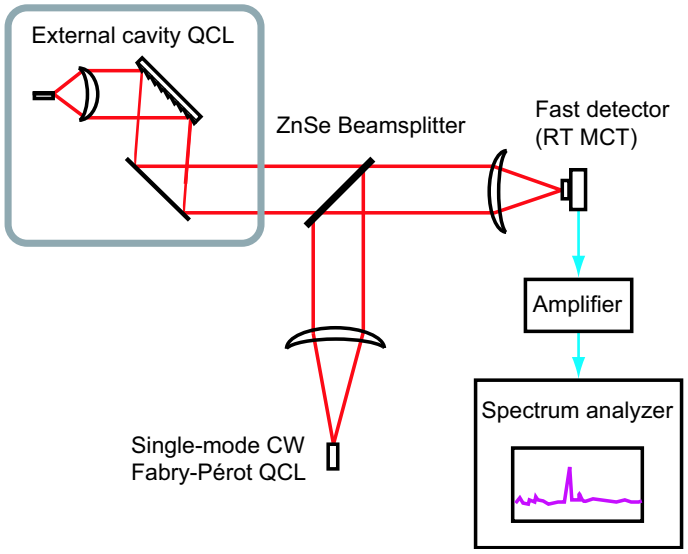

Figure 5.8: Schematic drawing of the heterodyne experiment setup for determination of an upper limit to the linewidth of the EC-QCL.

We used the second method. Our setup is presented in Fig. 5.8. The external cavity laser was heterodyned with a CW Fabry-Pérot device from the same wafer. We operated this device slightly below the largest current at which it was still single-mode and tuned the EC-QCL at a very close frequency using the FTIR. The current was supplied to the chips with two Keithley 2400 SourceMeters. For the FP laser, a low-pass RC filter with a 3 dB cutoff frequency of 16 Hz (R=10 Ω, C=1 mF) was used to reduce current fluctuations. The two beams were superimposed using a ZnSe beamsplitter and detected using a high-speed room temperature MCT detector (Vigo System S.A., Warsaw, Poland, model PEM-L-3). Care was taken to avoid optical feedback in the QCLs by tilting the detector surface with

respect to the beam axis. The resulting radio frequency (RF) beating signal was amplified by a 38 dB broadband (10 kHz-2.5 GHz) amplifer (Sonoma Intruments Co, Santa Rosa, CA, USA, model 317) and its spectrum was acquired on a 9 kHz to 3 GHz spectrum analyzer (Agilent E04402B). A typical beating spectrum is shown in Fig. 5.9. The sweep time was 4 ms and the resolution bandwidth 3 MHz. The full width at half maximum (-3 dB) of the beat note is 5 MHz.

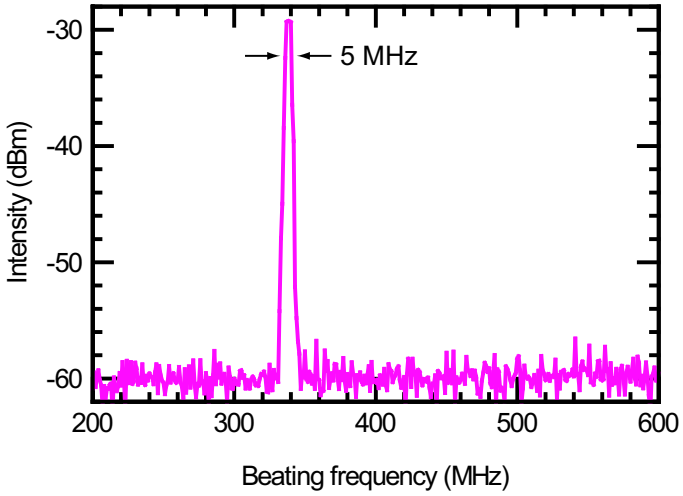

Figure 5.9: Spectrum of a heterodyne beating between the EC-QCL and a Fabry-Pérot chip.

Since we expect a 100 times larger linewidth for the Fabry-Pérot laser than for the external cavity one (see section 5.6.1), this value gives only an upper limit on the actual linewidth of the EC-QCL. This quite large value compared to the theoretical one is due to the jitter of the instantaneous frequency caused by current and temperature fluctuations on the reference laser. According to the temperature and current tuning coefficients that we measured, a temperature variation of only 1 mK or a current variation of 13 μA are sufficient to cause a variation of 5 MHz of the laser frequency.

5.7 High-resolution spectroscopic applications

The broad tuning range and narrow linewidth of this laser make it an interesting tool for high resolution spectroscopic applications. Very soon after its realization, we collaborated with Dr. Gerard Wysocki of Prof. Frank K. Tittel's Laser Science Group at Rice University, Houston, TX, USA to demonstrate effectively its suitability for such applications. Two members of our group, Jean-Marc Bulliard and myself, spent three weeks in Houston to install the setup and explain its utilization and left it there.

The instrument was modified by Wysocki et al. to get rid of the mode-hops described in Sect. 5.5.4. A piezo-activated mode tracking system was implemented to enable independent control of the EC length and diffraction grating angle. The grating was mounted on a moving platform whose position was controlled by a piezo-acuated linear translation stage (Physik Instrumente, model M-014.00 stage and model P-840.60 piezo-actuator) and a rotary stage (Physik Instrumente, model M-035.DP1) which is equiped with a motorized coarse angle control and a piezo-actuated fine control. The chosen components allowed precise positioning of the EC length and grating angle with a resolution of < 0.9 nm and 1 μrad for external cavity length and grating angle, respectively. The total grating angle range provided by PZT scanner was ± 520 μrad. The coarse tuning by the linear motor could be performed within a range of $\pm 6.3^\circ$ and unidirectional repeatability of 10 μrad with the actual position measured by a built-in encoder with a resolution of $\sim$1.4 μrad/unit. The piezo-actuator controlling the external cavity length had a total travel range of 90 μm, which corresponds to a maximum continuous laser frequency tuning range of ~ 2 cm^{-1} at $\lambda \cong 5$ μm.

Figure 5.10 illustrates the performance of the mode-tracking system. The output optical power of the EC-QCL as a function of time was monitored for different fractions of the control signals U_{EC} and U_{GR} (for the EC length and for the grating angle respectively) required for full mode tracking. The laser was driven by $\sim$630 mA current and modulated with a sinusoidal waveform. Three particular modes of operation can be observed: no wavelength tracking (control signals U_{EC} and U_{GR} not applied), only grating wavelength tracking (only

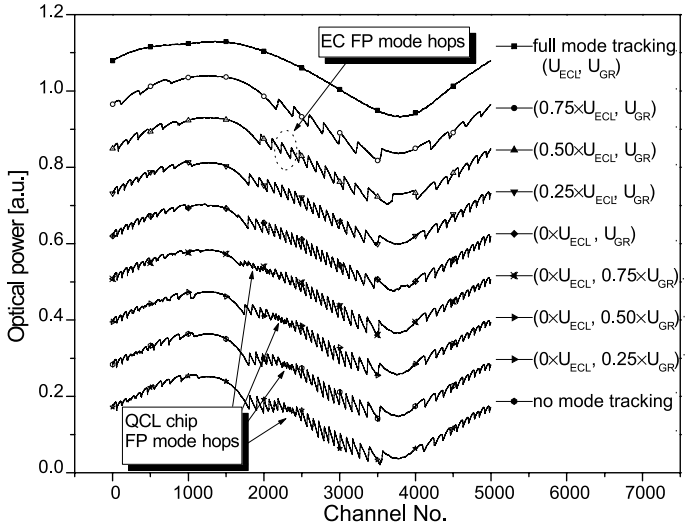

Figure 5.10: Demonstration of mode-hop free operation of the EC-QCL using the piezo-actuated cavity mode tracking system.

U_{GR} applied in full), and full wavelength tracking (both U_{EC} and U_{GR} applied in full). Both QCL FP resonator mode hops and EC FP resonator mode hops can be observed for partial mode tracking. Increase of the PZT control signals results in progressive separation of the mode hops, which finally leads to complete laser longitudinal mode tracking.

The suitability of the EC-QCL for high resolution spectroscopy was demonstrated by performing spectroscopic absorption measurements of nitric oxide, NO, and water, H2O, at reduced pressures. The measured spectrum of a large section of the R-branch of the NO rovibrational spectrum between 1935 and 1961 cm^{-1}, which could be accessed by the present EC-QCL is plotted together with a HITRAN 2000 simulation in Fig. 5.11. In this figure, successive spectral scans are recorded for different positions of the diffraction grating angle. Each scan is the average of 10 single 5000-points scans within 5 s. Thus a single high resolution spectrum containing spectral absorption data in a range $\geq$1 cm^{-1} can resolve spectral features separated by less than 0.006 cm^{-1} (see the inset of Fig. 5.11 depicting the NO-$R_{1/2}$(23.5) line).

All scans were performed using a sinusoidal modulation ($\sim$112 mA$_{\mathrm{p-p}}$ at 2Hz) of the laser current at an operating point of $\sim$650 mA. For scan calibration an air-spaced low finesse etalon constructed of two ZnSe wedged windows separated by 14.5 cm was introduced into

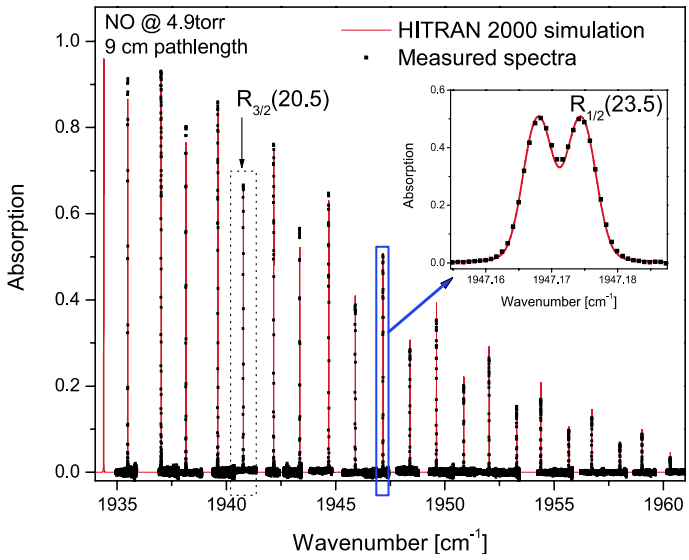

Figure 5.11: Nitric oxide absorption spectra measured at different angles of the EC-QCL plotted together with a HITRAN 2000 simulation. The narrow laser linewidth allows resolving two spectral peaks separated by $\sim$ 0.006 cm^{-1} (see inset).

the beam path. A typical set of data recorded for one of the component spectra presented in Fig. 5.11 is shown in Fig. 5.12. A wavelength calibrated spectra of NO $R_{3/2}(20.5)$ marked in Fig. 5.11 with a dotted box, along with the associated etalon fringe pattern and the calculated calibration curve are presented in the plots of Fig. 5.12.a, b, and c, respectively. In this spectral region the separation of the component lines in NO $R_{3/2}$ doublets is much smaller than in the previously presented NO $R_{1/2}$ line. However, the fine spectral structure at the top of the line can still be resolved as shown in the inset of Fig. 5.12.a. Each single spectral scan was separately calibrated. The shape of the calibration curve presented in Fig. 5.12.c is typical for all measured spectra. A fit of the calibration curve by the sinusoidal function confirms a linear relation between the laser current and frequency of the generated light with a tuning coefficient of 0.01 cm^{-1}/mA.

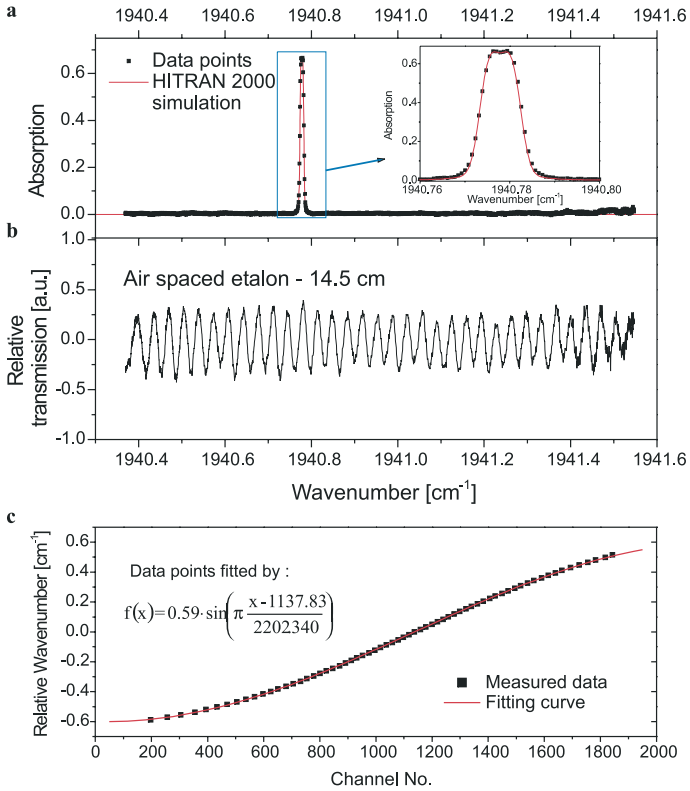

Figure 5.12: a) NO-$R_{3/2}(20.5)$ spectrum recorded within a range of a single scan of the EC-QCL. b) Transmission of an air spaced etalon recorded within the same scan. c) Frequency calibration curve.

Bibliography

[1] J. B. McManus, D. D. Nelson, S. C. Herndon, J. H. Shorter, M. S. Zahniser, S. Blaser, L. Hvozdara, A. Muller, M. Giovannini and J. Faist, "Comparison of cw and pulsed operation with a TE-cooled quantum cascade infrared laser for detection of nitric oxide at 1900 cm^{-1}", Appl. Phys. B **85**, 235 (2006).

[2] S. Blaser, D. A. Yarekha, L. Hvozdara, Y. Bonetti, A. Muller, M Giovannini, and J. Faist, "Room-temperature, continuous-wave, single-mode quantum-cascade lasers at $\lambda \simeq 5.4$ μm", Appl. Phys. Lett. **86**, 41109 (2005).

[3] A. Yariv, *Quantum electronics*, 3rd ed. (Wiley, New York, 1989), p. 199.

[4] C. H. Henry, "Theory of the linewidth of semiconductor lasers", IEEE J. Quantum Electron. **18**, 259 (1982).

[5] R. F. Kazarinov and C. H. Henry, "The relation of line narrowing and chirp reduction resulting from the coupling of a semiconductor laser to a passive resonator", IEEE J. Quantum Electron. **23**, 1401 (1987).

[6] S. Blaser, L. Diehl, M. Beck, J. Faist, U. Oesterle, J. Xu, S. Barbieri, and F. Beltram, "Characterization and modeling of quantum cascade lasers based on a photon-assisted tunneling transition", IEEE J. Quantum Electron. **37**, 448 (2001).

[7] H. Ganser, B. Frech, A. Jentsch, M. Mürtz, C. Gmachl, F. Capasso, D. L. Sivco, J. N. Baillargeon, A. L. Hutchinson, A. Y. Cho, and W. Urban, "Investigation of the spectral width of quantum cascade laser emission near 5.2 μm by a heterodyne experiment", Opt. Comm. **197**, 127 (2001).

[8] D. Weidmann, L. Joly, V. Parpillon, D. Courtois, Y. Bonetti, T. Aellen, M. Beck, J. Faist, and D. Hofstetter, "Free-running 9.1-μm distributed-feedback quantum cascade laser linewidth measurement by heterodyning with a $C^{18}O_2$ laser", Opt. Lett. **28**, 704 (2003).

[9] S. W. Sharpe, J. F. Kelly, J. S. Hartman, C. Gmachl, F. Capasso, D. L. Sivco, J. N. Baillargeon, and A. Y. Cho, "High-resolution (Doppler-limited) spectroscopy using quantum-cascade distributed-feedback lasers", Opt. Lett. **23**, 1396 (1998).

[10] C. R. Webster, G. J. Flesch, D. C. Scott, J. E. Swanson, R. D. May, W. S. Woodward, C. Gmachl, F. Capasso, D. L. Sivco, J. N. Baillargeon, A. L. Hutchinson, and A. Y. Cho, "Quantum-cascade laser measurements of stratospheric methane and nitrous oxide", Appl. Opt. **40**, 321 (2001).

[11] D. Weidmann, F. K. Tittel, T. Aellen, M. Beck, D. Hofstetter, J. Faist, S. Blaser, "Mid-infrared trace-gas sensing with a quasicontinuous-wave Peltier-cooled distributed feedback quantum cascade laser", Appl. Phys. B **79**, 907 (2004).

[12] D. D. Nelson, J. B. McManus, S. C. Herndon, J. H. Shorter, M. S. Zahniser, S. Blaser, L. Hvozdara, A. Muller, M. Giovannini, and J. Faist, "Characterization of a near-room-temperature, continuous-wave quantum cascade laser for long-term, unattended monitoring of nitric oxide in the atmosphere," Opt. Lett. **31**, 2012 (2006).

Chapter 6

External cavity quantum cascade lasers based on heterogeneous cascade active regions

6.1 Introduction

In the previous chapter, we demonstrated a continuous wave thermoelectrically cooled external cavity quantum cascade laser tunable over $\sim$170 cm^{-1} with a side-mode suppression ratio $\geq$ 25 dB. The usefulness of that kind of lasers for high-resolution mid-infrared spectroscopy has then been demonstrated in collaboration with Wysocki et al. in Prof. Tittel's group at Rice University who modified our setup for mode-hop free tuning and used it for spectroscopic absorption measurement of nitric oxide and water. From the point of view of spectroscopic applications, EC-QCLs with a broader tuning range of several hundreds of wavenumbers will be interesting because they will enable the spectroscopy of entire absorption bands. In addition, a broader tuning range will also increase the versatility of these sources for trace gas analysis.

In our previous works described in Chapters 4 and 5, we observed that, as predicted by the theory (see Section 2.3), the part of the gain curve $g(\nu)$ over which the EC-QCL could

be tuned is given by the condition $g(\nu)/g_{\max} \geq \xi$, where $g_{\max}$ is the maximum gain and ξ is the ratio between the threshold gain of the EC-QCL and the threshold gain of the AR coated chip. For our optical setup, we measured values of ξ between 0.65 and 0.8 depending on the characteristics of the chip. In order to realize a more broadly tunable EC-QCL, it is thus necessary to design a structure with gain variation of less than $\sim$20% over a larger wavelength range. A way to achieve this is to make a cascade containing dissimilar stages emitting at different wavelengths.

A similar concept was already used in the field of optical communications; near-infrared external cavity diode lasers with a tuning range of 240 nm (17% of center wavelength) have been realized using nonidentical multiple quantum-wells[1]. QCLs, however, are more adapted to multi-wavelength lasing than interband lasers, because of two reasons. First, the cascaded geometry, in which the active regions are arranged in series and not in parallel like in multiple QW diode lasers, insures the same injection efficiency in all the active wells independently of the injection current. Secondly, in opposition to interband lasers in which the gain is always accompanied by absorption at higher frequencies, there is no reabsorption between active regions emitting at different wavelengths.

This concept has first been demonstrated by Gmachl et al. at Bell Labs who realized a two-wavelength laser emitting simultaneously at 5.2 and 8 μm[2] and an ultra-broadband laser[3]. The latter consisted of 36 three-quantum-well active regions designed to emit at 30 different wavelengths spanned between 5 and 8 μm. The broadband lasing spectrum covered the range from 6 to 8 μm (30% of center wavelength) at cryogenic temperature, and from 7.1 to 7.7 μm (10% of center wavelength) at room temperature. The threshold current density of the device varied from 4 kA/cm^2 at 10 K to 16kA/cm^2 at 300 K.

In this chapter I will present a heterogeneous cascade based on two bound-to-continuum designs centered at 8.4 and 9.6 μm. Using only two different broad gain bound-to-continuum active regions instead of plenty of narrow gain three-QW ones is advantageous for single-mode operation in an external cavity configuration because the strong spectral overlap of the gain spectra prevents multimode lasing to happen at large injection currents. In addition,

the better behavior of this design at high temperature resulted in high performance in pulsed mode at room temperature. Lasing spectra spanning over 20% of the center wavelength were obtained at 300 K with a threshold current density of 4.4 kA/cm^2.

6.2 Structure design

6.2.1 Active region

When designing a heterogeneous cascade for single-mode operation in external cavity, not only the total gain is important but also the spectral overlap of the gain curves of the individual stages. As we will see in Section 6.3, a poor overlap will result in multi-mode lasing at large injection current because the total gain is not clamped at the threshold value. The structure that we used is based on two bound-to continuum designs (see Fig. 6.1). Active region A, already described in Chapter 4, is expected to be centered at 9.6 μm according to simulations. Active region B is a similar design centered at 8.4 μm. The layer sequence of one period, in nanometers, starting from the injection barrier is: **4.3**/1.8/**0.7**/5.5/**0.9**/5.3/**1.1**/4.8/**1.4**/3.7/**1.5**/3.5/**1.6**/3.3/**1.8**/3.1/**2.0**/2.9/**2.4**/2.9/**2.6**/2.7/**3.0**/2.7 where $In_{0.52}Al_{0.48}As$ layers are in bold, $In_{0.53}Ga_{0.47}As$ in roman and the n-doped layers (Si, $2{\cdot}10^{17}$ cm^{-3}) are underlined. According to previous electroluminescence measurements on epilayers based on similar designs (see Chapter 4), a FWHM of 300 cm^{-1} is expected for both designs, and the frequency interval between the two peaks is 150 cm^{-1}. The heterogeneous cascade contains 20 stages of each design.

6.2.2 Waveguide

The complete structure is shown schematically in Fig. 6.2. Since the total number of stages (40) was kept close to what we usually use in this wavelength range (35), a standard waveguide could be used. In adition, because the center wavelengths are only $\sim$14% different, we didn't have to adjust the number of periods of each design to compensate for the wavelength dependent waveguide losses like it has been done in Ref. [3]. The core of the

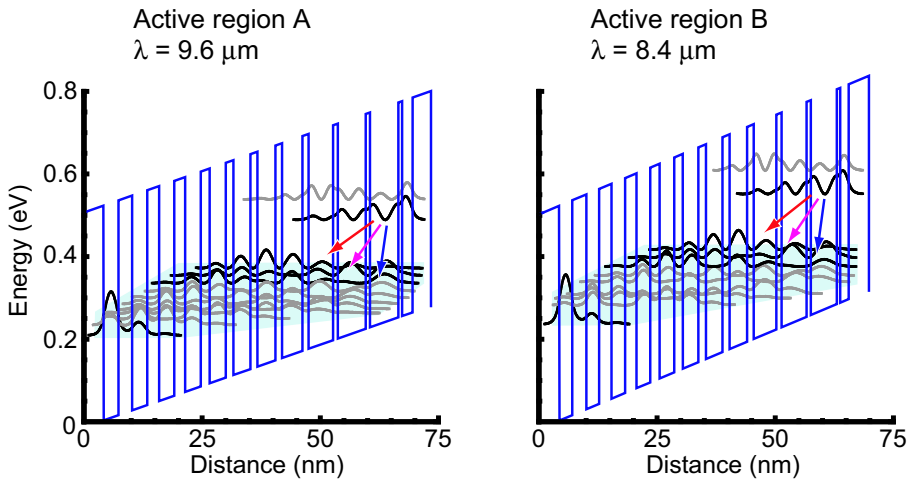

Figure 6.1: Schematic conduction band diagram of one stage of both active regions of the heterogeneous cascade with the moduli squared of the computed wavefunctions. Active region A ($\lambda = 9.6$ μm) is simulated under an applied electric field of 40 kV/cm and active region B ($\lambda = 8.4$ μm) under an applied electric field of 48 kV/cm.

waveguide, grown by molecular beam epitaxy, consists of, starting from the substrate: 200 nm of n-doped InGaAs (Si, $6 \cdot 10^{16}$ cm^{-3}), 20 periods of active region A, 20 periods of active region B, and 300 nm of InGaAs (Si, $6 \cdot 10^{16}$ cm^{-3}). The InGaAs and AlInAs alloys are lattice matched to the InP substrate. The doping level is $3.1 \cdot 10^{11}$ cm^{-2} per period in both active regions. The cladding, grown by metal-organic vapor phase epitaxy, consists of: 4 μm of InP (Si, 10^{17} cm^{-3}), 0.5 μm of InGaAs (Si, $3 \cdot 10^{18}$ cm^{-3}), and finally 50 nm of InGaAs (Si, 10^{19} cm^{-3}).

6.2.3 Spontaneous emission spectra

Electroluminescence spectra of the structure were taken following the sample preparation and measurement technique described in Chapter 3 and already used in Chapter 4. The resulting spectra of a 100 μm square sample at room temperature (300 K) under biases ranging from 8 to 14 V are shown in Fig. 6.3. The FWHM of the spectra is equal to 350 cm^{-1} and has weak dependence on the applied voltage. The frequency range over which $I(\nu)/I_{max} \geq 0.8$, which is easily accesible for single-mode tuning in EC setup, is equal to 205

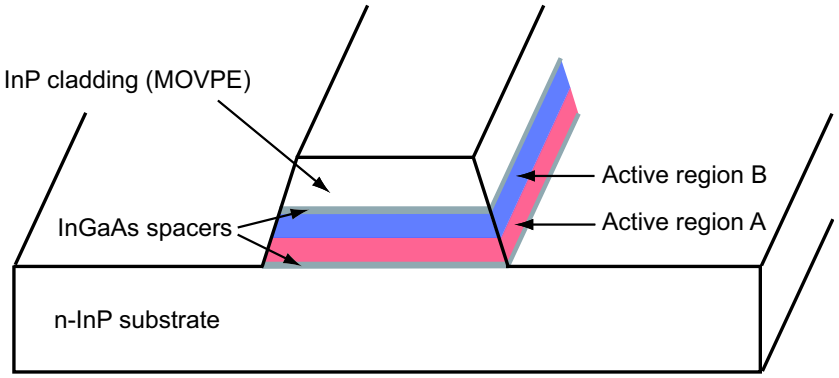

Figure 6.2: Schematic drawing of the complete structure. Two substacks of 20 stages of each designs have been grown in an otherwise standard waveguide structure.

cm^{-1}. The inset of Fig. 6.3 shows two spectra of the same sample at cryogenic temperature (80 K). The FWHM at this temperature is 299 cm^{-1}.

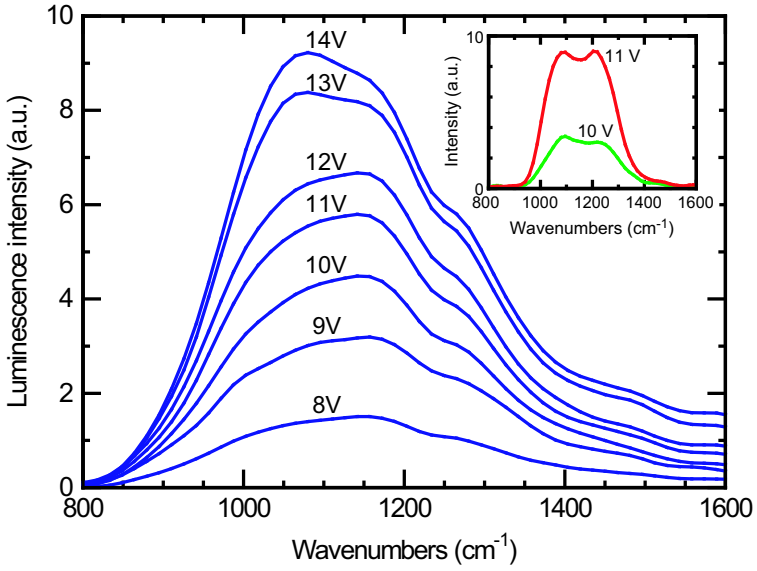

Figure 6.3: Spontaneous emission spectra of a 100 μm squared mesa at 300 K. The FWHM is $\sim$350 cm^{-1} and the frequency range over which $I(\nu)/I_{max} \geq 0.8$ is larger than 200 cm^{-1}. Inset: Spontaneous emission spectra of the same sample at 80 K.

As can be seen in Fig. 6.4, the data between 800 and 1230 cm^{-1} could be well fitted by a sum of two gaussian functions centered at 1040 cm^{-1} and 1190 cm^{-1}, respectively, in

good agrement with the computed transition energies. The deviation from the fit at higher frequencies is attributed to thermally activated emission from the energy level above the upper state. This deviation was not observed at cryogenic temperature (see inset of Fig. 6.3).

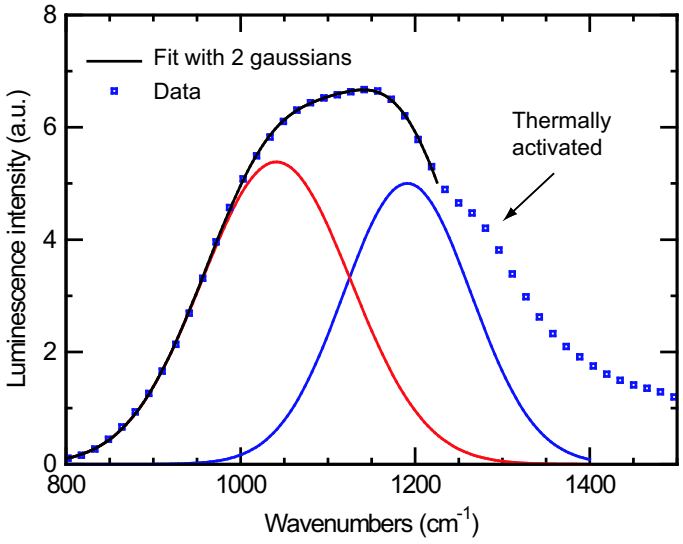

Figure 6.4: Spontaneous emission spectra of a 100 μm squared mesa at 300 K under an applied bias a 12 V. The experimental data have been fitted by a sum of two gaussian functions.

6.3 Rate equation model

Since the gain spectrum of a heterogeneous quantum cascade structure is inhomogeneously broadened, it does not behave like usual structures. In particular, when lasing action occurs at one particular wavelength, only the gain at this wavelength is clamped at the threshold value and not the whole gain curve like in the case of homogeneous broadening. The condition $g(\lambda)/g_{\max} \geq \alpha_{EC}/\alpha_{FP}$ seen in Section 2.3 still holds, but it only gives the range over which single-mode tuning is possible at threshold. In order to investigate theoretically the behavior above threshold we resorted to a rate equation model.

The evolution of the sheet carrier densities $n_{3,a}$, $n_{3,b}$, $n_{2,a}$, and $n_{2,b}$ and the photon flux

density S at the grating selected wavelength λ_G are described by five coupled equations:

$$\frac{dn_{3,i}}{dt} = \frac{J}{q} - \frac{n_{3,i}}{\tau_{3,i}} - S g_{c,i}(n_{3,i} - n_{2,i}) \tag{6.1}$$

$$\frac{dn_{2,i}}{dt} = \frac{n_{3,i}}{\tau_{32,i}} + S g_{c,i}(n_{3,i} - n_{2,i}) - \frac{n_{2,i}}{\tau_{2,i}} \tag{6.2}$$

$$\frac{dS}{dt} = \frac{c}{n}\Big[\sum_j N_{p,j}\, g_{c,j}(n_{3,j} - n_{2,j}) - \alpha_{EC}\Big] S \tag{6.3}$$

where $i = a$, b, and the gain cross sections $g_{c,i}$ are evaluated at λ_G. This model can readily be extended to a structure consisting of a larger number of disimilar active regions.

For simplicity, we substituted a gaussian lineshape L_G with the same full width at half maximum for the bound-to-continuum lineshape L_{BTC}. The gain cross sections read (written as functions of the wavenumber $\tilde{\nu} = \nu/c$ in cm^{-1})

$$g_{c,i}(\tilde{\nu}) = \frac{e^2 f_{\mathrm{tot},i}\,\Gamma_i}{4 m_0 \varepsilon_0 c^2 n L_{p,i}} L_G(\tilde{\nu} - \tilde{\nu}_i) \tag{6.4}$$

where $f_{\mathrm{tot}} = \sum_l f_{kl}$ is the sum of the oscillator strengths of the transitions to all the lower states of the bound-to-continuum and Γ_i is the overlap factor of one stage in the substack i:

$$\Gamma_i = \frac{L_{p,i}}{\sum_j N_{p,j} L_{p,j}}\,\Gamma \cong \frac{\Gamma}{\sum_j N_{p,j}} \tag{6.5}$$

where Γ is the overlap factor of the whole active region.

For the lifetimes, we took the ones of the strongest transition of the BTC, from level 12 to level 10. Because designs a and b are very similar, we found very close values in the two cases: $\tau_{3,a} \cong \tau_{3,b} = 0.58$ ps, $\tau_{2,a} \cong \tau_{2,b} = 0.18$ ps, and $\tau_{32,a} \cong \tau_{32,b} = 2.1$ ps at $T = 300$ K. We found also very similar values of f_{tot} in the two designs for the same reason: 33.5 in active region a and 34 in active region b under applied electric fields of 40 kV/cm and 48 kV/cm, respectively.

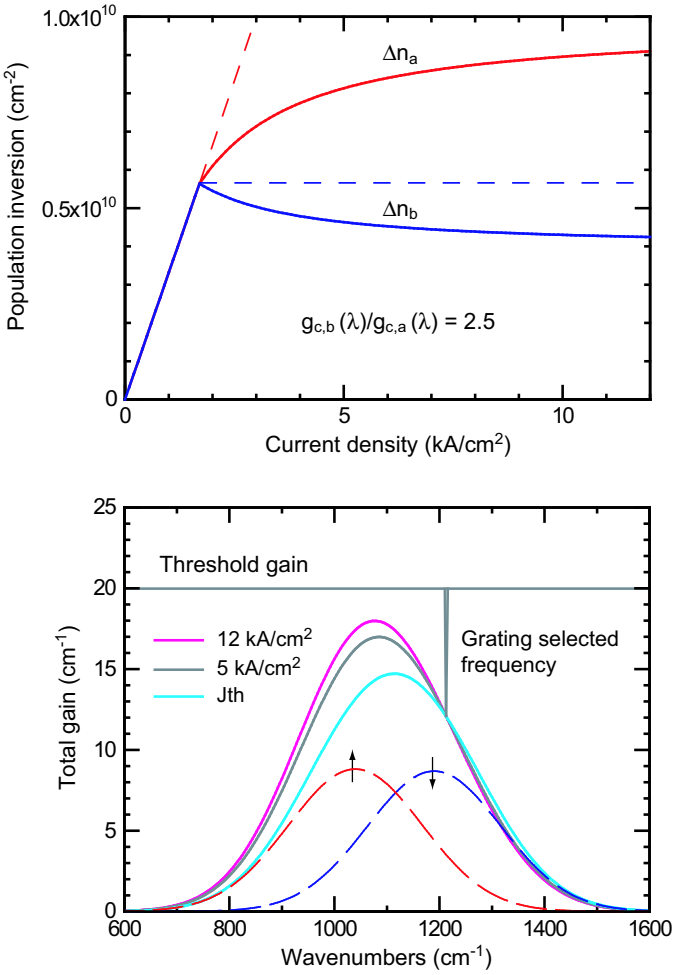

Figure 6.5: Top graph: Population inversion in the two active regions of the heterogeneous cascade. Above threshold the inverted population increases in the active region with the smallest gain cross section (red curve) and decreases in the other one. Bottom graph: Total modal gain at three different values of the current density J. The grey curve represent the wavelength dependent threshold gain and the dashed curves the partial gains in the two substacks at threshold.

Since the two gain cross sections $g_{c,i}(\tilde{\nu})$ are not centered at the same frequency, they are equal only near the maximum of the total gain, about midway between $\tilde{\nu}_a$ and $\tilde{\nu}_b$, but otherwise different. This difference is at the origin of the inhomogeneous behavior. Above threshold, the rate of stimulated emission $\tau_{stim}^{-1} = g_c S$ is smaller in the active region with the smallest gain cross section. Since the number of carriers injected in the upper state is the same in each period because of current conservation, this results in an accumulation of

charges in this state and consequently an increase of the partial gain.

The population inversions Δn_i determined using this model are shown in the top graph of Fig. 6.5. This simulation was done for a detuning of $\cong 100$ cm^{-1} from the peak gain, coresponding to a ratio of the gain cross sections $g_{c,b}/g_{c,a} \cong 2.5$. As expected, Δn_a increases above threshold, and Δn_b decreases in such a way that the total gain $g_{c,a}\Delta n_a + g_{c,b}\Delta n_b$ at the grating selected wavelength stays constant.

However, one can see that this phenomenon quickly saturates and the inverted populations tend asymptotically toward finite values. In the limit where the transport is dominated by stimulted emission (which is difficult to achieve for quantum cascade lasers because of the short upper state lifetime) one has $\Delta n_a/\Delta n_b \rightarrow g_{c,b}/g_{c,a}$. The bottom graph of the same figure shows the total gain for three current densities between threshold and roll-over. In this particular case, despite the large detuning from the peak gain, the laser stays single-mode over the entire current range. According to those simulations, single-mode operation up to roll-over is expected over a range of 225 cm^{-1}. Such a behavior is possible because of the strong overlap of the two gain spectra.

The dashed lines on top graph of Fig. 6.5 show population inversions for active region whose gain spectra do not overlap. In this case the Fabry-Pérot modes of the chip reach threshold already below 3 kA/cm^2.

6.4 Fabrication and characterization of the gain elements

The gain elements were processed in ridge waveguides following standard processing, i.e. wet etching, deposition of a Si_3N_4 passivation layer, deposition of metallic contacts, and electroplating of 4 μm of gold for heat dissipation. The back facets of the chips were high reflection coated with Al_2O_3/Au (300 nm/100 nm) to reduce the threshold current and increase the output power.

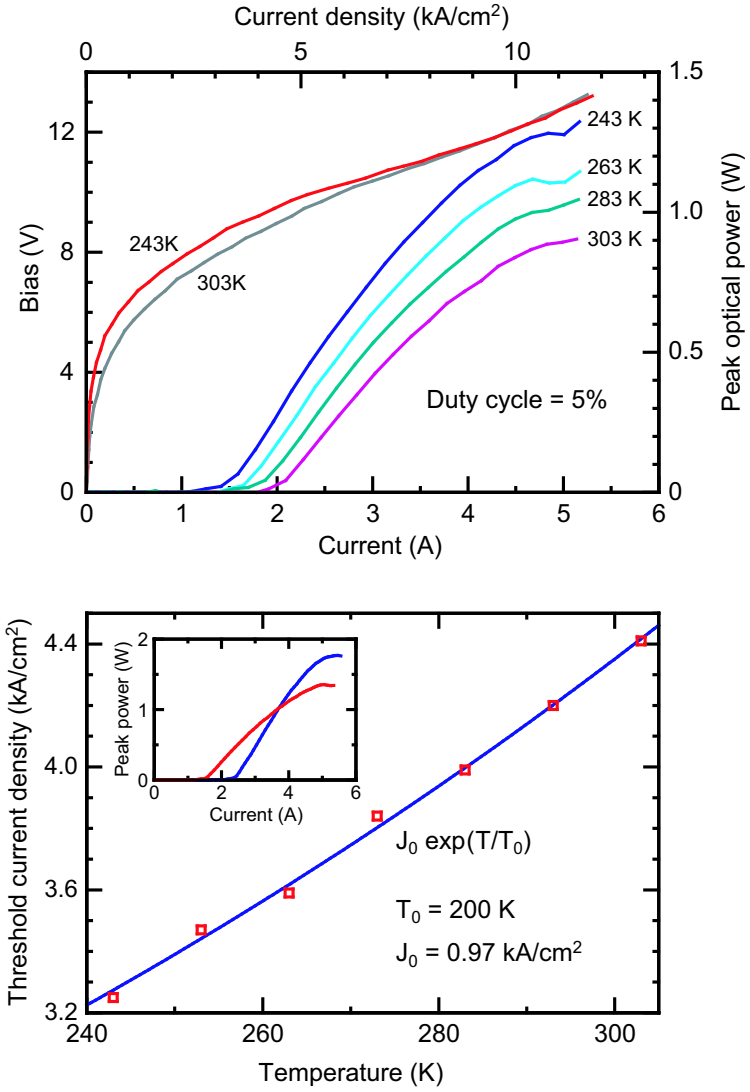

Figure 6.6: Top graph: Peak optical power and bias as functions of the injection current for a high-reflection coated 2.5 mm-long 18 μm-wide chip. Bottom graph: Threshold current density of the same laser as a function of the heatsink temperature. Inset: Peak optical power versus current characteristics of the chip before (red curve) and after (blue curve) the deposition of an AR coating.

The peak output power of a 2.5 mm-long, 18 μm-wide sample operated in pulsed mode on a thermoelectric cooler is shown on top graph of Figure 6.6. These curves were measured using 100 ns current pulses with a repetition rate of 500 kHz (duty cycle = 5%). A maximum peak power of 1.3 W was observed at 243 K. The threshold current density varied from 3.25 to 4.4 kA/cm^2 between 243 and 303 K (see bottom graph of Fig. 6.6). A fit of the form

$J_{\mathrm{th}}(T) = J_0 \exp(T/T_0)$ resulted in a characteristic temperature $T_0 = 200$ K. This chip lased up to a duty cycle of 50% at 253 K with a maximum average optical power of 133 mW at a duty cycle of 20%. The high doping level in the active region allows to inject a large current density in the structure, favoring high peak optical power but, on the other hand, limiting the high duty cycle operation because of the large amount of heat that has to be dissipated.

After the deposition of an YF_3/ZnSe anti-reflection (AR) coating designed to have its minimum reflectivity at 1100 cm^{-1} on the chip front facet, the threshold current at 243 K increased by 60% from 1.5 to 2.4 A (see inset of Fig. 6.6). From these values and estimating waveguide losses to be 10 cm^{-1}, we compute a residual reflectivity of 0.7%. The slope efficiency also increased from 520 to 777 mW/A and the maximum peak power reached 1.77 W.

According to simulations, the anti-crossing of the ground state of the injector and the upper level of the lasing transition occurs at 42 and 50 kV/cm in active regions A and B, respectively. This corresponds to biases of 5.81 and 6.55 V over the two 20 period substacks. For higher voltages, resonant tuneling injection is not possible anymore, resulting in an increase of the differential resistance and a roll-over of the power. Experimentally, we observe the roll-over of the power at 13 V in good agreement with the sum of the aforementioned values. This indicates that, as already observed by Gmachl et al.[2], each substack is apportioned the appropriate fraction of the applied bias.

The lasing spectra of these Fabry-Pérot devices were narrow and centered near 1080 cm^{-1} just above threshold and became broader with increasing current, up to $\sim$200 cm^{-1} at roll-over. Figure 6.7 shows the spectrum of such a device under a bias of 15 V, slightly beyond the roll-over, at 253 K. Fabry-Pérot modes are observed all over the wavelength range between 8.3 and 10 μm, that is over 20% of the center wavelength.

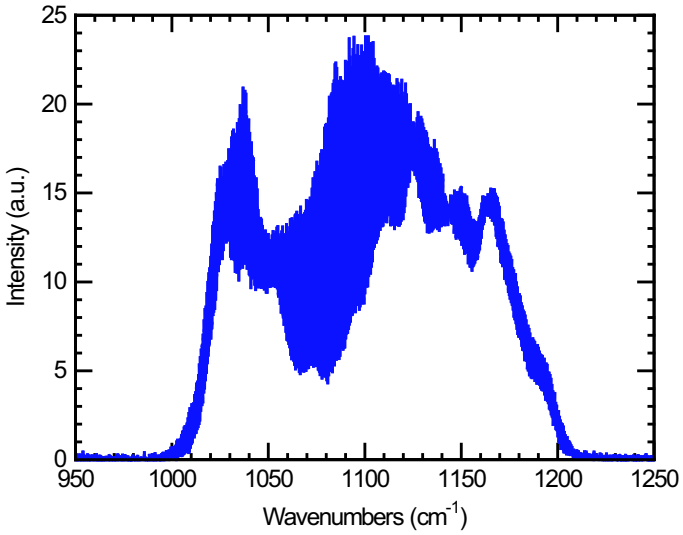

Figure 6.7: Lasing spectrum of a Fabry-Pérot device in pulsed mode at 253 K under a bias of 15 V (linear scale).

6.5 Performance of external cavity lasers

For external cavity tuning experiments, we used the same setup as for the 10 μm laser presented in Chapter 4. The beam was collimated using an f/0.6 aspheric germanium lens and a 150 grooves/mm, 9.3 μm-blazed grating mounted in Littrow configuration provided the optical feedback. The output was taken from the zeroth order reflection of the grating. The chip was operated in pulsed mode using 100 ns pulses with a repetition rate of 200 kHz. The heat-sink temperature was 293 K.

The EC-QCL could be tuned over 2.25 μm (265 cm^{-1}) from 8.16 μm (961 cm^{-1}) to 10.41 μm (1226 cm^{-1}) by varying the grating angle and the bias voltage. This represents an improvement of 77% compared to the 150 cm^{-1} that we achieved with only one type of active region (see Chap. 4). The relative tuning $\Delta\lambda/\lambda_c$ where $\lambda_c = (\lambda_{min} + \lambda_{max})/2$ is the center wavelength is equal to 24%. The maximum peak power was in excess of 65 mW between 1000 cm^{-1} and 1200 cm^{-1} with a highest value of 147 mW near 1100 cm^{-1} (see Fig. 6.9).

It should be noticed that the same chip could already be tuned over 212 $^{-1}$ with its front

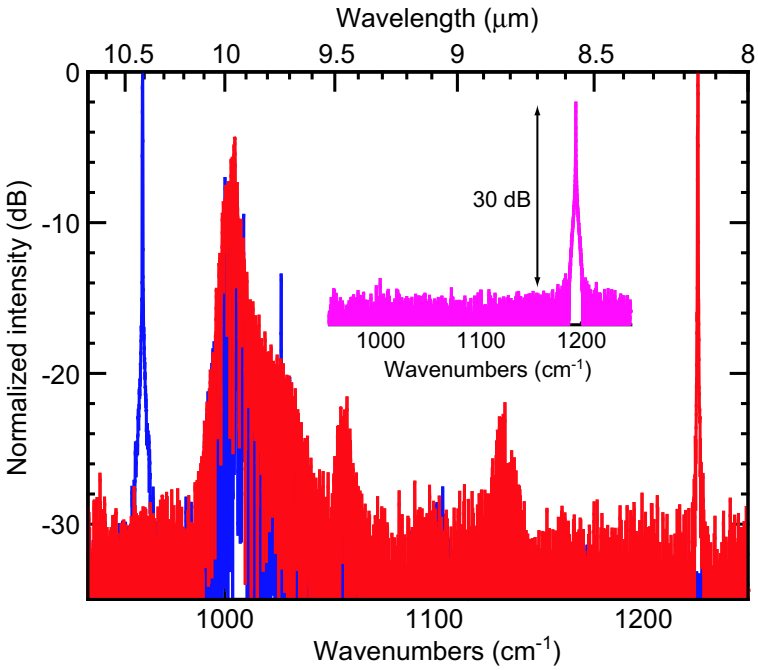

Figure 6.8: The two extreme spectra of the EC-QCL. The parasitic modes near 1020 cm^{-1} are lasing only at the beginning of the pulses. Inset: Time-resolved spectrum taken between 12 and 15 ns after the beginning of the pulse.

facet uncoated, proving that the improvement in tuning range compared to our previous work is mainly due to the broader gain curve of the chip and not to the better AR coating.

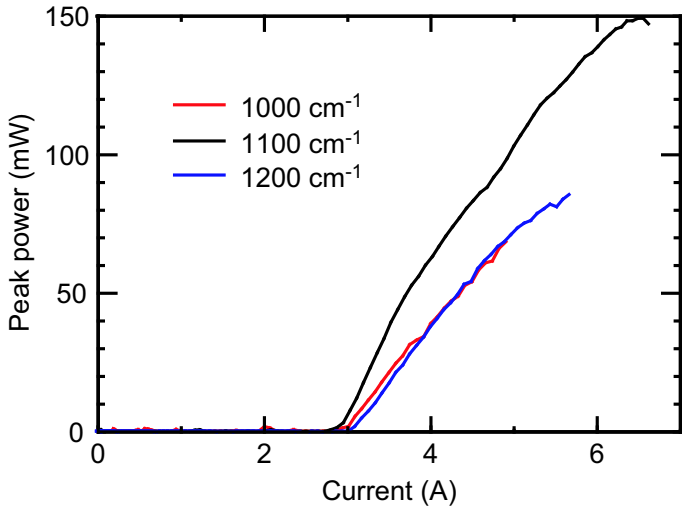

Figure 6.9: Peak output power versus current characteristics of the EC-QCL at three representative lasing frequencies.

In addition to the grating-selected mode, Fabry-Pérot modes of the gain chip were always observed in the measured spectra. These modes were located close to the center of the gain curve, near 1080 cm^{-1}, before the depostition of the AR coating and near 1020 cm^{-1} after. This difference is attributed to a larger residual reflectivity of the AR coating on the long wavelength side. The side mode supression ratio (SMSR) was always smaller or equal to 28 dB.

Time-resolved spectra of the EC-QCL were acquired using a FTIR in rapid scan mode with a fast uncooled MCT detector and a boxcar integrator. For all investigated wavelengths the spectra taken ∼12 ns after the beginning of the pulse were single-mode. As an example, the inset of Fig. 6.8 shows the spectrum of the EC-QCL tuned at 1196 cm^{-1} between 12 and 15 ns after the beginning of the pulse. This spectrum is single-mode with a SMSR of 30 dB.

6.6 Continuous-wave heterogeneous cascade devices

As we have seen in Chapter 5, to obtain the large side-mode suppression ratio which is necessary for spectroscopic applications, external cavity QCLs should be operated in continuous-wave. It is thus important to demonstrate that heterogeneous QCLs are capable of CW operation on thermoelectric cooler.

The epilayer studied in the previous sections of this chapter lased only up to a duty cycle of 50% because of its high doping level. An eplilayer based on the same design, but with only half the doping of this one showed pulsed operation up to 90% when processed in ridge waveguides. We concluded that this layer will lase CW with a buried heterostructure processing. Because this processing was not available at that time, we decided to design a heterogeneous cascade emitting in the wavelength region between 5 and 6 μm for continuous-wave operation in ridge waveguide processing. We used two bound-to-continuum designs in which the (compensated) strain is modulated in each period to confine better the electrons in the upper state at high temperature. The frequency separation between the two peaks was reduced compared with the previous design to a value of ∼100 cm^{-1} in order to generate a higher peak gain. The active region consisted of two substacks of 15 periods centered at

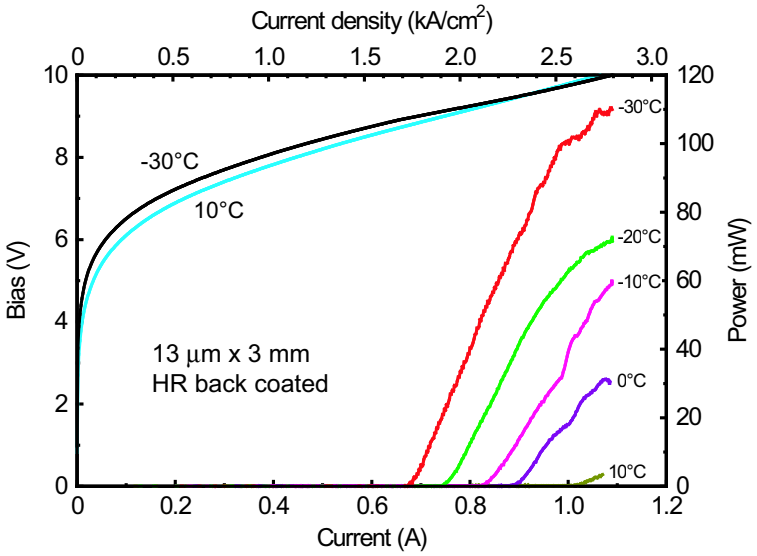

Figure 6.10: CW optical power and bias versus current characteristics of a 13 μm-wide, 3 mm-long HR coated sample.

5.2 μm and 5.5 μm, respectively. The doping level was $8 \cdot 10^{10}$ cm^{-2} per period in both substacks.

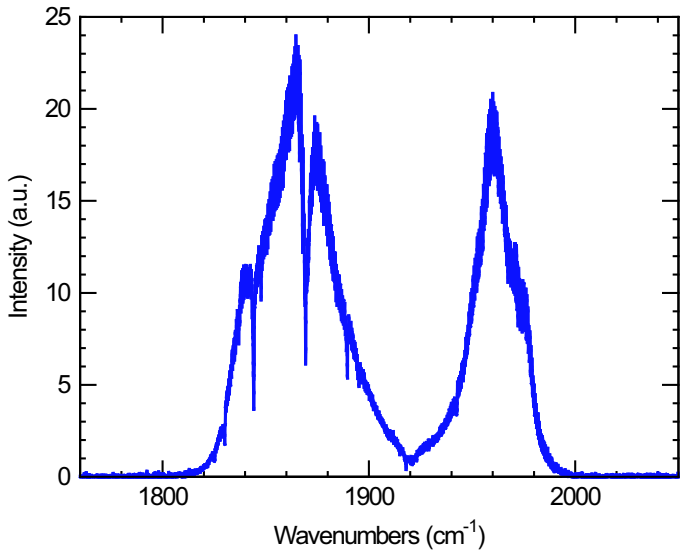

Figure 6.11: Spectrum of a heterogeneous cascade chip in pulsed mode at -30°C.

This epilayer showed continuous wave operation up to +10°C in ridge waveguide processing. Figure 6.10 shows the CW optical power and bias versus current characteristics of a 13 μm-

wide, 3 mm-long sample with high-reflection back facet coating for various temperatures. At $T = -30°C$, the threshold current density was 1.75 kA/cm^2 and the maximum output power was 110 mW. Fig. 6.11 shows the spectrum of a similar device in pulsed mode at $-30°C$. The Fabry-Pérot modes are spanned over 190 cm^{-1}.

The development of broadly tunable CW external cavity lasers based on this CW heterogeneous cascade epilayer is currently in progress.

Bibliography

[1] C. F. Lin, Y. S. Su, and B. R. Wu, "External-cavity semiconductor laser tunable from 1.3 to 1.54 μm for optical communication", IEEE Photon. Technol. Lett **14**, 3 (2003).

[2] C. Gmachl, D.L. Sivco, J. N. Baillargeon, A. L. Hutchinson, F. Capasso, and A. Y. Cho, "Quantum cascade lasers with a heterogeneous cascade: Two-wavelength operation", Appl. Phys. Lett. **79**, 572 (2001)

[3] C. Gmachl, D. L. Sivco, R. Colombelli, F. Capasso, and A. Y. Cho, "Ultra-broadband semiconductor laser", Nature (London) **415**, 883 (2002).

Chapter 7

Conclusions

In this thesis I have presented the development of broadly tunable external cavity quantum cascade lasers.

We could increase drastically the tuning range of such lasers, and improve their performance near room temperature, by using gain elements based on bound-to-continuum active region designs. A tuning range of 150 cm^{-1} at $\lambda \cong 10$ μm has been demonstrated for devices operating in pulsed mode at room temperature. The spontaneous emission spectrum of the gain medium had a full width at half maximum (FWHM) of 297 cm^{-1} at 300 K. The peak output power of the lasers varied between 30 and 70 mW depending on the selected wavelength. The side mode suppression ratio (SMSR) was relatively poor ($\leq$ 25 dB), but time resolved spectra showed that it was due to Fabry-Pérot modes of the chips lasing at the beginning of the pulses because of their shorter round trip time compared to the grating selected mode. An instrument-limited SMSR of 30 dB was observed after the first 12 ns of the pulse.

We have demonstrated for the first time continuous-wave operation of an EC-QCL on a thermoelectric cooler. This laser was tunable over $\sim$170 cm^{-1}, from 4.95 to 5.4 μm, with a SMSR larger or equal to 25 dB. Its output power was in excess of 10 mW over $\sim$100 cm^{-1} and in excess of 5 mW over $\sim$130 cm^{-1}. An upper limit to the linewidth of 5 MHz was determined

with a heterodyne beating experiment. The broad tuning range and narrow linewidth of this laser make it well suited for high resolution mid-infrared absorption spectroscopy.
We collaborated with the Laser Science group at Rice University, Houston, to demonstrate effectively the usefulness of such a laser for high-resolution spectroscopic applications. The setup was modified to allow mode-hop free tuning, by varying the cavity length together with the injection current and the grating angle, and spectroscopic absorption measurements of NO were performed. More than twenty absorption lines of that gas spanned over $\sim$30 cm^{-1} could be scanned and two peaks separated by 0.006 cm^{-1} could be resolved.

Finally, we investigated heterogeneous quantum cascade structures as a way to further increase the tuning range of these sources. A heterogeneous cascade based on two bound-to continuum designs centered at 9.6 and 8.4 μm was realized and studied. Its spontaneous emission spectrum had a FWHM of 350 cm^{-1} at room temperature, and showed a variation of intensity of less than 20% over more than 200 cm^{-1}. External cavity lasers based on gain elements with this active region could be tuned over 265 cm^{-1} from 8.2 to 10.4 μm, that is over 24% of the center wavelength. Again, the SMSR was relatively poor because of the mode competition at the beginning of the pulses, but time resolved spectra showed a SMSR of 30 dB after the first 12 ns. According to our simulations, single-mode operation for the entire current range up to roll-over is expected over 225 cm^{-1} despite the inhomogeneous broadening. Such a behavior is possible because of the strong overlap of the gain curves of the two substacks.
Continuous-wave heterogeneous cascade devices based on two bound-to-continuum designs centered at $\lambda \sim 5.2$ and 5.5 μm have been developed. These chips, which were processed as ridges waveguides, lased CW up to 10°C.

The technological problem of developing a robust, low-reflectivity, AR coating for mid-infrared QC lasers has also been solved. This element is crucial for high performance operation of external cavity lasers because it allows a broader tuning range and mode-hop free tuning without varying the heatsink temperature or injection current. We have found a pair

of materials with excellent adhesion properties to the facet which allows the realization of AR coatings at any given wavelength between 3 and 12 μm. A reflectivity as low as 0.01% was obtained on a buried heterostructure device emitting at 8.4 μm.

Recently, our group has demonstrated a room temperature CW device tunable over 130 cm^{-1} at $\lambda \sim 8.4$ μm. The chip was based on a standard bound-to-continuum design and processed as a buried heterostructure. It lased CW up to $\sim 70°C$ with a high-reflection back facet coating. Continuous tuning between the Fabry-Pérot modes of the chip could be demonstrated using the afore-mentionned AR coating.

The results presented in this thesis demonstrate that room temperature, continuous-wave, external cavity quantum cascade lasers with a tuning range larger than 250 cm^{-1} are feasible in the mid-infrared, between ≈ 4 and 10 μm, using heterogeneous cascade active regions and buried heterostructure processing. In addition, thanks to the anti-reflection coating which has been developed, mode-hop free tuning is possible at constant current and temperature by rotating the grating and adjusting the cavity length.

Acknowledgements

First of all, many thanks to my thesis supervisor, Professor Jérôme Faist for giving the opportunity to work on this project, and for his constant support and unshakable enthusiasm throughout these years.

I also thank Prof. Hans-Peter Herzig (University of Neuchâtel), Prof. Daniel Courtois (University of Reims Champagne-Ardenne, France), and Dr. Alessandro Tredicucci (NEST CNR-INFM & Scuola Normale Superiore, Pisa, Italy) for reading the manuscript and taking part to the examination committee.

I am grateful as well to the members of the Mesoscopic Physics Group with whom I collaborated: Dr. Mattias Beck, Dr. Dmitri Yarekha, Thierry Aellen, Romain Terazzi, and Tobias Gresch, to the two master sudents that I had the pleasure to supervise: Jean-Marc Bulliard and Arun Mohan, who both did an extraordinary work, to the MBE growers: Mattias Beck, Marcella Giovannini and Nicolas Hoyler, and to all the other members, Giacomo Scalari, Christoph Walther, Milan Fischer, Lorenzo Sirigu, Lassaad Ajili, Maria Amanti, for the excellent atmosphere in the group.

Thanks a lot to Dr. Gerard Wysocki and Prof. Frank K. Tittel from Rice University for the fruitful collaboration we had and for welcoming us so kindly to Texas.

I also benefited from interactions with the Alpes Lasers team, especially with Stéphane Blaser who collaborated with me on the development of facet coatings and with Lubos Hvozdara who shared a part of his large experience on QCL fabrication with me, but also with Sophie Brunner, Guillaume Vandeputte, and Antoine Muller.

Thanks also to the technical and administrative staffs of the Institute of Physics who really made my life easier during this time.

Daniel Hofstetter and all the Optoelectronics Group, that is Marcel Graph, Esther Baumann, Fabrizio Giorgetta, and Yargo Bonetti are also acknowledged for their kind collaboration.

Merci beaucoup à mes parents pour m'avoir laissé choisir ma voie et pour leur soutien tout au long de mes études.

Published work

- **R. Maulini**, M. Beck, J. Faist, and E. Gini, "Broadband tuning of external cavity bound-to-continuum quantum-cascade lasers", Appl. Phys. Lett. **84**, 1659 (2004).
- **R. Maulini**, D. A. Yarekha, J.-M. Bulliard, M. Giovannini, J. Faist, and E. Gini, "Continuous-wave operation of a broadly tunable thermoelectrically cooled external cavity quantum-cascade laser", Opt. Lett. **30**, 2584 (2005).
- G. Wysocki, R. F. Curl, F. K. Tittel, **R. Maulini**, J. M. Bulliard, and J. Faist, "Widely tunable mode-hop free external cavity quantum cascade laser for high resolution spectroscopic applications", Appl. Phys. B **81**, 769 (2005).
- **R. Maulini**, D. A. Yarekha, J.-M. Bulliard, M. Beck, M. Giovannini, J. Faist, and E. Gini, "Broadly-tunable external cavity quantum-cascade lasers", Proc. SPIE **6010**, 601001 (2005).
- **R. Maulini**, A. Mohan, M. Giovannini, J. Faist, and E. Gini, "External cavity quantum-cascade laser tunable from 8.2 to 10.4 μm using a gain element with a heterogeneous cascade", Appl. Phys. Lett. **88**, 201113 (2006).
- T. Aellen, **R. Maulini**, R. Terazzi, N. Hoyler, M. Giovannini, J. Faist, S. Blaser, and L. Hvozdara, "Direct measurement of the linewidth enhancement factor by optical heterodyning of an amplitude-modulated quantum cascade laser", Appl. Phys. Lett. **89**, 91121 (2006).

Contributions

- **R. Maulini**, J.-M. Bulliard, D. A. Yarekha, T. Gresch, M. Giovannini, J. Faist, and E. Gini, "Broadly-tunable continuous-wave thermoelectrically-cooled external cavity quantum-cascade laser", Poster at the 5th QCL-Workshop, Freiburg im Breisgau (Germany), September 23-24, 2004.

- **R. Maulini**, D. A. Yarekha, J.-M. Bulliard, M. Beck, M. Giovannini, J. Faist, and E. Gini, "Broadly-tunable external cavity quantum-cascade lasers", Invited talk at Optics East 2005, Boston, MA (USA), October 23-26, 2005.

- **R. Maulini**, A. Mohan, M. Giovannini, J. Faist, and E. Gini, "External cavity quantum-cascade laser tunable from 8.2 to 10.4 μm using an inhomogenously broadened gain element", Talk at CLEO/QELS 06, Long Beach, CA (USA), May 21-26, 2006.

- **R. Maulini**, A. Mohan, M. Amanti, M. Giovannini, J. Faist, A. Wittmann, and E. Gini, "Broadly tunable external cavity quantum-cascade lasers", Invited talk at the 2nd International Workshop on Quantum Cascade Lasers, Brindisi (Italy), September 6-9, 2006.